Imperial College London

MRC Clinical Sciences Centre

Illuminating cAMP dynamics at the synapse with multiphoton FLIM-FRET Imaging

Lucien West

Doctor of Philosophy (PhD) Thesis

Neuroplasticity and Disease Group

MRC Clinical Sciences Centre

Imperial College London

&

Photonics Group

Department of Physics

Imperial College London

ABSTRACT

The study of signalling pathways within mammalian physiology has long been hindered by the size of the players involved, being far beyond the realms of the conventional light microscope. The advent of advanced fluorescent imaging techniques has revolutionised our capabilities to probe biological processes.

The work in this thesis particularly utilised Förster resonance energy transfer (FRET), a fluorescence-based technique that can provide functional readouts of the processes underlying cellular function. Specifically I worked to develop and optimise a fluorescence imaging system for investigating the dynamics and function of cyclic adenosine monophosphate (cAMP), a ubiquitous second messenger.

The neuroscientific study of how the brain can learn and recall memories is a rapidly advancing field. The current challenges of tackling dementias, such as Alzheimer's disease, and preventing memory loss can only be addressed through better understanding of how memories can be stored. It is now believed that neurons retain memories within their synapses, the femtolitre structures that determine the strength of these connections.

cAMP has been shown to play a distinctive role in orchestrating the retention of long term memory at the synaptic level. However, its spatial and temporal activation profiles are still not fully understood. To address this, my PhD project combined FRET readouts with cutting edge imaging techniques applied to synapses in neuronal cultures that provide reasonably convenient optical access.

By examining the structure of these synapses, along with the measurement of cAMP concentration in different neuronal regions, this project uncovered the highly compartmentalised nature of this signalling molecule, seen to act directly at the sites of strengthening synapses.

Through the optimisation of a FRET imaging system for studying activity in neuronal tissues, this project establishes a method for the future investigation of a plethora of pathways underlying the healthy functioning of the mammalian brain.

DECLARATION OF ORIGINALITY

All work performed in this thesis, unless explicitly stated, was undertaken by myself at either the Clinical Sciences Centre or Department of Physics at Imperial College London. No part of this degree has been submitted for another degree or qualification.

COPYRIGHT DECLARATION

The copyright of this thesis rests with the author and is made available under a Creative Commons Attribution Non-Commercial No Derivatives licence. Researchers are free to copy, distribute or transmit the thesis on the condition that they attribute it, that they do not use it for commercial purposes and that they do not alter, transform or build upon it. For any reuse or redistribution, researchers must make clear to others the licence terms of this work.

TABLE OF CONTENTS

1 Introduction to the Project 15
2 Introduction to Fluorescence 17
2.1 Fluorescence microscopy 17
2.2 Fluorophores 17
2.2.1 Excitation and Emission 17
2.3 One and Two Photon Systems 20
2.4 Förster Resonance Energy Transfer (FRET) 22
2.5 Fluorescence Lifetime Imaging Microscopy (FLIM) 24
2.5.1 Time-Domain FLIM 25
2.5.2 FLIM-FRET 26
3 Learning and Memory 28
3.1 The Synapse 28
3.1.1 The Pre-Synaptic Site 29
3.1.2 The Post-Synaptic Site 29
3.2 Synaptic Plasticity 30
3.3 Synaptopathology 33
3.4 cAMP and its Role in the Brain 34
3.5 Compartmentalisation of cAMP in cells 37
3.6 Fluorescent probing of synaptic structures 38
4 Aims of this Project 42
4.1 Experimental Outline 42
5 Culturing the Brain 44
5.1 The Challenge 44
5.2 Transfection Methods 46
5.2.1 Electroporation 47
5.2.2 Viral Transduction 51
5.2.3 Biolistics 54
5.3 Systems to Carry Forward 58
6 Development of a Culture Imaging/Manipulating System 60
7 Finding the Best Sensor 65
7.1 Introduction to cAMP sensors 65
7.2 Analysis of Dynamic Range 70
7.3 HEK Cell Studies 71
7.3.1 HEK FRET 72
7.3.2 HEK FLIM 77
7.4 Primary Neuron Studies 82

7.4.1 PNC FRET 82
7.4.2 PNC FLIM 84
7.5 OSC Studies 85
7.5.1 OSC FLIM 86
7.6 Proceeding with the Optimum Sensor 87
8 Combining cAMP Activation and Synaptic Structural Changes 89
8.1 Rapid Synaptic Changes Occur in OSCs 89
8.2 cAMP Compartmentalisation 93
8.2.1 Compartmentalisation is maintained even after drug induced changes 95
8.3 Increased cAMP levels are detected at sites of synaptic strengthening 98
9 Materials and Methods 102
9.1 DNA 102
9.1.1 Constructs 102
9.1.2 Amplification 102
9.1.3 Sequencing 103
9.2 Animals 103
9.3 Live Cultures 104
9.3.1 HEK Cell Culture 104
9.3.2 Primary Neuronal Culture 105
9.3.3 Organotypical Slice Culture 107
9.4 Drugs 110
9.5 Solutions 111
9.5.1 Physiological Solution –HEK Cells 111
9.5.2 Artificial cerebrospinal fluid – OSCs 111
9.6 Perfusion System 112
9.7 Single Photon Imaging 113
9.8 Two Photon Imaging 114
9.9 Image Analysis 115
9.9.1 Grid Scan Stitching 115
9.9.2 EPBScore 115
9.9.3 Ratiometric FRET Quantification 116
9.9.4 FLIM analysis 118
9.9.5 Calcium Imaging Analysis 118
9.9.6 Statistics 118
10 Discussion 120
10.1 Microscopy 120
10.2 Fluorescent probes and FRET sensors 122

10.3 Stimulation 124
10.4 Morphology and Bouton Size 125
10.5 cAMP activity is upregulated at sites of pre-synaptic enlargement 126
10.6 cAMP in Disease 128
11 Conclusions and Future Work 130
11.1 Summary of findings 130
11.2 Future work 131
11.3 Closing Remarks 132
12 References 134
13 Appendices 151
13.1 Appendix i: *in vivo* calcium activity recording 151
13.2 Appendix ii: Super Resolution Microscopy 153
13.3 Additional drug-induced changes of cAMP activity 154
13.4 Appendix iv: MATLAB code 155
13.4.1 FRET analysis of cells 155
13.4.2 Alignment of multiphoton tiling 156
13.4.3 Alignment of multiphoton axonal tracking 156
13.4.4 Time-Resolved Analysis for GcamP 158

Table of Figures

Figure 1 The Jablonski Diagram 18
Figure 2 The Stokes' Shift 19
Figure 3 Single and Multiphoton Excitation 20
Figure 4 Conditions required for FRET 22
Figure 5 Schematic of a TCSPC FLIM system. 26
Figure 6 Example FRET lifetime response 27
Figure 7 cAMP Signalling Pathway. 36
Figure 8 Epac-mediated signalling pathways and functions. 37
Figure 9 Dendritic response to glutamate uncaging with a CaMKII sensor. 40
Figure 10 Experimental outline of the project 43
Figure 11 Set up of electroporation conductance trial. 47
Figure 12 Different versions of electroporator tips for delivery DNA to OSCs. 48
Figure 13 Example of electroporation transfection efficiency. 49
Figure 14 Comparison of electrode tips for transfection efficiency. 50
Figure 15 Comparison of viral transductions in OSCs. 52
Figure 16 Microinjection of viral particles into OSCs, guided via bright field microscope 53
Figure 17 The BioRad Helios Gene Gun 54
Figure 18 Comparison of Biolistic Parameters 57
Figure 19 Examples of gene gun differences in relation to transfection efficiency. 57
Figure 20 Intensity of GFP measured after biolistic transfection. 58
Figure 21 Expression of CFP-Epac-YFP in a transgenic mouse. 59
Figure 22 Dish insert and perfusion pump for HEK cell studies. 61
Figure 23 Series of prototype 3D printed perfusion systems. 62
Figure 23 Comparison of perfusion systems based on inlet location. 64
Figure 24 Photobleaching comparison 68
Figure 25 Schematic of Epac sensors 69

Figure 26 cAMP concentrations in HEK293T cells after drug addition. 72
Figure 27 Fluorescent Spectra of an mTurquoise-Epac-VenusVenus FRET Sensor 73
Figure 28 Example of HEK293T cells expressing $^{T}Epac^{VV}$ sensor. 74
Figure 29 FRET Montage of mT2-Q270E-VV Sensor in HEK293T cells 75
Figure 30 Comparison of Epac Sensors from the NKI 77
Figure 31 FRET-FLIM response of Sensors in HEK cells acquired on a plate-reader 78
Figure 32 Lifetime Decay of FRET sensor in HEK cells. 79
Figure 33 FRET-FLIM screening of sensors in HEK cells with confocal microscopy 81
Figure 34 Primary neuron cultures in vitro. 82
Figure 35 FRET in Primary Neurone Cultures 84
Figure 36 PNC 2P-FRET-FLIM Response to forskolin. 85
Figure 37 Forskolin-induced responses in OSCs 86
Figure 38 Comparison maximal FLIM measurement 87
Figure 39 The EPBscore software 90
Figure 40 Synaptic turnover along axons under 2-Photon microscopy. 91
Figure 41 EPB Size Changes in OSCs over 90min time period. 92
Figure 42 Example of compartmentalisation of cAMP at axonal boutons. 93
Figure 43 Donor expression only of mTurquoise2. 95
Figure 44 cAMP compartmentalisation preserved when forskolin is added 97
Figure 45 Correlation of cAMP concentration (FRET-FLIM) with bouton size changes (2P) 100
Figure 46 Workflow of Analysis 116
Figure 47 Calcium activity imaged and quantified from 2-Photon acquisition. 152
Figure 48 Super-resolution images of PNCs with a SIM system. 153
Figure 49 FRET responses for 100µM forskolin and 1mM MDL. 154

Table of Tables

Table 1 Comparison of viral vectors for efficiency 51

Table 2 Variable parameters to optimise for biolistic transfection. 55

Table 3 Comparison of transfection methods for introducing plasmid DNA into OSCs. 58

Table 4 Imaging methods selected for different cultures within this project 60

Table 5 The FRET sensors used in this project with their respective source papers. 67

Table 6 Physiological solution for fibroblast imaging. 111

Table 7 Artificial CSF solution for OSC imaging. 112

Acknowledgements

The three and a half years spent on this project was a challenging yet productive period of my education. There were many obstacles to overcome, but with support from many different people across multiple fields I was always able to seek information and advice whenever it was needed.

My supervisors Dr. Vincenzo de Paola of the Neuroplasticity and Disease Group and Dr. Chris Dunsby and Professor Paul French of the Photonics Group where supportive and insightful throughout, and provided me with all of the tools and equipment (physically and mentally) to complete the project in my own way, for which I am very grateful.

The members of both labs were always happy to help and socialise, as was the rest of the departments. I would also like to thank Dr. Mark Ungless who helped guide me when I seemingly came against dead-ends and provides excellent student support for the clinical sciences centre.

Finally, it was all made much smoother with the excellent Ju Jitsu training provided by Rick Bates at the CSC, allowing for plenty of frustration to be fought out twice a week on the mats. It was also in the dojo where I met Ola, who continues to provide me with joy, laughter and adventure in our lives together.

List of Abbreviations

AAV	Adeno-Associated Virus
ABS	Acrylonitrile Butadiene Styrene
AC	Adenylate (Or Adenylyl) Cyclase
aCSF	Artificial Cerebrospinal Fluid
ADC	Analog To Digital Converter
AMPA	A-Amino-3-Hydroxy-5-Methyl-4-Isoxazolepropionic Acid
APT	
ATP	Adenosine Triphosphate
AV	Adeno-Virus
CAD	Computer Assisted Design
cAMP	Cyclic Adenosine Monophosphate
CFP	Cyan Fluorescent Protein
CMV	Cytomegalovirus
CREB	Camp Response Element-Binding Protein
CSF	Cerebrospinal Fluid
DEP	Dishevelled, Egl-10 And Pleckstrin Domain
DLR	Dna-Loading Ratio
DMEM	Dulbecco's Modified Eagle's Medium
DMSO	Dimethyl Sulfoxide
DNA	Deoxyribonucleic Acid
EDTA	Ethylenediaminetetraacetic Acid
ELISA	Enzyme-Linked Immunosorbent Assay
EPAC	Exchange Factor Directly Activated By Camp

EPB	En-Passant Bouton
FBS	Fetal Bovine Serum
FD	Frequency Domain
FLIM	Fluorescence Lifetime Imaging Microscopy
FRET	Förster Resonance Energy Transfer
FSK	Forskolin
GCaMP	Gfp-Calmodulin Protein
GEF	Guanine Nucleotide Exchange Factor
GFP	Green Fluorescent Protein
GPCR	G Protein–Coupled Receptors
HEK	Human Embryonic Kidney Cells
IBMX	3-Isobutyl-1-Methylxanthine
IRF	Instrument Response Function
KCL	Potassium Chloride
LB	Luria Broth
LTD	Long-Term Depression
LTP	Long-Term Potentiation
LV	Lentivirus
MAPK	Mitogen-Activated Protein Kinases
MATLAB	Matrix Laboratory
MEM	Minimum Essential Medium
NA	Numerical Aperture
NaCl	Sodium Chloride
NMDA	N-Methyl-D-Aspartate
NSF	N-Ethylmaleimide-Sensitive Factor
OSC	Organotypic Culture

PBS	Phosphate-Buffered Saline
PDE	Phosphodiesterase
PEI	Polyethylenimine
PKA	Protein Kinase A
PLA	Polylactic Acid
PMT	Photomultiplier Tube
PNC	Primary Neuronal Culture
PSD	Post-Synaptic Density
PTFE	Polytetrafluoroethylene
PVP	Polyvinylpyrrolidone
REM	Ras Exchange Motif
RFP	Red Fluorescent Protein
RNA	Ribonucleic Acid
SIM	Structured Illumination Microscopy
SNARE	Soluble Nsf Attachment Protein
SYN	Synapsin
TAC	Time To Amplitude Converter
TB	Terminal Bouton
TCSPC	Time-Correlated Single Photon Counting
VAMP	Vesicle-Associated Membrane Protein
VV	Venus-Venus
YFP	Yellow Fluorescent Protein

1 INTRODUCTION TO THE PROJECT

The development of advanced molecular biology and fluorescence-based imaging tools has greatly improved our understanding of mammalian physiology in the past two decades. It has provided us with the ability to transfer a stretch of DNA into cells of interest and use their own biological machinery to decode and then build fluorescent probes capable of reflecting changes on a molecular level.

Before the advent of super-resolved microscopes, the limitations of light microscopy prevented structures much below 400 nm from being resolved. However, spectroscopic techniques exploiting fluorescent biosensors have provided biologists with detailed insights into the inner workings of different cells and tissues.

This PhD project aimed to utilise such a biosensor to investigate how a relatively well-researched signalling molecule, cAMP, performs its role in the processes underlying the way in which mammals learn and retain memories, providing a visual understanding of the how, when and where cAMP exerts its functions.

This thesis is structured to present my work chronologically, first describing my development and optimisation of the method for characterising and acquiring cAMP data *in situ* and then discussing the building of a dataset to detail the molecular dynamics in a neuronal system. The first chapter provides an introduction to fluorescence microscopy, from the fluorescent proteins themselves, to the mechanics of FRET biosensors, to the tools required to image them in a variety of biological environments.

In Chapter 3, I introduce the connections between nerve cells, the synapses, and their morphology and modulations upon the learning of new memories. The significance of studying the synapse and its role in a wide range of neuropsychiatric disorders is also discussed, as well as the known role of cAMP in synaptic plasticity. The use of fluorescent biosensors to

measure cAMP concentration is also introduced as a novel method for improving our understanding of its activity in living cells.

The aims of the neurobiology study are outlined in Chapter 4, along with a brief description of the experimental design that led to the optimisation of the imaging system used to acquire the final dataset.

Chapters 5 through 7 describe the processes of screening, selection, discovery and optimisation to determine the best possible set-up and approach to measuring cAMP in neuronal processes. This begins with the challenges of culturing the brain in a controlled environment, reminiscent of a mammalian brain *in situ*; proceeding to the development of an imaging system modified to record from such tissues and finally to the selection and optimisation of the most sensitive FRET biosensor available for acquiring information on low concentrations of cAMP.

Having established which biosensor would provide the highest signal to noise ratio and the best imaging system for recording cAMP dynamics in a culture medium that reflected the *in vivo* environment, Chapter 8 describes the combination of high resolution and live cell imaging applied to provide both structural and functional information. By combining three dimensional scanning over a 90-minute time period, as well as recording the concentration of cAMP within the synapses using a FRET biosensor, a correlation is seen between a compartmentalised increase in the signalling molecule and the enlargement of synaptic sites.

Chapter 9 discusses the findings in the context of better understanding learning and memory and the signalling processes that drive it, especially in the case of strengthening pathways at the synapse, as indicated from the results.

The materials and methods used throughout the project are described in Chapter 9, while the overall conclusions and where the project may go in the future are finally discussed in Chapter 11.

2 INTRODUCTION TO FLUORESCENCE

2.1 FLUORESCENCE MICROSCOPY

The field of biology is today shaped by scientists' ability to observe processes and phenomena on a microscopic level, in vitro or in vivo. For centuries, the compound microscope has been used to bring biological structures down to the micron scale into focus. Today, however, major advances in the field of fluorescence microscopy have enabled methods of discovery, allowing multiple labelling of sub-cellular regions with a high level of specificity and the dynamic observation of intracellular biological processes. Fluorescence microscopy, in particular, has progressed from merely identifying features in samples to probing molecular activities in live cell cultures through action-dependent changes in florescence emission. These now essential tools have revolutionised modern biology and our understanding of microscopic systems.

The first fluorescent protein, green fluorescent protein (GFP), was isolated from the *Aequorea Victoria* jellyfish over 50 years ago (Shimomura et al., 1962), when its bioluminescent properties were first observed. Since then, a plethora of colours and variants of fluorescent proteins have been synthesised and, to this day, improvements of this essential tool are still being made.

2.2 FLUOROPHORES

2.2.1 Excitation and Emission

The function of the fluorescent microscope is to supply light at a specific wavelength (the excitation wavelength) to a fluorescent sample and to separate the emitted light, which is always at higher wavelength (the emission wavelength) from the strong background of the excitation light.

The photophysical mechanism underlying fluorescence is commonly depicted with a Jablonski energy diagram (Figure 1). This is a simplified depiction of the electronic states of a fluorescent molecule, and how electrons can shift between them. At each electronics energy level (S_0, S_1, etc.), a large number of vibrational levels of energy can be occupied, depicted by the series of grey lines at each electronic energy level. For typical fluorophores in solution, there will also be even more closely spaced rotational energy levels associated with each vibrational energy level (not shown).

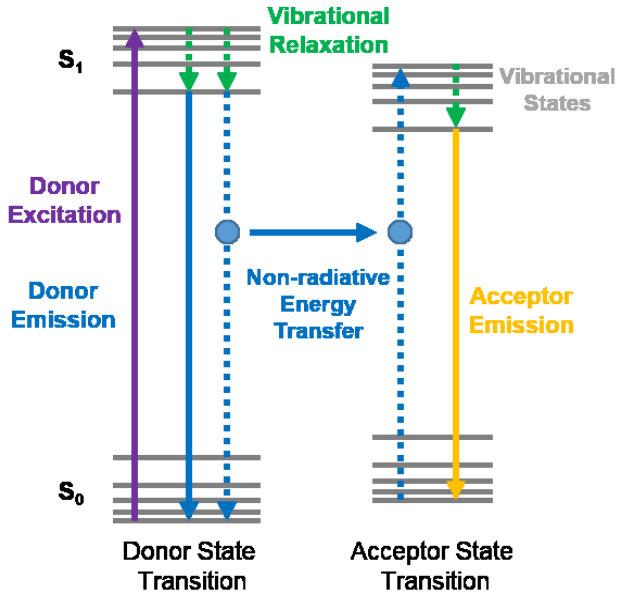


Figure 1 The Jablonski Diagram Depicting the shift in energy state of fluorescent molecule upon excitation.

The configuration of the fluorescent molecule prior to excitation consists of electrons predominantly occupying the vibrational energy levels associated with its ground state (S0). In thermal equilibrium the occupation of the energy levels is governed by the Boltzmann distribution with little to no population in the excited states from which emission can result. This is the resting (equilibrium) state for molecules.

Upon irradiation by photons at a specific energy (or wavelength), the electrons are excited to a higher state of energy (e.g. the first excited state, S_1), closely followed by a rapid thermalisation and loss of energy as the electrons relax to the lowest vibrational levels of the excited state. This excited state relaxation is fast, occurring on sub-picosecond time scales.

At this point, the return to S_0 can be via either radiative or non-radiative decay. Fluorescence emission results from the former mechanism (the left-hand portion of Figure 1), whereby each electron decays to a vibrational energy level associated with the electronic ground state, resulting in the spontaneous emission of one photon. There follows a rapid thermalisation of

the electrons to the lowest vibrational levels to complete the fluorescence cycle. The relaxation back to the ground state following excitation occurs on nanosecond timescales in most fluorophores, much slower than the vibrational relaxation.

As the fluorescent stage of relaxation always occurs from the lowest energy state of S1 to the same energy level of S0, regardless of initial excitation level, the photon emitted is always of lower energy, and therefore higher wavelength. This is described as the Stokes shift (depicted in Figure 2).

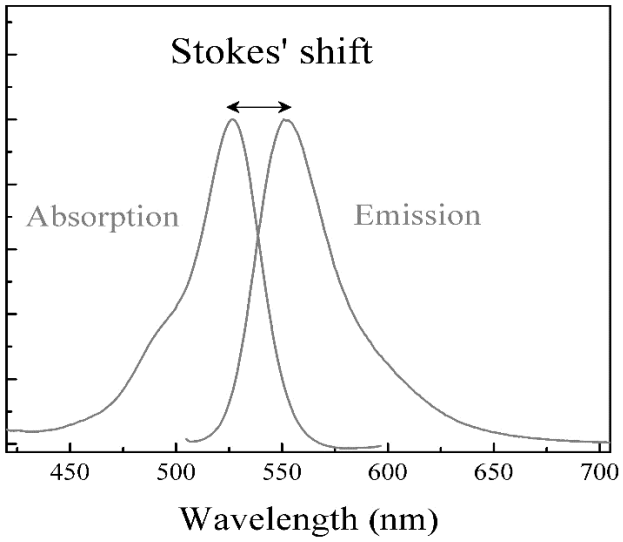


Figure 2 The Stokes' Shift The shift in spectral wavelength between the absorption (blue) and emission (red) spectra.

A fluorescent microscope is designed to deliver a pre-determined wavelength of excitation light to the sample and to detect the emitted fluorescence. The intensity of this emission is proportional to the number of photons received from the fluorescing sample. The efficiency with which the fluorophore emits photons depends on the balance between the radiative and non-radiative relaxation rates and is defined as its quantum yield (Φ):

$$\Phi = \frac{Number\ of\ emitted\ photons}{Number\ of\ absorbed\ photons}$$

The maximum yield a fluorophore can approach is therefore one, i.e. it emits one photon for every photon it receives, which would require negligible non-radiative decay.

The quantification of the intensity of the fluorescent signal is a key measurement technique in fluorescence imaging, since it is proportional to the levels of concentration of the fluorophore (if the quantum yield is fixed), and therefore to the amount of material that has been stained, or the level of fluorescence protein production in live samples.

Every fluorophore species has its characteristic excitation and emission spectra. These are usually a mirror image of one another, a phenomenon aptly named 'The mirror image rule' (Ratsep et al., 2009).

2.3 One and Two Photon Systems

While fluorescent samples can be excited and imaged with a simple light microscope fitted with a fluorescent lamp and the appropriate filters, superior image contrast in biological tissue can be obtained through the use of laser scanning confocal or multiphoton systems. With traditional fluorescent lamp-based applications, the entire subject is illuminated, exciting fluorophores present throughout a sample, and this leads to a large background signal from outside the plane of interest to be recorded by the photodetector (typically a camera) of the microscope.

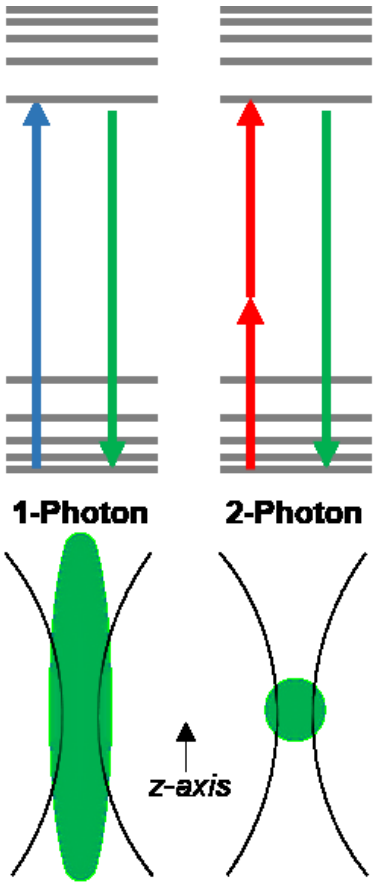


Figure 3 Single and Multiphoton Excitation. Examples of the energy transitions (above) of 1-photon confocal and 2-photon imaging systems, the latter using two photons of half the required energy compared to a confocal system. The diagram below shows the focal plane in green of the excited area of the sample. The 2-Photon, single point of illumination allows for the absence of a pinhole, as well as reduces unnecessary excitation of the rest of the sample.

In a single photon-excited confocal microscope, the sample is excited with laser focussed to a spot that also excites the sample along the z-axis outside the focal region. By imaging the spot of excited fluorescence onto a pinhole at the detector, it is possible to discriminate in favour of light emitted from the focal spot and reject the out of focus back ground light. This is described as confocal detection. Rapid scanning of the focused excitation spot, or of the sample, then allows for optical sectioned images to be acquired. 3-D images can then be assembled from z-stacks of optically sectioned images. In scattering media such as biological

tissue, photons from outside the focal plane can be scattered through the detection pinhole and this limits the imaging depth in tissue to ~100 microns.

In two-photon (2P) systems, the fluorophore is excited by photons of approximately half the required excitation energy that are focused to a spot. This requires two such photons to be absorbed simultaneously such that they have a similar effect as one photon of twice the energy. The probability of two photons arriving simultaneously is low and so high intensity radiation is required. This is typically provided by a mode-locked, femtosecond laser, which produces pulses of light with high peak intensity with relatively low average power at the required wavelength, which is typically in the near infrared. Because the beam is focussed, the intensity is highest in the focal plane and the power can be set such that the intensity is only sufficiently high at the focus to excite significant fluorescence. Since all the excited fluorescence must then originate from the focal plane, there is no need to use a confocal detection pinhole for two-photon (or multiphoton) excitation microscopy. This increases the imaging depth in scattering media such as biological tissue because even scattered fluorescence photons contribute to the useful signal. Furthermore, as the intensity of the longer wavelength photons delivered through two-photon (2P) systems are insufficient to excite fluorescence outside the focal plane, 2P imaging is substantially less prone to photodamage and photobleaching than confocal microscopy, whereby continued out of focus excitation of a fluorophore causes either biological trauma or a bleaching of fluorescent signal respectively. 2-Photon also extends the imaging depth into tissue samples, especially in highly scattering media such as neural tissue, because the longer wavelength excitation photons are less strongly scattered. This makes this 2P microscopy advantageous within this project as samples progress from cell monolayers grown on glass coverslips (readily imaged with confocal techniques) and into thick sections, requiring relatively low signals to be recorded from deep neurons.

2.4 FÖRSTER RESONANCE ENERGY TRANSFER (FRET)

Named after the physicist who first described it, Förster resonance energy transfer (FRET) has become an invaluable tool for probing molecular structure and dynamics - particularly cell signalling pathways and protein interactions (Förster, 1948; Jares-Erijman and Jovin, 2003; Padilla-Parra and Tramier, 2012). It represents the non-radiative transfer of energy from an excited fluorescent protein, the donor, to another fluorophore, the acceptor, in close proximity – typically within ~10nm of one another (depicted in figure 4). Thus a sample can be irradiated with light tuned to excite just he donor fluorophores and the acceptor fluorophores will become excited if (and only if) the conditions for FRET are met.

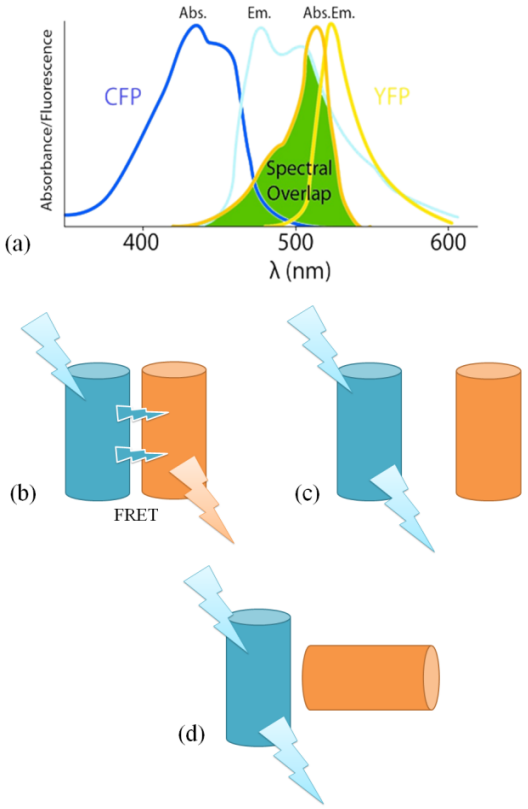


Figure 4 Conditions required for FRET a) A spectral overlap must be present in order for the donor emission (CFP) to excite the acceptor (YFP). (b) FRET occurring when both fluorophores are within range and correctly orientated. (c) and (d) display a lack of FRET due to the distance being too far apart, or the wrong orientation respectively.

These conditions are typically listed as: 1) the close proximity of the fluorophores (typically <10nm), 2) a overlap of the donor emission and acceptor excitation spectra (for example CFP and YFP respectively) and 3) non-orthogonal orientation of the fluorophore dipoles (see Figure 4).

The efficiency of this energy transfer depends on the distance between the donor and the acceptor, as described by the following equation:

$$E = 1/\left(1 + \left(\frac{r}{R_0}\right)^6\right)$$

Where *E* is the FRET efficiency, *r* is the distance from the donor to the acceptor and R_0 is the Förster radius, which can be calculated using:

$$R_0 = [c\kappa^2\eta^{-4}\varphi_d\varepsilon_a J(\lambda)]^{1/6}$$

Where κ is the donor and acceptor dipole alignment, φ_d is the donor quantum yield (defined as number of photons emitted/photons absorbed), ε_a is the acceptor absorption coefficient and J(λ) is the degree of overlap between donor emission and acceptor excitation.

For FRET readouts, the donor and acceptor fluorophores can be arranged in accordance to the desired mechanism of probing; typically, either bound to two separate entities that FRET when coming into close proximity (intermolecular FRET), or both attached to a single protein that undergoes some conformational change, e.g. upon binding a ligand, that structurally brings the fluorescent proteins together or moves them apart (intramolecular FRET).

There are a number of ways to detect FRET that can be implemented with a standard fluorescence microscope. These include donor quenching, spectral unmixing and spectral ratiometric measurement of intensity. The latter is the most common and simplest method, and entails measuring the fluorescence intensity in two spectral channels, one set for the donor emission and the other for that of the acceptor. Upon occurrence of FRET, the donor loses energy to the acceptor, resulting in a signal decrease, while a simultaneous increase is seen in the acceptor channel.

This ratio of acceptor to donor intensity serves as a measure of FRET, allowing for imaging of compartmentalisation of signal, and can be implemented at high acquisition speed. The principal drawback of this technique is the spectral bleed-through of the donor emission into the acceptor emission channel, since there is often a significant spectral overlap between donor and acceptor emission spectra. This can lead to errors in the apparent FRET signal: as donor signal decreases and acceptor signal increases during FRET, the donor bleed-through decreases the acceptor emission channel intensity, thus countering the increase in acceptor intensity. A further issue is that the acceptor fluorophores can be directly excited by the donor

excitation radiation, thereby producing a false positive apparent FRET signal. These issues have been addressed by the integration of correction techniques, several of which have been published (Boerner et al., 2011; Chen et al., 2006), but typically revolve around the generation of coefficients derived from the fluorescent signals in the presence and absence of each fluorophore.

2.5 FLUORESCENCE LIFETIME IMAGING MICROSCOPY (FLIM)

As previously described, the emission of fluorescence results from electrons relaxing from the excited electronic energy level S1 to S0, the ground state. The fluorescent lifetime is defined as the average time a fluorophore stays in its excited energy state.

There are two forms of relaxation to ground state, as mentioned previously, radiative (fluorescent, κ_f) and non-radiative (non-fluorescent, κ_{nf}) decay, as seen in Figure 1. The former is dependent on the electronic energy level structure of the molecule, whereas the latter represents thermal relaxation pathways such as internal conversion or collisions with solvent molecules. Once excited, a fluorophore can undergo either decay pathway, and so the lifetime (τ) of the S1 state is proportional to the sum of the rates of both forms of relaxation as they depopulate it. The total decay rate is the inverse of the fluorescence lifetime:

$$\tau = \frac{1}{\kappa_f + \kappa_{nf}}$$

This can be determined by measuring the (exponential) fluorescence decay profile Measurement of this lifetime of excited fluorophores is intrinsically useful in the field of fluorescence microscopy. The classical measurement of intensity for measuring levels of fluorescence in a sample is simple, yet is subject to a number of factors introducing artefacts into quantification. For example, a biologist wishes to compare levels of a fluorescently tagged protein of interest in two adjacent cells. The absolute values of intensity based on the detection with a confocal microscope in pixel values could be directly compared. However, if one cell happens to express more copies of the genetically-encoded fluorophore, or if many of its

fluorophores have been photobleached during imaging or lie outside the excitation/detection volume (e.g. out of focus), a false comparison can be made due to the observed lower level of intensity.

Fluorescence lifetime imaging microscopy (FLIM) overcomes many potential artefacts of intensity-based imaging by being almost entirely independent of brightness (*almost*, as there must still be sufficient signal to collect enough photons for measurement).

There are still, however, some factors that can impact lifetime measurements *in situ* including changes in states of temperature, molecular interaction, pH, etc., that can change the fluorescence lifetime of some fluorophores. However, these environmental parameters can be controlled for in an experiment and, indeed, fluorescence lifetime can be used to measure such parameters, as seen in Szmacinski and Lakowicz (1993) whereby FLIM was used to directly measure pH changes.

2.5.1 Time-Domain FLIM

The principal of TCSPC is illustrated in Figure 5: the fluorescent target is excited by a pulsed laser and the arrival times of each detected photons is recorded relative to the excitation pulses. As the decay of the fluorescence is known to be exponential, the fluorescent lifetime decay curve can be calculated by binning photons into relatively few time points along the lifetime, creating a histogram of the photons' arrival times at the detector, and fitting these to an exponential decay profile.

To accomplish this measurement in a typical TCSPC-FLIM system, the excitation pulses will trigger a photodiode to provide a 'start' signal, initiating a voltage ramp in a time-to-amplitude converter (TAC). When the first photon from the excited sample is detected following the excitation pulse, this voltage ramp is stopped. The difference between these start and stop signals is propagated as a proportional voltage output to an analog-to-digital converter (ADC) resulting in an "arrival time" being stored for the received photon. Over repeated measurements and excitation pulses, the fluorescence decay profile is gradually built up until there are sufficient detected photons to provide an accurate lifetime measurement. The requirement to detect no more than one photon per excitation pulse , combined with the sequential measurement of each image pixel in a laser scanning microscope results in relatively slow imaging compared to other forms of fluorescence microscopy, typically requiring 30 seconds to one minute of photon collection per fluorescence lifetime image (Becker et al., 2004).

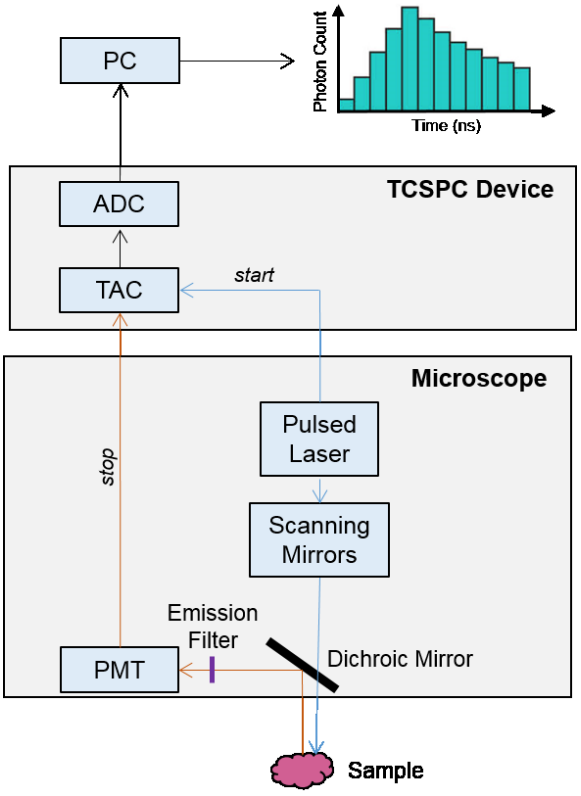


*Figure 5 Schematic of a TCSPC FLIM system.*A pulsed laser is used to illuminate the sample and excite the fluorophore, whilst a 'start' signal is sent to the time-to-amplitude converter (TAC). The emitted photons from the sample are directed to a photomultiplier tube (PMT) and once the first photon is received by the TAC, stop signal is generated. The difference between start and strop are then passed to the analog to digital converter (ADC) whereby a time channel is generated and sent to a computer (PC) for recording the histogram of arrival time vs. number of photons.

2.5.2 FLIM-FRET

FRET can be read out by measuring the reduction in the fluorescence lifetime of the donor fluorophore since an excited fluorophore population will decay faster when FRET offers an additional way to lose energy (see Figure 6). This means that only the donor signal need be

recorded from and even a fluorescently ‘dark’ acceptor can be used The combination of FLIM and FRET is a powerful tool when studying the dynamics of proteins and interacting signalling pathways within living samples. As described in section 2.4, FRET facilitates the probing of complex systems at a molecular level, however, its measurement via ratiometric, intensity-based readouts carries the limitations of intensity-based fluorescent imaging. These limitations may not be significant in a sample with excellent optical clarity and minimal sample thickness (for example, a cell monolayer grown in culture onto glass), but the signal to noise ratio associated with weaker signals originating in deep tissues and presenting small fluorescent changes make reliable intensity-based readings problematic. FLIM provides a more robust readout that is independent of fluorescent intensity. When coupled with the penetration-power of multiphoton microscope systems, 2P-FLIM-FRET provides a powerful tool for reading out FRET biosensors *in vitro* or *in vivo*.

Since multiphoton excited FLIM can provide relatively robust signals from FRET biosensors expressed deep within tissues, it is a good choice for quantitative studies of cAMP in neuronal pathways, including those underlying learning and memory.

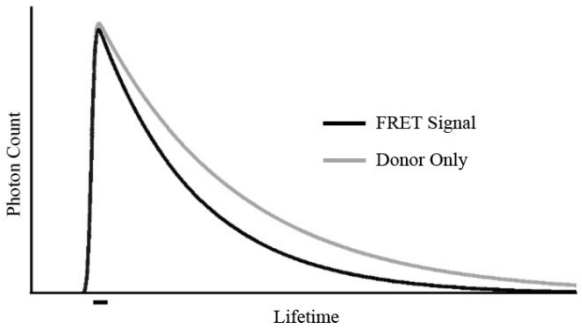


Figure 6 Example FRET lifetime response Simulated fluorescent lifetime readings from a blue-yellow FRET pair. Due to the acceptor absorbing photons during FRET, we see a decrease in the lifetime of donor signal (black) compared to when imaged alone (grey). Bar represents laser pulse.

3 LEARNING AND MEMORY

The mammalian brain is a truly remarkable organ, a nervous centre capable of computing near infinite possibilities and controlling a vast range of functions. A typical human brain consists of approximately 100 billion neurons, while the mouse bears around 70 million (Herculano-Houzel et al., 2006). Over a century ago, Cajal described the junctions (Ramon y Cajal, 1894), or synapses as Sherrington named them (C.S. Sherrington, 1897), that allow for information to pass between neurons to allow for this complex network of computing units to provide its sheer cognitive power. Each neuron carries, on average, 1,000 synaptic connections to other brain cells, providing massive inter-communicative patterns of activity capable of storing immense quantities of information (Sirevaag and Greenough, 1987).

3.1 THE SYNAPSE

The junction at which information passes from one neuron (the pre-synaptic) to another (the post-synaptic) is the synapse, a femtolitre structure consisting of a pre-synaptic bouton and a post-synaptic density (PSD), separated by a synaptic cleft approximately 20nm across (Kandel et al., 2001; Schikorski and Stevens, 1997).

The most common locations are found to connect the axon to the adjacent dendrite, giving rise to the classical view of neuronal information transfer: the action potential from an excited neuron travels to the synaptic point along its axon; the resultant membrane depolarisation then causes calcium influx via ionic channels opening at the synapse. This high calcium concentration causes synaptic vesicles to dock with the membrane at the synaptic cleft, in turn releasing their contents (neurotransmitter) which binds to receptors at the post-synaptic membrane which in turn can open further ion channels to modulate its membrane potential, or may recruit some further action of a secondary messenger. This essentially allows for the conduction of an electro-chemical signal to traverse between cells, where it may ultimately excite or inhibit the recipient neuron.

The most common synapse is the excitatory glutamate-releasing variety (Elias and Nicoll, 2007), where the neurotransmitter glutamate is detected by two types of ionotropic channels: α-amino-3-hydroxy-5-methyl-4-isoxazole propionic acid (AMPA) (Luscher et al., 1999) and N-methyl-D-aspartate (NMDA) receptors (Carroll et al., 1999).

3.1.1 The Pre-Synaptic Site

The axonal side of the synapse, consists of a swelling termed the *bouton*, situated either along the process itself, the *en-passant bouton* (EPB), or at the end of a branching process, a *terminaux bouton* (TB). After receipt of membrane depolarisation, the action potential, and the resulting influx of calcium via voltage-gated channels, the ~50nm, neurotransmitter-packed vesicles begin their cycle of docking with the pre-synaptic membrane, as well as the endocytosis of emptied vesicles, followed by the re-absorption of excess transmitter (Greengard et al., 1993). This process of membrane fusion requires a complex of specialised SNARE proteins (Soluble N-ethylmaleide-sensitive factor attachment protein receptor). These consist of specialised vesicular variants, such as the VAMP (vesicle associated membrane protein) family, as well as the targeted proteins such as syntaxin (Sollner et al., 1993).

3.1.2 The Post-Synaptic Site

The dendritic side of the synapse, consisting of the protein-dense post-synaptic density (PSD), typically manifests at the spines of the dendritic branches. These long, filopodia-like processes extend from the dendritic shaft and have long been a target of interest in synaptic plasticity due to their rapid turnover and easily classifiable characteristics, namely morphology, length and shape. Scaffolding proteins, such as the Shank family (Sheng and Kim, 2000), help to align and maintain the pre- and post-synaptic membranes, ensuring neurotransmitter-release in turn reaches its destination receptors across the cleft. The existing research on synaptic plasticity also looks to the PSD for its high number of neurotransmitter receptors, namely NMDA and AMPA, and their strong affiliation to the induction of long-term memory.

3.2 SYNAPTIC PLASTICITY

In 1949, Donald Hebb proposed that memories are stored essentially in patterns of activity between populations of neurons. This also gave rise to the concept of synaptic strengths being directly correlated to adjacent cell activity, or as it is often colloquially summarised: “cells that fire together, wire together” (Lowel and Singer, 1992).

Upon experience-driven learning, the synaptic sites along both axons and dendrites can change at different levels, from subtle changes in the weighting of synaptic connections, differing in strengths of communication, to whole structural remodelling, consisting of the generation, elimination and stabilisation of synaptic sites. These constant morphological alterations give rise to an ever-changing neuronal architecture, aptly named synaptic plasticity.

The refinement of Hebbian learning concepts in the 1940s (Hebb, 1949; Konorski, 1948) indicated the existence of physical changes occurring at the synaptic level upon learning and memory. In 1973, two papers (Bliss and Gardner-Medwin, 1973; Bliss and Lomo, 1973) demonstrated the first observations of physiological changes in the rabbit brain that lasted long enough to be deemed a stable and resilient source of memory. The resultant phenomenon, named long-term potentiation (LTP) was then identified throughout excitatory pathways across the mammalian brain, in particular the hippocampus (Alger and Teyler, 1976; Doyere and Laroche, 1992; Yamamoto and Chujo, 1978), a region attributed to long-term memory storage.

The experiments elucidating LTP revolve around high-frequency stimulation of monosynaptic neuron pairs, portraying a long lasting (>1hr) increase in synaptic strengthening after just milliseconds of stimulation (Morris et al., 1990) *in vitro*, increasing to days *in vivo* (Teyler et al., 1977).

Experience-dependent plasticity has since been detected across many systems including visual and somatosensory (Fox and Wong, 2005), and has become a leading and somewhat unrivalled theory of memory acquisition and retention. Initially, the question was set out to

address whether it was the number of synapses or their individual strength that contributes to memory networks being established. This now appears to be answered as connections have been observed to modulate in accordance with stimulation, as well as the mass up-regulation of synaptogenesis upon learning tasks (Bailey and Kandel, 1993; Greenough and Bailey, 1988; Xu et al., 2009; Zuo et al., 2005). This synapse-counting approach is fraught with difficulties, mostly arising from cortical circuits not being easily isolated to ensure synaptic density measurements are not confounded by other overlapping circuits.

The mechanisms behind LTP have long been studied, with an abundance of research being carried out at the post-synaptic density, with the redistribution of glutamate receptors at the synaptic membrane.

LTP appears to be established at the point of an increased calcium concentration within the PSD, as concluded by the prevention of LTP upon inhibition of calcium influx (Mulkey and Malenka, 1992), and the overloading of calcium directly inducing it (Bliss and Collingridge, 1993).

Initially, the inhibition of NMDA activity purported a reduction in LTP incidence (Collingridge et al., 1983), and this finding, coupled with observations of NMDA activity driving calcium influx via voltage-gated channels (Ascher and Nowak, 1986) led to the conclusion that plastic changes require an NMDA component. However, NMDA has been shown to not directly cause LTP if activated solely; requiring further intracellular calcium activity in conjunction with NMDA-induced calcium influx to induce LTP.

AMPA receptors have also been described in the LTP pathways. While it is classically viewed that AMPA mediates fast transmission in neuronal communications, in contrast to the long-lasting effects of NMDA modulation, there is growing evidence that an increase in the number of AMPA receptors at the post-synaptic membrane could be required in order for LTP to occur (Davies et al., 1989; Isaac et al., 1995).

The discovery of LTP and LTD indicated not only changes in cellular signalling cascades, but also large, morphological changes in synapse number and size, leading to the investigation of synaptogenesis at specific sites along the axon (en-passant and terminaux boutons) and dendrite (spines). The advent of electron microscopy, pushing microscopic resolution to the atomic level, greatly advanced our understanding of synapses, allowing for the direct observation of the connections between specific processes (Knott et al., 2006). This increased resolution (on a picometre scale, as opposed to the nanometre scales of light microscopy limits) has allowed for the visualisation of size changes at the level of existing synapses, reflecting the precise tuning of existing connections in response to experience-dependent activity. Of particular interest is the correlation of the increase in synaptic volume with an increased synaptic strength (Cheetham et al., 2014; Yuste and Bonhoeffer, 2001). This allows for an inherent readout of connectivity alteration based on morphological data acquired from *in vitro* and *in vivo* microscopy.

Synapses are incredibly heterogeneous organelles with thousands of molecules packed into submicron volumes. How these synaptic molecules are organised, let alone the way they are assembled and remodelled during synaptic plasticity, still carries major gaps in our understanding of brain function. The processes underlying synaptogenesis are being studied in great detail at the molecular level, with entire proteomes being generated for their cytoskeletal scaffold alone (Bayes et al., 2011).

Neurons direct proteins required for synaptogenesis to a new connection point. This includes vesicles, neurotransmitter receptors and synaptic machinery (Ahmari and Smith, 2002; Garner et al., 2002; Ziv and Garner, 2001). While the scaffolding complexes and underlying processes governing the coupling and differentiation of pre- and post-synaptic sites have been well researched in the developing central nervous system, the signalling pathways controlling the presynaptic strength and structure are still being investigated in the adult brain.

3.3 SYNAPTOPATHOLOGY

As the complexity and computational functions of the brain are almost entirely due to its level of interconnectivity, it follows that any impairment at the synaptic level could lead to problematic brain function. Since the discovery and characterisation of the synapse, a vast range of neurological and psychiatric disorders have been attributed to the synapse, a field labelled collectively as 'synaptopathology' (Brose et al., 2010). The field now includes dementias such as Alzheimer's disease (Oddo et al., 2003; Selkoe, 2002; Terry et al., 1991), but also neuropsychiatric conditions now attributed to synaptic developmental impairments, including autism spectrum disorders (Pinto et al., 2010), fragile-X (Jamain et al., 2003) and schizophrenia (Kirov et al., 2012; Selemon and Goldman-Rakic, 1999). The majority of studies take the post-synaptic site, the dendritic spine, as the model of disease. Indeed, Alzheimer's disease as has been now strongly correlated to a marked loss of spines, understandably producing the hallmark symptoms of memory loss and confusion. Conversely, the excessive gain of spines has been identified as a pathway involved in the development of autistic spectrum disorders (Hutsler and Zhang, 2010).

The pre-synaptic boutons are relatively understudied in synaptopathologies, possibly due to their difficulty to classify and monitor, in comparison with well modelled and observable traits seen in dendritic spines. However, as the inception of interneuronal communication lies within the neurotransmitter-packed vesicles within the pre-synaptic bulb, going on to dock with the membrane and exocytose into the synaptic cleft; there is an abundance of complex mechanisms and pathways (Takamori et al., 2006) susceptible to failure. One example is the soluble NSF attachment protein receptor, or SNARE, complex, controlling the attachment and docking of vesicles to the active zone (Bennett et al., 1992). This consists a family of proteins including syntaxin and synuclein, both being implicated in the development of Parkinson's disease (Burre et al., 2010; Garcia-Reitbock et al., 2010).

3.4 cAMP AND ITS ROLE IN THE BRAIN

3'-5'-cyclic adenosine monophosphate (cAMP) is a ubiquitous second messenger, driving a wide range of signalling cascades, regulating a plethora of cellular events. Discovered in 1958, it was almost 20 years later, after Brunelli et al. (1976) injected cAMP straight into Aplysia sensory neurons, that cAMP was seen as a key regulator in neural activity.

Kandel's fundamental research specified long-term potentiation (LTP) and long-term depression (LTD) as the drivers of long-term synaptic changes, and went on to identify the role of the cAMP-PKA cascade behind these occurrences (Abel et al., 1997; Frey et al., 1993b; Huang et al., 1994; Kandel, 2012; Schacher et al., 1988).

The basis for this research was discovered when Aplysia were stimulated with serotonin resulting in an increased intracellular cAMP concentration, along with activation of PKA, a cAMP-binding protein. After extended stimulation, an enduring activation pattern of cAMP drives more durable alterations of synaptic plasticity (i.e. LTP), by causing PKA to recruit p42 MAPK (mitogen-activated protein kinases), whereby nuclear translocation then goes on to activate gene expression via transcription factors, providing longer lasting changes (Kandel, 2001). These are directly driven by the cAMP response element (CRE) (Montminy et al., 1986), found within the promoter regions of these memory-forming genes. Upon CRE activation by the cAMP-PKA derived transcription factor CREB (cAMP response element binding protein) (Montminy and Bilezikjian, 1987) by either PKA, MAPK or CaMK (Montminy, 1997), RNA polymerase then goes on to take up the role of regulating these genes.

PKA-dependent pathways downstream of cAMP have been shown to be crucial in many neuronal processes, especially at the synapse. While LTP has been shown to predominantly require the movement of AMPA receptors in the post-synaptic density, it is also recognised that changes in exocytosis machinery is required at the pre-synaptic side. In particular, the role of PKA in regulating exocytosis and therefore neurotransmitter release has been identified as an integral part of synaptic communication and LTP (Chen and Regehr, 1997; Lessmann

and Heumann, 1997; Seino and Shibasaki, 2005; Trudeau et al., 1996; Weisskopf et al., 1994b). Upon receiving Ca^{2+} influx, calmodulin drives adenylate cyclase production of cAMP, activating PKA in turn (Linden, 1997; Salin et al., 1996). While this appears to be the mechanism of long-term change in the cortex, other brain regions, typically within the hippocampus, portray a different means of pre-synaptic LTP whereby no Ca^{2+} input is required, and a simple phosphorylation is performed by PKA activity, suggesting an even greater significance of its role in neurotransmitter release probability and amount, indicating cAMP as a key orchestrator, rather than an intermediate signalling messenger (Chavis et al., 1998; Linden, 1998), determining release levels from intracellular concentrations of Ca^{2+} (Lonart et al., 2003).

Originally PKA was thought to be the only protein to bind cAMP and initiate its downstream effects, however in 1998 a Rap1 guanine nucleotide exchange factor, named Epac (exchange protein activated by cAMP) was discovered as another protein directly activated by cAMP (de Rooij et al., 1998) (

Figure 7). There is however, a similar probability of cAMP binding to both these PKA and Epac targets, as documented by Dao et al. (2006).

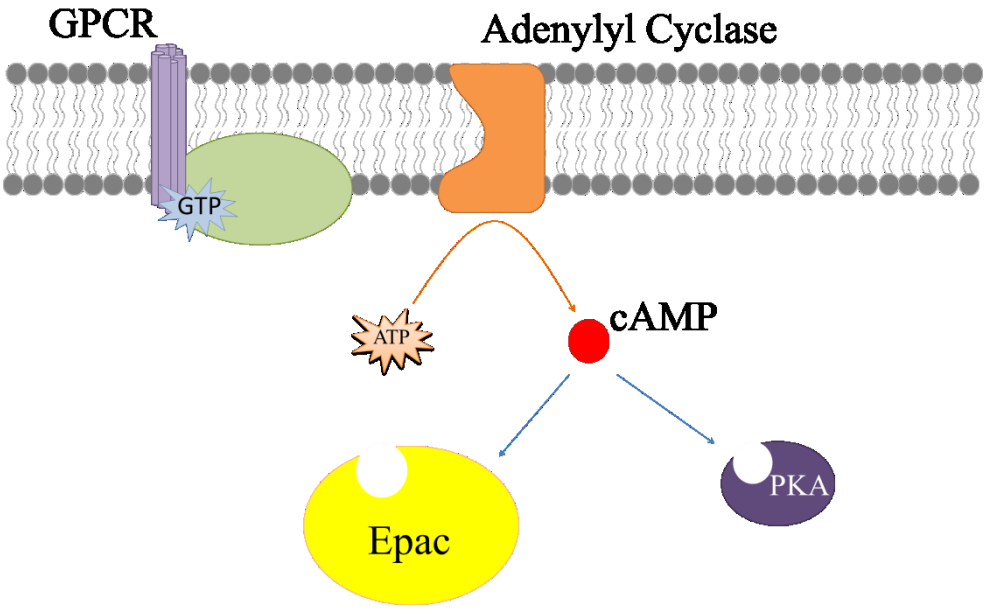


Figure 7 cAMP Signalling Pathway. Upon activation of adenylyl cyclase (e.g. from a G-protein coupled receptor), cAMP is derived from ATP. It then goes on to bind to either protein kinase A (PKA) or exchange protein activated by cAMP (Epac).

Epac's isoforms 1 and 2 are expressed in fairly different patterns throughout mammalian systems. The former, Epac1, is found throughout many thoracic organs including muscle tissues, the kidneys and thyroid (Kawasaki et al., 1998), whereas Epac2 is predominantly found in neural tissues. Once activated by cAMP, Epac's function consists of nucleotide exchange for the Rap family of Ras-like GTPases, hence its alternative name. The binding of cAMP to Epac subunits is highly dynamic, requiring no binding energy, indicating a rapid rate of dissociation (Kraemer et al., 2001).

While there is evidence for a role of Epac within the central nervous system (specifically the Epac2 form), most research following cAMP-mediated neural changes focus on the PKA-dependent pathway. Epac-derived processes have been seen to play a part in neurotransmitter release (Gekel and Neher, 2008; Zhong and Wu, 1991), memory retrieval (Ouyang et al., 2008), levels of dendritic spine morphology (Woolfrey et al., 2009), and a range of other regulatory roles via the Ras superfamily of small GTPases, highlighted in Figure 8.

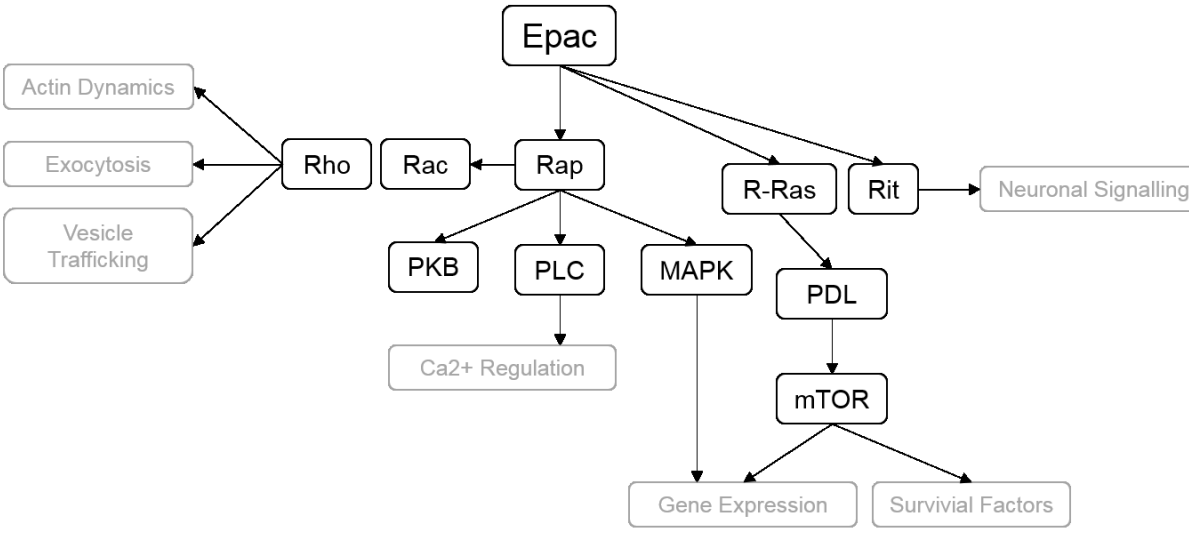


Figure 8 Epac-mediated signalling pathways and functions. Schematic of Epac's downstream effectors and the role it plays in several neurological functions, recruiting protein kinase B (PKB), mitogen-activated protein kinase (MAPK), phospholipase-C (PLC). Rho, Rac, Rap, R-Ras and Rit are all members GTPase members of the Ras family. Adapted from Roscioni et al. (Roscioni et al., 2008).

While cAMP has been seen to orchestrate a wide range of neuronal roles including excitatory modulation (Goldsmith and Abrams, 1992; Pedarzani and Storm, 1993), neurite growth (Ooashi et al., 2005), dendritic spine activity (Hoogland and Saggau, 2004; Pedarzani and Storm, 1993), cortical development (Inan et al., 2006) and synaptic changes at the post-synaptic, dendritic level (Blitzer et al., 1998b; Choi et al., 2002; Esteban et al., 2003; Lee and O'Dowd, 2000; Raman et al., 1996; Tzounopoulos et al., 1998); its roles in synaptogenesis, degradation and modulation at the pre-synaptic, axonal side are still relatively unknown. Most groups have studied its roles in neurotransmitter release (Leenders and Sheng, 2005; Turner et al., 1999), which could underlying pre-synaptic enlargement, yet its direct role in the formation of whole synapses is understudied.

There does appear, however, to be a strong emphasis on the cAMP-PKA pathway (Munno et al., 2003), and studying the spatio-temporal dynamics of cAMP activation in live cortical neurons, axons and boutons could further elucidate the role of this integral driver of neuroplastic changes.

3.5 COMPARTMENTALISATION OF CAMP IN CELLS

Due to its ubiquitous nature, cAMP is found at many locations within the majority of mammalian cell types. Research into the dynamics of downstream, localised processes has found a targeting and anchoring of cAMP-binding proteins, such as PKA (Wong and Scott, 2004), but has also highlighted micro-domains of cAMP itself. This subcellular compartmentalisation has been detected within excitatory cells, including cardiac myocytes and neurons (Di Benedetto et al., 2008; Kotaleski and Blackwell, 2010; Steinberg and Brunton, 2001; Zaccolo and Pozzan, 2002). However, the rapid diffusibility of cAMP molecules through the cytoplasm has given rise to questions of how such compartments can be established and maintained.

Upon being synthesised at the plasma membrane by adenylyl cyclase, cAMP then diffuses throughout the cytoplasm before being degraded by phosphodiesterases. The relationship between these three stages in the life of a cAMP molecule appears to drive this non-uniform cAMP coverage, however it has been suggested that more substantial cytoskeletal barriers may isolate such compartments (Martin and Cooper, 2006; Rich et al., 2001a). In 2005, two groups (Baillie et al.; Lynch et al.) proposed a mechanism of phosphodiesterase activity enforcing compartment perimeters around sites of cAMP synthesis. This interplay of adenylyl cyclase producing cAMP where it is required, followed by spatially immediate degradation would allow for such a precise system of cAMP localisation (Zaccolo, 2006). Within the dendritic spines, such segregation can be preserved by the physical barriers of the spine neck, essentially a narrowing or 'bottleneck' beneath the spine head that impairs free cytoplasmic diffusion (Li et al., 2015). This allows for cAMP to be highly targeted to individual spines undergoing the post-synaptic changes required for LTP.

3.6 FLUORESCENT PROBING OF SYNAPTIC STRUCTURES

Previously, the study of a signalling molecule required the use of cell assays, first running the experiment on cells in culture and then adding a lysis buffer at pre-determined intervals. The lysate could then be purified and analysed for scintillation counting, or ELISA procedures

(Brooker et al., 1979). This, however, is not only time consuming, costly and limited to the temporal resolutions that the experimenter is willing to attempt, but also entirely lacks spatial resolution, producing whole-cell population values.

The development and use of fluorescent probes for such targets has since become commonplace with the advent of faster imaging techniques and the discoveries of mutated fluorescent proteins to allow for spectral changes in response to molecular activity (Griesbeck, 2004; Miyawaki, 2003; Zhang et al., 2002).

Due to its vitality in the functioning of neuronal pathways, studies of the synapse have long been attempting to unravel roles of many signalling molecules and binding proteins, and as the neuron is such a highly functionally polarised structure, spatial resolution has been of key importance.

An excellent example of FRET-FLIM in synaptic research is detailed in Lee et al. from 2009. The group, led by Professor Ryohei Yasuda, a pioneer in neuroscientific fluorescence probing, developed a FRET sensor for calmodulin-dependent protein kinase II (CaMKII), a calcium-dependent kinase known to be required for synaptic plasticity (Takao et al., 2005). By stimulating individual dendritic spines with localised glutamate release, the lifetime shifts from their FRET sensor could be visualised and compared to the adjacent, unstimulated spines. A figure from the paper is shown below in Figure 9. The spatial resolution provided by multiphoton imaging of neural tissue sections, with a sensitive FRET sensor provided unparalleled insight into CaMKII activity at activated spines.

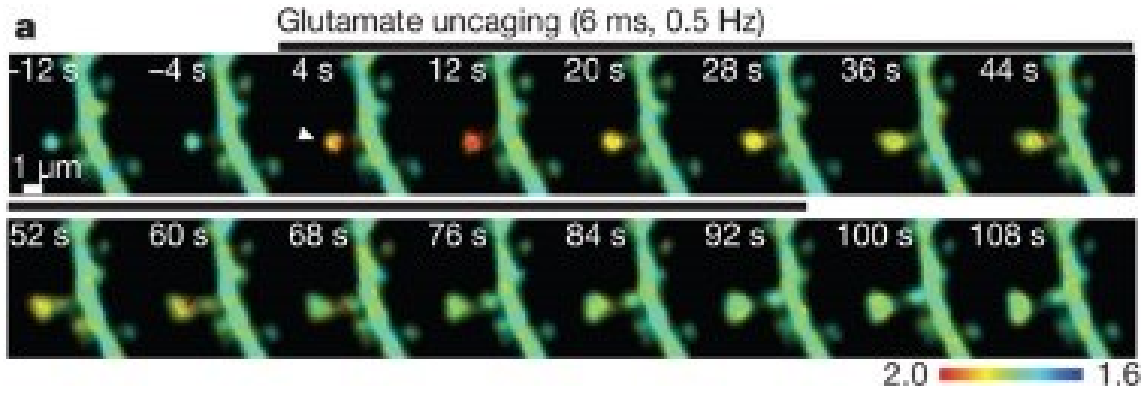


Figure 9 Dendritic response to glutamate uncaging with a CaMKII sensor. Note the isolated signal in the dendritic head that has been stimulated, coupled with marked morphological size changes. Taken from Lee et al. 2009.

The majority of studies surrounding synaptic plasticity have focussed on the post-synaptic site, the dendritic spines (Chen and Sabatini, 2012; Murakoshi et al., 2011; Rizzo et al., 2004; Vanderklish et al., 2000; Yagishita et al., 2014; Yasuda, 2006). While mechanisms of LTP are well characterised at this site, and thus make it an attractive structure to investigate, technical advantages over the pre-synaptic site also play a role: the changes are large and turnover is rapid, thus allowing a relatively low spatial resolution system to record robust structural changes.

This project turns to pre-synaptic terminals, in particular the *en-passant bouton* (EPB), and applies these well characterised fluorescent probing techniques. Previous research into EPBs with FRET sensors have typically been in drosophila, a species that is remarkably simple to breed, genetically manipulate and image with minimal penetration difficulty. Such studies have looked at the motor-synapse, a readily available site of neuronal pre-synaptic terminals synapsing to muscle fibres, and have observed neuronal communications via calcium signalling with a TroponinC FRET sensor. (Guerrero et al., 2005; Mank et al., 2006; Shakiryanova and Levitan, 2008).

Studies at mammalian presynaptic sites have been mostly investigating the SNARE proteins in the docking and release of vesicles (Degtyar et al., 2013; Pennuto et al., 2002) as well as

the increased energy requirements at the synapse, necessary to drive the constant machinery dedicated to synaptic transmission (Pathak et al., 2015).

While the pre-synaptic mechanisms of LTP revolve around the dynamics of synaptic vesicles (it is here that the point of synaptic transmission commences after all), the action potential-induced calcium influx resulting in increased synaptic docking is still relatively understudied. The role of cAMP, a comparatively early signalling molecule in the synaptic transmission and strengthening process, is of particular interest in these systems.

4 AIMS OF THIS PROJECT

This project set out to develop a robust system for imaging cAMP dynamics in live neurons with the most sensitive fluorescent probes available. Previous literature describes a vital role for cAMP in the pathways underlying synaptic plasticity and ultimately the processes by which we learn and retain memories. This role has been characterised primarily from general modulation with pharmaceutical agents, resulting in widespread changes suggesting the necessity for cAMP in the strengthening of synapses.

The existing knowledge in the field relies predominantly on indirect measurements, insensitive to the spatial dynamics of this ubiquitous signalling molecule, with suggestion of compartmentalisation within neuronal cell types, but not combining measurements of cAMP activation with its subcellular localisation.

With the appropriate FRET sensor, an optimised microscopy setup and a live cell sample that reflects the natural, neural environments as closely as possible; this project aims to fuse the previous observations of increased synaptic size and strength changes upon long-term plasticity, with some of the latest techniques in live cell fluorescence imaging microscopy to study the spatial and temporal cAMP dynamics in axons and pre-synaptic terminals.

4.1 EXPERIMENTAL OUTLINE

The project consists broadly of two phases: first optimisation, then data collection. The first stage entailed the selection of neuronal cultures that would allow for a compromise of accessible, live cell imaging with the unhindered representation of the mammalian brain, still capable of undergoing unstimulated synaptic plasticity. Next, an appropriate system was optimised for imaging cultures along with a means for perfusion with solutions and drugs.

To measure cAMP, FRET sensors were acquired from the National Cancer Institute in the Netherlands, and these candidate sensors were screened, first in HEK cells and then in

primary neuronal cultures. After the best sensor was selected, the project moved into organotypic slice cultures, utilising a multiphoton imaging system combined with fluorescence lifetime microscopy.

Once the optimisation of FRET-FLIM recordings was completed, the next phase of data collection began, imaging slices over a 90 minute time period (a length determined from the time OSCs can spend out of incubation) and recording the readout from the FRET sensor in neurons.

Post-processing and image analysis could then combine the morphological changes occurring at the synaptic cytoskeletal level, with the cAMP concentrations in different intracellular microenvironments from the FRET sensor.

The optimisation workflow is depicted in the schematic below, in Figure 10.

The second phase, of data collection curtailed a large *n* of axonal processes from as higher number of different samples as possible, to allow for meaningful averaging of the data collected at each synapse.

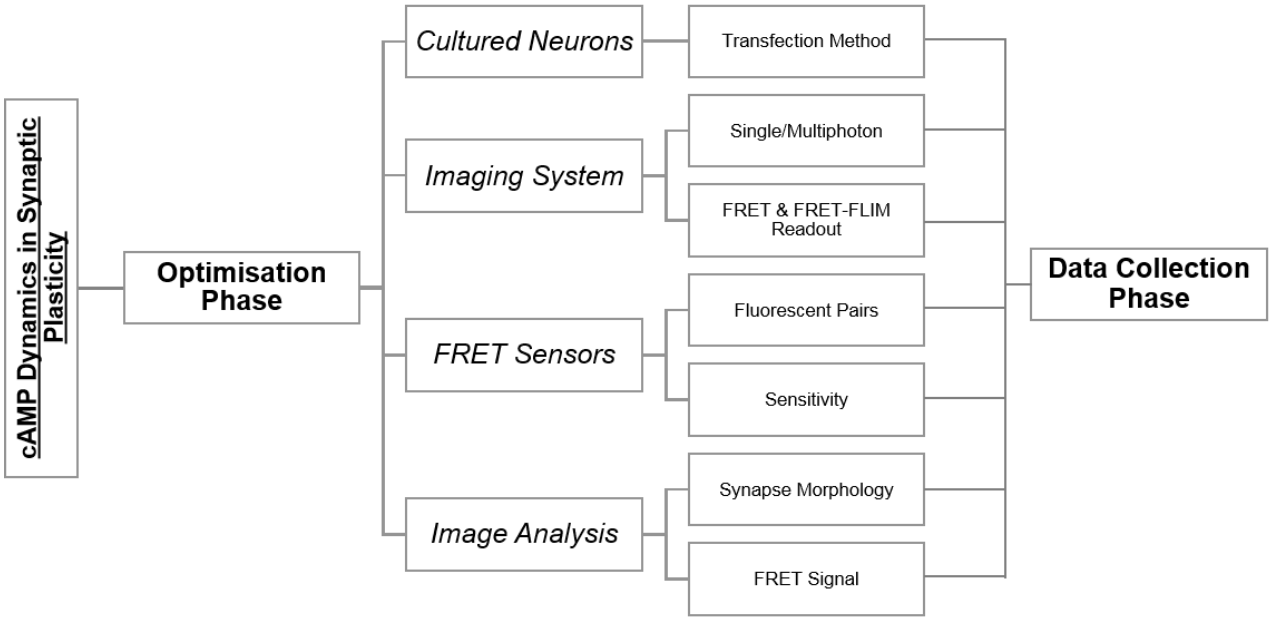


Figure 10 Experimental outline of the project

5 CULTURING THE BRAIN

5.1 THE CHALLENGE

The brain is arguably the most complex organ in the animal body, consisting of trillions of intricate connections between a plethora of different cell types. The ability to study neurons *in vitro* and *ex vivo* is mandatory in understanding how processes occur on a cellular level, with uninhibited microscopic access and ease of manipulation and stimulation of samples.

Culturing neurons has been a part of modern neuroscience for over a century, beginning in its infancy, with the work of Harrison (1910) culturing extracted neurons in a droplet of serum suspended from a coverslip. This technique revolutionised the concept of the neuron doctrine hypothesis, in tandem with Ramon y Cajal's early work, in conceiving that the nervous system is composed of individual, discrete cells, comprising specialised units for processing.

This hanging drop technique was a highly efficient option at the time, offering fully isolated cultures, resistant to contamination and easily viewed by microscope. It was however, severely limited in terms of longevity due to its sealed and therefore finite media supply.

The next instalment came when Carrel (1923) documented the use of culture flasks for neurons, maintaining far larger cultures for a much greater period of time, with the ability to exchange media and control gas exchange.

Two decades later came the advent of the 'roller tube', an advanced form of the test tube capable of rotating to provide light agitation to cultures, promoting better media and gas exchange (Hogue, 1947). At this point, slices of brain tissue (organotypic slice cultures, OSCs) as well as cell cultures could be grown for several months without deteriorating, providing much of the basis for modern neuronal tissue culture today.

Further to culturing OSCs, the above method utilises the tissue bound to a coverslip (known as the 'flying coverslip' technique) that is free to move within the half-filled, rolling tube

(Costero and Pomerat, 1951). The other mainstream alternative to maintaining OSCs is via a chamber system, with the slices grown on membrane inserts within dishes or the wells of a plate. This latter system is mostly used in this project, providing ideal gas/media exchange dynamics, as well as excellent longevity showing slices to maintain healthy connections and plastic changes up to six months post-preparation (Gogolla et al., 2006b).

Primary cultures, that is, cells extracted from whole organisms and then cultured *in vitro*, can be traced back over a century to the very origins of cell culture and the identification of the need for nutrients to be provided in order to promote and maintain healthy, *ex vivo* preparations. For neurons, the brain of animal may be extracted, dissociated and then seeded to live for several months (Kaneko and Sankai, 2014; Kumar and Mallick, 2016). Typically, brains are taken at the late embryonic stages, the rationale being a time point prior to the point of extensive axonal and dendritic branching, and thus minimising damage and cell death during transplantation (Banker and Cowan, 1979). One immediate challenge, specific to neurons, is their inability to replicate and thus cultures are inevitably finite. Due to the coexistence of neurons with their supportive glial cell types (which do divide), cultures are often administered anti-proliferation concoctions (such as AraC) to inhibit survival of contaminant cell types to produce solely neuronal cultures. However, the presence of astrocytes and oligodendrocytes are relatively minimal anyway, due to their production commencing relatively late in embryonic development (Gilmore and Herrup, 1997).

Primary neuronal cultures typically consist of hippocampal regions, due primarily to the abundance of well-characterised cell types for study (namely pyramidal neurons), however cortical, cerebellar or combinations of regions is also commonplace for studying different cell types.

Levels of synaptic turnover and plasticity in *in vitro* cultures varies between types of culture and the conditions they are maintained in, as well as the stages of development and maturation either of the source animal prior to dissociation or age of culture *in vitro*. In OSCs, electrophysiological recordings show not only typical synaptic transients (Debanne et al.,

1998; Debanne et al., 1995), but also synaptic plasticity, including activity-driven synaptogenesis and elimination (Bastrikova et al., 2008; Bonhoeffer et al., 1989; Vlachos et al., 2012). In primary cultures, plasticity and LTP has been observed in the movement of glutamate receptors (Carroll et al., 1999; Lu et al., 2001), yet due to the monolayer-basis of cultures, the number of intersecting processes is infrequent, and thus synaptic contact is relatively rare, especially given the shorter length of time in culture, reducing the full time span of development.

Human embryonic kidney cells (HEKs), are often used in the initial screening and testing of mammalian plasmids and expression vectors. These cells are straightforward to culture, resilient to stress and possess all the necessary machinery to express plasmids, they therefore provide an ideal system to screen the fluorescent probes used in this project. They also express the adenylate cyclase receptors required for cAMP production (however the role of cAMP differs, due to their renal nature), and thus react accordingly to the same stimulation protocols as would be used on neuronal cultures.

This project makes use of several different forms of culture, becoming more advanced in tandem with the imaging equipment used to visualise cAMP-derived FRET changes.

5.2 TRANSFECTION METHODS

Inserting the sensor into the appropriate culture medium requires a tailored method for its respective sample. In the case of cell cultures, including the HEKs and PNCs, this can be done chemically with reagents such as PEI and Lipofectamine 2000. These systems form lipid rafts with the DNA of interest and aid in ‘carrying’ it across the plasma membrane to nuclear targets for expression.

However, for the OSCs, this system lacks the penetration to label neurons reliably, and so an alternative method was sought after.

Three techniques were trialled: electroporation, viral transduction and biolistics.

5.2.1 Electroporation

The concept of electroporation revolves around the transient and reversible formation of micropores (20-120nm in diameter) throughout the plasma membrane, rendering it temporarily permeable to foreign matter (Neumann and Rosenheck, 1972; Teruel and Meyer, 1997). The technology is now commonplace for the transfection of genetic material into cell cultures and some tissues, however its use in transfecting neurons in tissue is relatively rare, typically requiring complex targeting of individual neurons via a dye-filled micro-pipette (Akamatsu et al., 1999; Miyasaka et al., 1999; Rathenberg et al., 2003).

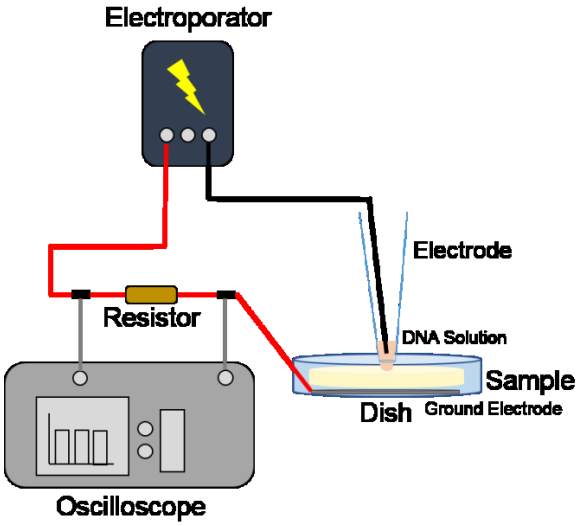


Figure 11 Set up of electroporation conductance trial. Silver wire electrodes were connected to an electroporator, the anode being situated within a glass pipette, directly charging the DNA solution; whilst the cathode is connected to the ground electrode beneath the sample. An oscilloscope measures the voltage drop across a known resistor to monitor amplitude and trains from the stimulus.

Electroporation seemed a useful candidate for transfecting the FRET sensors of choice into OSCs due to the following reasons: (1) the ease of a naked plasmid being ready for insertion, without prior preparation (2) the possibility of pinpointing of a target region of neurons topographically and (3) the possibility of controlling the density of labelling based on DNA concentration and elution volume.

The technical setup for electroporating OSCs is depicted in Figure 11. Initially measurements were taken via oscilloscope to determine preservation of the pulses from an electroporator, via electrode to the ground plate beneath the membrane.

The electrode itself was constructed from pulled silver wire attached to a pipette tip to allow for simultaneously administration of the plasmid and electrical field application. Designs for this tip have been show in Figure 12, with a range of modifications to alter output.

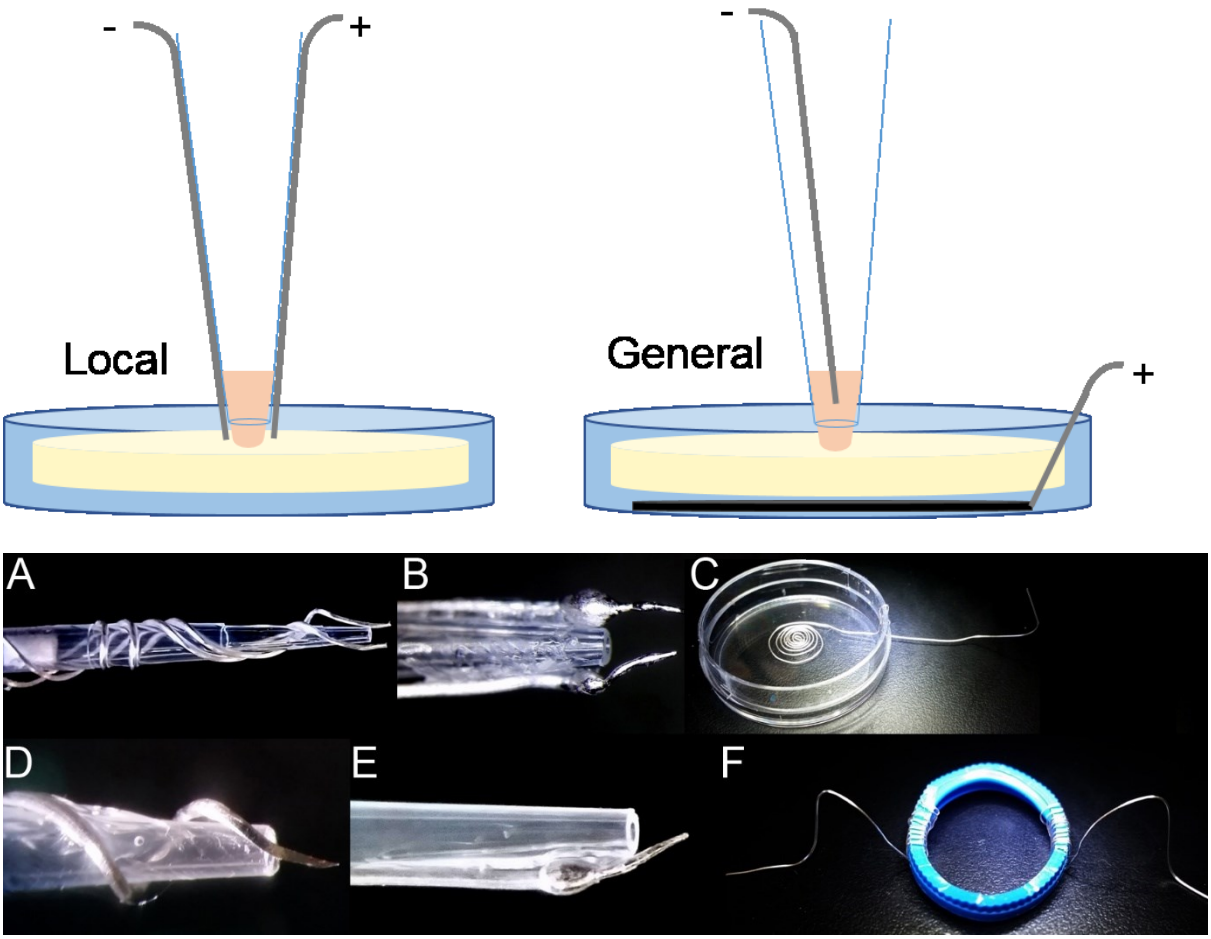


Figure 12 Different versions of electroporator tips for delivery DNA to OSCs. Above: Schematic of electrodes, either localised with both contacts encapsulating the delivery site, or generalised with a ground electrode beneath the sample and the other within the DNA solution itself. Below: Silver wire was glued to 10µl pipette tips for current separation and localised solution delivery. A and B show pole-pole localised current configurations, whilst D and E show single-pole electrodes to be combined with a ground cathode shown in C, placed beneath the sample. F depicts a system for inducing a generalised electrical field across the entire sample.

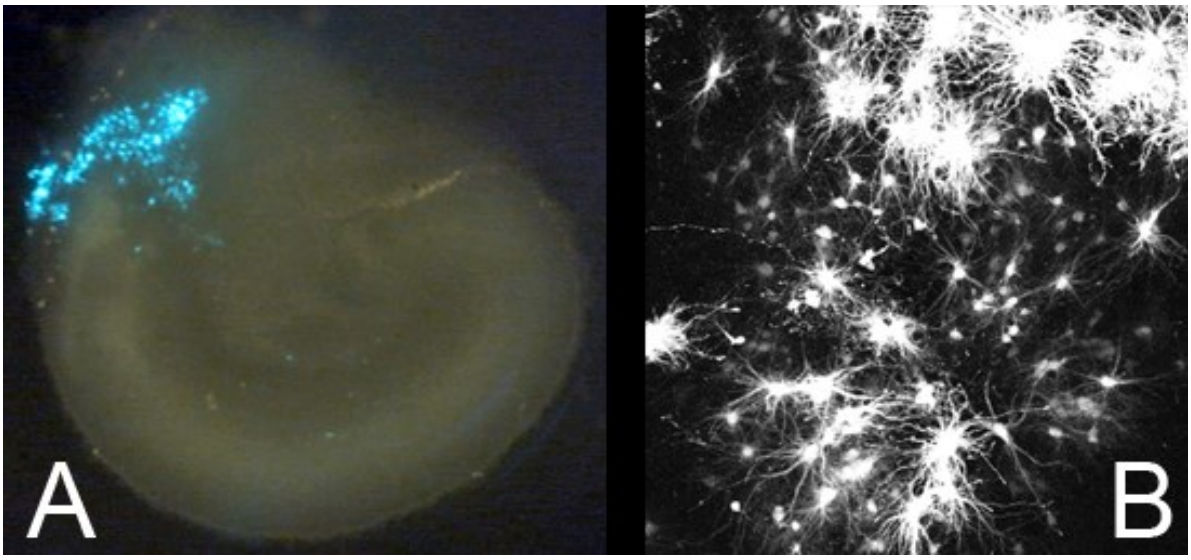


Figure 13 Example of electroporation transfection efficiency. A shows a photograph under dissection scope and fluorescent lamp of the resulting GFP-expressing cells, after electroporation with Tip A from the above figure. B shows the same transfection region under 2-Photon microscopy.

The tips portrayed revolve around single- and dual-pole strategies, either: a single anode is bound to the DNA applicator, negatively charging the plasmid solution and then pulling this, via the sample to a ground electrode; or a 'double pronged' tip simply provides the localised field across the tissue surface, opening the pores for free diffusion of plasmid DNA into the target cells.

The electroporator used was able of producing trains of current at preset voltages and timings, and the literature provided the approximate values to be used, namely: six trains of 50ms duration with 1s interval between each pulse (Murphy and Messer, 2001). For voltage, trials were ran with 12, 25 and 50 volts, whereby the higher the voltage the more cells should transfected, however the more heat damage can be caused to the tissue. These experiments were run with a CMV-GFP plasmid into OSCs 30 days *in vitro*, and were imaged 48 hours later under fluorescent lamp to deduce cell counts.

The results from each electrode are shown in Figure 14, with an example of the localised, high-density transfections reminiscent of the technique portrayed in Figure 13. The data shows that a single-pole electrode produces the highest levels of transfections, with 25V being an ideal voltage compromise for negligible loss of transfection efficiency compared to 50V, yet lower levels of damage to the tissue.

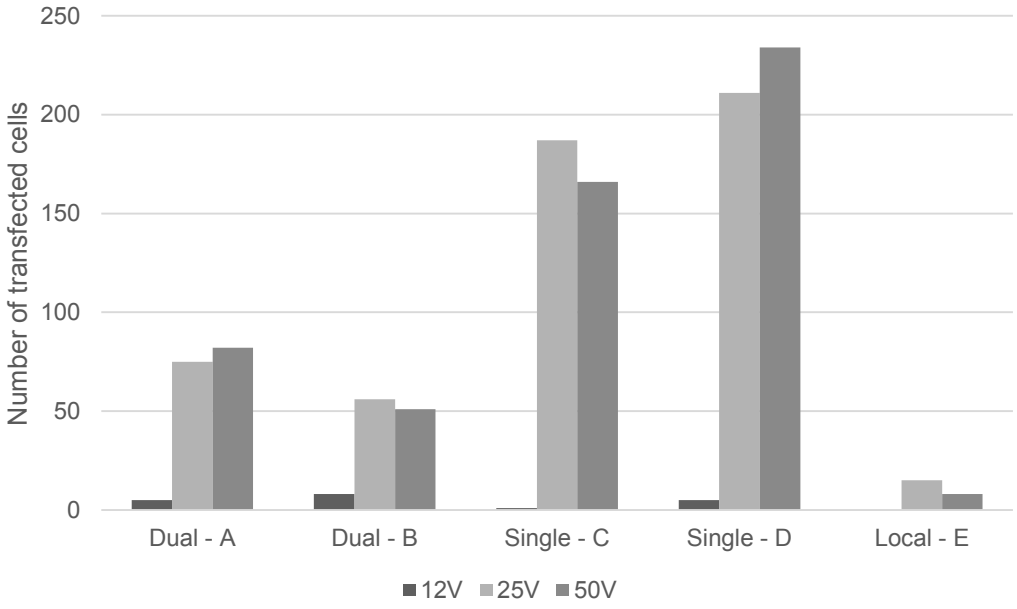


Figure 14 Comparison of electrode tips for transfection efficiency. OSCs were electroporated using one of five different electrode variables. After 48hrs, sections were imaged under fluorescent dissection scope and imaged for quantification analysis of transfected cells (y-axis).

The primary disadvantage of the electroporation system for transfecting FRET sensors into the tissues is the level of damage caused by the electrical field. After 48hrs at the higher voltage, an inflammatory response at the electrode sites can be seen, producing widespread glial up-regulation, making the imaging of healthy neurons unfeasible. A second problem with the technique is the density at which cells are transfected. As the project relies on the imaging of individual axonal processes over time, as well as consequent automated image analysis, dense stacks of processes and overlapping cells becomes an impairment. Finally, while the area can be targeted by the positioning of the electrode, no specification of cell type is

permitted in the transfection technique itself, showing a high number of transfected astrocytes, as seen in Figure 13. A neuron-specific promoter could be used to avoid this problem.

5.2.2 Viral Transduction

Research into viral transduction as a method of introducing DNA of interest into host cells has been driven largely by its application in gene therapy – the delivery of functional genes into patients with defective DNA to correct mutation-driven disease (Friedmann and Roblin, 1972).

The use of viruses to introduce DNA vectors to living cultures has become hugely popular within neurosciences, particularly due to the difficulty of transfecting neurons, a non-dividing cell type, in tissues.

Three viral vectors were trialled to deliver eGFP to OSCs: adenovirus, lentivirus and adeno-associated virus. Table 1 portrays the different properties of each virus.

Virus Type	**Abbreviation**	**Payload Size**	**Targeting Method**
Adenovirus	AV	7.4 (Ehrengruber et al., 1998)	Envelope and/or promoter
Lentivirus	LV	9.0 (Scott et al., 2002)	Envelope and/or promoter
Adeno-associated Virus	AAV	5.0 (Duan et al., 2001)	Serotype selection

Table 1 Comparison of viral vectors for efficiency

As the OSC preparations develop a thick layer of glial cells across the surface, the viral vectors would have to be targeted to prevent mass transfection of non-neuronal cell types. An example of a lack of such targeting can be seen in the case of the adenovirus, whereby a ubiquitous CMV promoter was used, the results of which can be seen in Figure 15-AV.

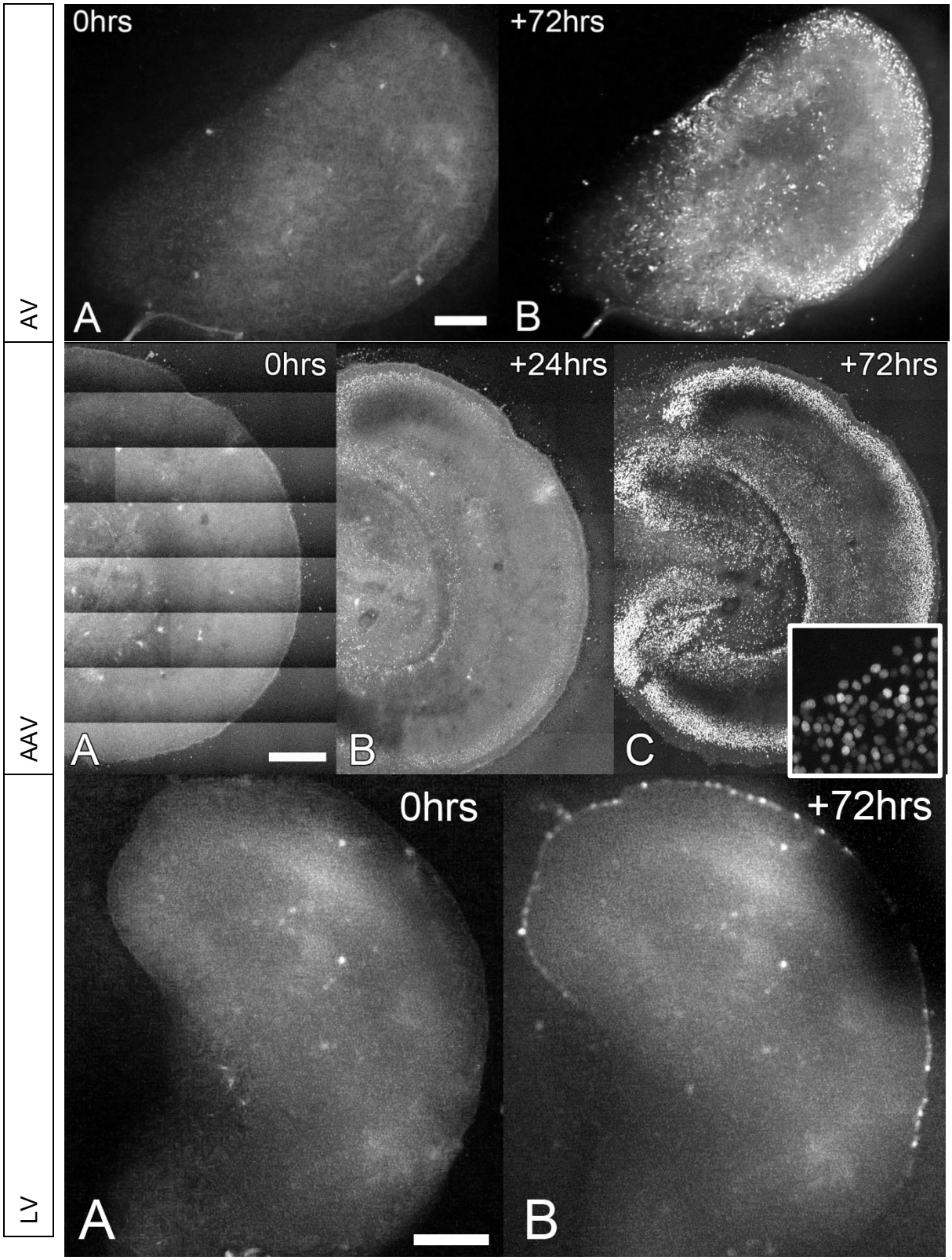


Figure 15 Comparison of viral transductions in OSCs. GFP was transfected via different viruses into OSCs on a 72hr time period. Images were acquired as a tile scan from 2-photon microscopy. Scale bars = 1mm.

In order to target cells of interest, either the genetic payload can be encoded with a neuron-specific promotor, or the envelope of the virus can be altered. In the case of adeno-associated viruses, the serotype has this innate targeting already present, namely the AAV9 serotype (Foust et al., 2009) which is neuron-specific and is also able to cross the blood brain barrier. Figure 15-AAV shows the specific targeting of neuronal cell bodies after 72hrs incubation with the virus added to its media. Lentiviruses (LV) are also capable of being targeted but by changing the tropism of the envelope via pseudotyping to target cell sub-types.

The results of these topical viral applications highlight a valid method of introducing the FRET sensors into OSCs, however the method has several drawbacks.

Firstly, there is a distinct labelling at the outer perimeter of the slice, most likely due to the virus in solution cascading down and off the surface of the tissue and collecting at the base, on top of the membrane or within the media. This results in prolonged contact with viral particles at just these perimeter sites and so labelling does not occur across the more central regions, where the primary neurons of interest, pyramidal subtypes, would be located.

To overcome this, viruses were also injected via microinjection, whereby a pulled glass needle (Figure 16) was used in combination with a micromanipulator and picospritzer pump to deliver the viral solution at specific, localised regions of the cortex. However, this did not produce any significant levels of GFP-labelling, possibility due to the physical trauma incurred or the low concentrations of viral particles capable of being injected.

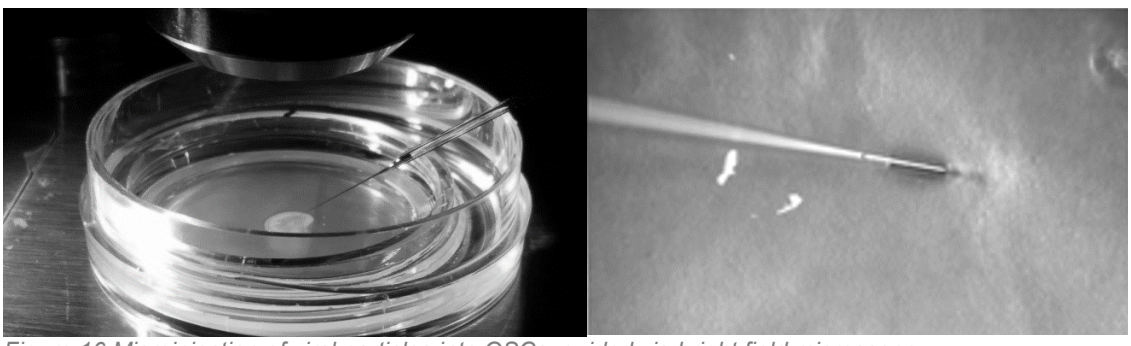


Figure 16 Microinjection of viral particles into OSCs, guided via bright field microscope

The other disadvantage of viral transduction, lies in its inability to seemingly reach the processes of the neurons that fluoresce. As seen particularly in the AAV-infected slices, many neurons are successfully transduced, however only the spherical structures of the somata are seen to express GFP, and not the neuronal processes. This could be due to damage to the cell and as a result, a retraction of its processes; or possibly a transportation/targeting issue on a molecular, cytoplasmic basis. Alternatively, a longer time-scale may have seen eventual movement of fluorescence into the neurites, indeed a time period of 13-15 days has been suggested by Ehrengruber et al. (2001) in the case of AAVs.

5.2.3 Biolistics

5.2.3.1 Introduction to Biolistics

The term 'biolistic' has been coined from the words *bio*logical and bal*listic*, describing the transfection of a DNA construct into a cell via coated, high-speed particles. The technique was initially described for punching through the tough walls of plant cells (Klein et al., 1987), however has since been adapted for the use in mammalian cells.



Figure 17 The BioRad Helios Gene Gun

The principle lies in the DNA coating of microcarriers, typically made of gold or tungsten measuring 0.5-2µm in diameter, which are then accelerated using an inert gas , (helium is ideal due to its low density), into the sample placed a short distance away.

The difficulties in this technique lie in the sum of its many variables, requiring the need for optimisation when transfecting under different conditions.

For this project, the BioRad Helios Gene Gun was used (Figure 17), firing gold carriers powered by helium gas.

5.2.3.2 Determining the Optimal Parameters for Biolistic Transfection into Neurons

The Gene Gun system consists of five variable parameters that can be adjusted to obtain optimal transfection rates, explained in Table 2. These can be divided into those affecting bullet preparation and those of the firing itself. The former consists of gold bead diameter choice and the DNA concentration initially used in coating, whilst the latter comprises gas pressure, firing distance and the addition of diffusers between barrel and sample.

Parameter	Variations	Positive Effects	Negative Effects
Microcarrier Diameter	0.6-1.6μm	Larger bullets penetrate deeper	Larger bullets cause more trauma
DNA Concentration	0-3000 ng/μl	Greater Transfection with higher concentrations	Clumping of bullets at higher concentrations
Gas Pressure	100-500 PSI	High pressures provide greater penetration and spread	High pressures cause more damage to the tissue
Firing Distance	5-30mm	Closer distance provides more penetration	Closer distances result in less spread and more damage
Diffuser Presence and Material	Steel Gauze, Fine or Coarse Mesh	A present diffuser cushions the impact of excess gas against the tissue	Diffusers can decrease velocity and reduce the number of bullets fired

Table 2 Variable parameters to optimise for biolistic transfection.

When preparing the microcarriers, the amount of DNA to be precipitated onto the gold is defined as the DNA loading ratio (DLR) and is calculated from the number of cartridges to be made from the preparation, and the amount of gold loaded into each one. The amount of DNA is a compromise between a high-level of genetic material ideally introduced to as many cells as possible, yet not so much as to cause aggregation of the microcarriers, reducing transfection efficiency.

The diameter of the microcarriers is also an important consideration. Too small and the mass is insufficient to travel through the glial layer that forms across OSCs after preparation; yet too large particles could produce more damage to the neurons labelled. Three sizes (0.6μm, 1.0μm and 1.6μm) of carrier, coated with varying concentrations of eGFP DNA (89-2,127ng/μl) were fired into OSCs and then incubated for 48 hours. Micrographs were then taken of the slices and GFP-expressing cells (see Figure 19 for examples) were quantified computationally. The results, seen in Figure 18, highlight the 1μm diameter microcarriers with

the higher DNA concentrations to be ideal for transfections, and so this system was carried forward in future experiments.

To determine the optimal length of time post-transfection for imaging, slices were shot with GFP with the above parameters and then observed via fluorescence microscopy for 10 days at 24hr intervals. Results are displayed in Figure 20. After the initial 24hrs, the relative intensity of the fluorescent signal increases at a linear rate until peaking at five days (120hrs) post-biolistic transfection, upon which a slow rate of decline was observed.

From these experiments, the gene gun, once optimised, appears to be a very capable and targeting method for transfected OSCs. Its high bullet penetration ability also seems to be able to pass through the glial scarring that occurs on the exposed surfaces of the slice, reaching the neurons within. Minimal damage also occurs, with only the cells being transfected successfully being imaged for over two weeks post-shooting.

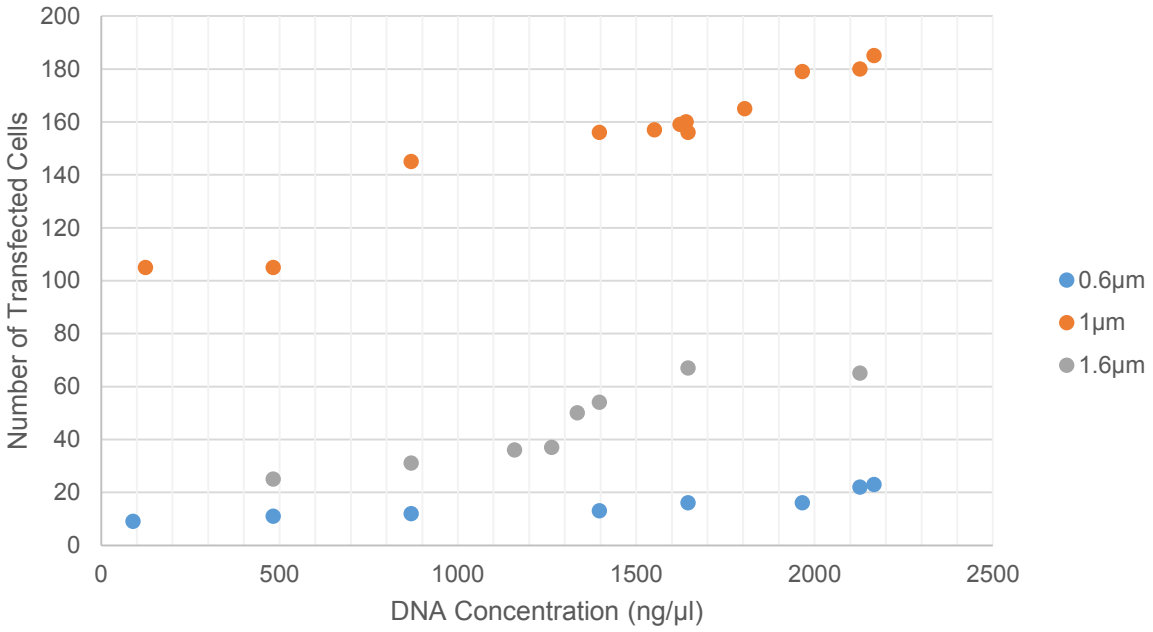


Figure 18 Comparison of Biolistic Parameters. A comparison of DNA concentration and microcarrier diameter on the number of cells transfected in OSCs, as determined by quantification of images taken after five days via fluorescence dissection scope.

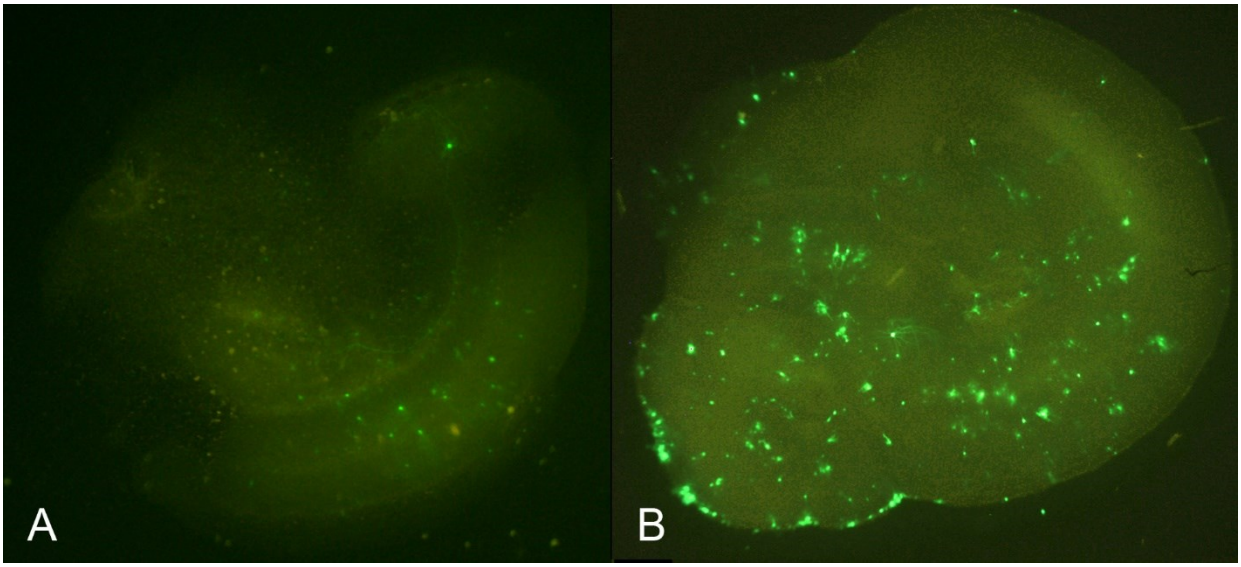


Figure 19 Examples of gene gun parameter differences in relation to transfection efficiency. A shows an OSC after biolistic transfection with 482 ng/µl DNA and 1.5µm carriers, whereas B depicts the same transfection of eGFP with 1966 ng/µl DNA and 1µm carriers.

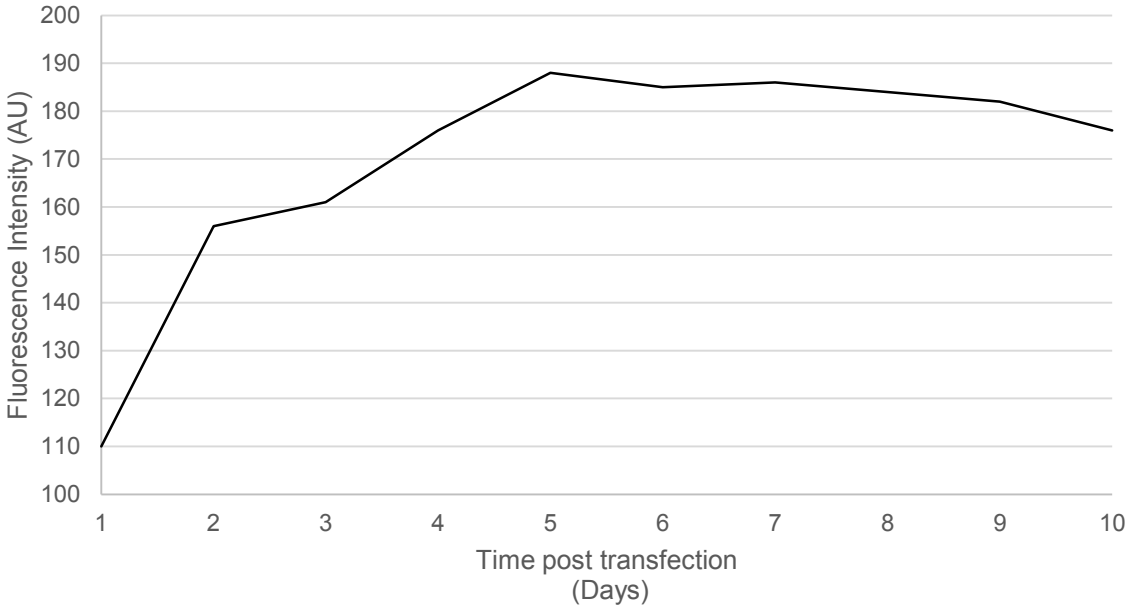


Figure 20 Intensity of GFP measured after biolistic transfection. OSCs were shot with 2127ng/µl DNA on 1µm gold microcarriers and a population of neurons were followed over ten days. The mean intensity in relation to background was quantified and plotted, showing a peak fluorescent intensity at day 5.

5.3 SYSTEMS TO CARRY FORWARD

Transfection Method	**Optimal Settings**	**Advantages**	**Disadvantages**
Electroporation	25V, 100ms Pulse	Targeted and localised, very little preparation	Electrical damage to tissue, dense labelling
Viral Transduction	AAV	High rate of transfection, low levels of reported cell damage	Expensive to produce, no observed neurite labelling
Biolistic Transfection	1µm, 2.2µg/µl DNA	Sparse labelling, fast transfection, reproducible, cost-effective	Ballistic damage, lengthy bullet preparation

Table 3 Comparison of transfection methods for introducing plasmid DNA into OSCs.

From the experiments carried out above, and summarised in Table 3, the transfection method of choice for this project was selected as biolistic transfer. The ease in which the system, once optimised, can be used with bullets made for each FRET sensor and then shot into slices interchangeably and rapidly, along with strong expression just five days later appears ideal for

the use in the project. There is a caveat of ballistic damage to neurons within the OSCs, however when weighed against the advantages and the comparative damage of any transfection technique, it remains most appropriate.

If a more advanced and long-term study was to be attempted in future with a single FRET sensor, more permanent and reproducible options may be utilised, mainly the use of transgenic animals expressing the sensor with a promotor that induces sparse labelling of cortical neurons (e.g. THY-1 as in the GFPm mouse line (Feng et al., 2000)).

Brief screening was performed on an existing mouse line expressing the original, first generation CFP-EPAC-YFP sensor, which is commonly used to monitor cAMP concentrations in cardiac myocytes and other organs within the thorax. However, as the sensor is expressed in every cell within the brain, it is impossible to isolate individual axons for study, let alone the synapses that line them. Sections from one of these transgenic animals is show in Figure 21.

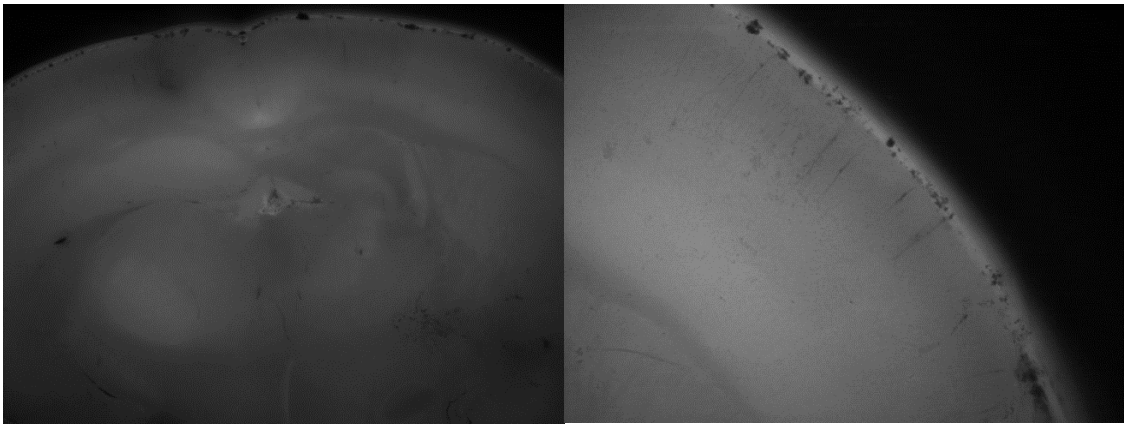


Figure 21 Expression of CFP-Epac-YFP in a transgenic mouse. Wide-field images taken under fluorescent dissection microscope (YFP channel) of slices prepared from a mouse expressing the CFP-Epac-YFP sensor ubiquitously. Fluorescent signal is seen in every cell, making it impossible to isolate individual neurons and their processes.

6 DEVELOPMENT OF A CULTURE IMAGING/MANIPULATING SYSTEM

Culture Type	Microscope	FRET Measure	Transfection
Cell Culture	1P, inverted	Ratiometric FRET	Reagent-based (PEI/Lipofection)
Organotypic Slice Culture	2P, upright	FRET-FLIM	Biolistic

Table 4 Imaging methods selected for different cultures within this project

Table 4 summarises the previous chapter for the optimal methods of acquiring signal from the chosen FRET sensors in both cell monolayers (HEK cell and primary culture studies) and tissues (OSCs).

In order to manipulate the samples to establish a dynamic range for different FRET sensors, a system for simultaneous drug administration and imaging is required. Traditionally, so called 'bath' experiments are used, whereby the drug to be added is simply pipetted topically into the imaging dish and allowed to freely dissociate (Boerner et al., 2011). As I was more interested in specific concentrations of agents, as well as a constant level of saturation, a perfusion system was required for easy exchange of imaging solution. As water-immersible objective lenses were used with both 1P and 2P imaging systems, the samples are permanently submerged in a colourless, ion-balanced imaging solution (see materials for composition). This is the media in which drugs were suspended and administered to samples during imaging.

Several commercial chambers exist for drug administration, however for the specific microscopes being used, the required volume of imaging solution and the size of OSC tissues, a custom system was needed.

In the case of HEK cell studies, an inverted confocal microscope was used to image the cell monolayer that was grown directly onto glass-bottomed petri dishes. Initially, imaging solution was applied from a reservoir gravity fed via tubing and with a tap for flow control, while an aspirator attached to a bent Pasteur pipette removed liquid once it reached a certain height. This preliminary system did allow for media exchange, however was rather cumbersome and resulted in a volume of imaging solution too high to control low doses of drugs being added.

A commercial insert was purchased which allowed for the adherence of a plastic ring to the petri dish via vacuum grease, leaving the glass-bottom portion isolated for filling with and exchanging solution (shown in Figure 22). This was then controlled with a two-channel perfusion pump that could simultaneously administer fresh solution while removing existing liquid at a constant rate.

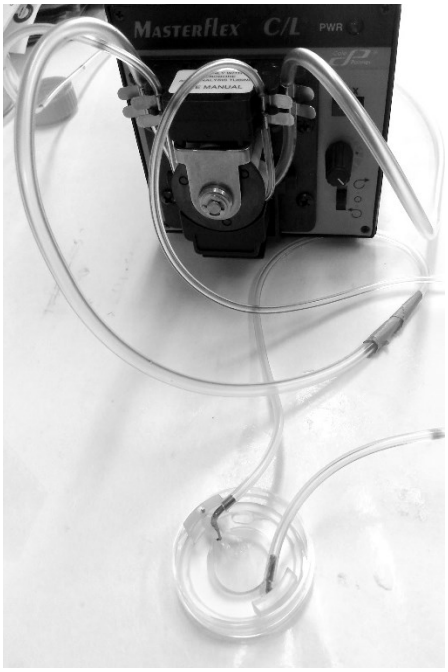


Figure 22 Dish insert and perfusion pump for HEK cell studies.

In the case of the OSCs, the tissues must remain on the membrane they are cultured to in order to stay intact. Therefore, a new option needed to be designed for access from an upright 2-photon microscope with a chamber that could hold the slice and input/output connections for media exchange.

Several 3D printed models were designed and produced to achieve this, the final working version of which is depicted in Figure 23. This insert was then attached to a standard sized glass slide with vacuum grease, thus creating a sealed chamber in the centre for the slice to be placed. In the optimal set up, culture membranes were cut around the tissue, with some excess remaining to then weigh down with a horseshoe-shaped silver bracket, keeping the slice in place during imaging.

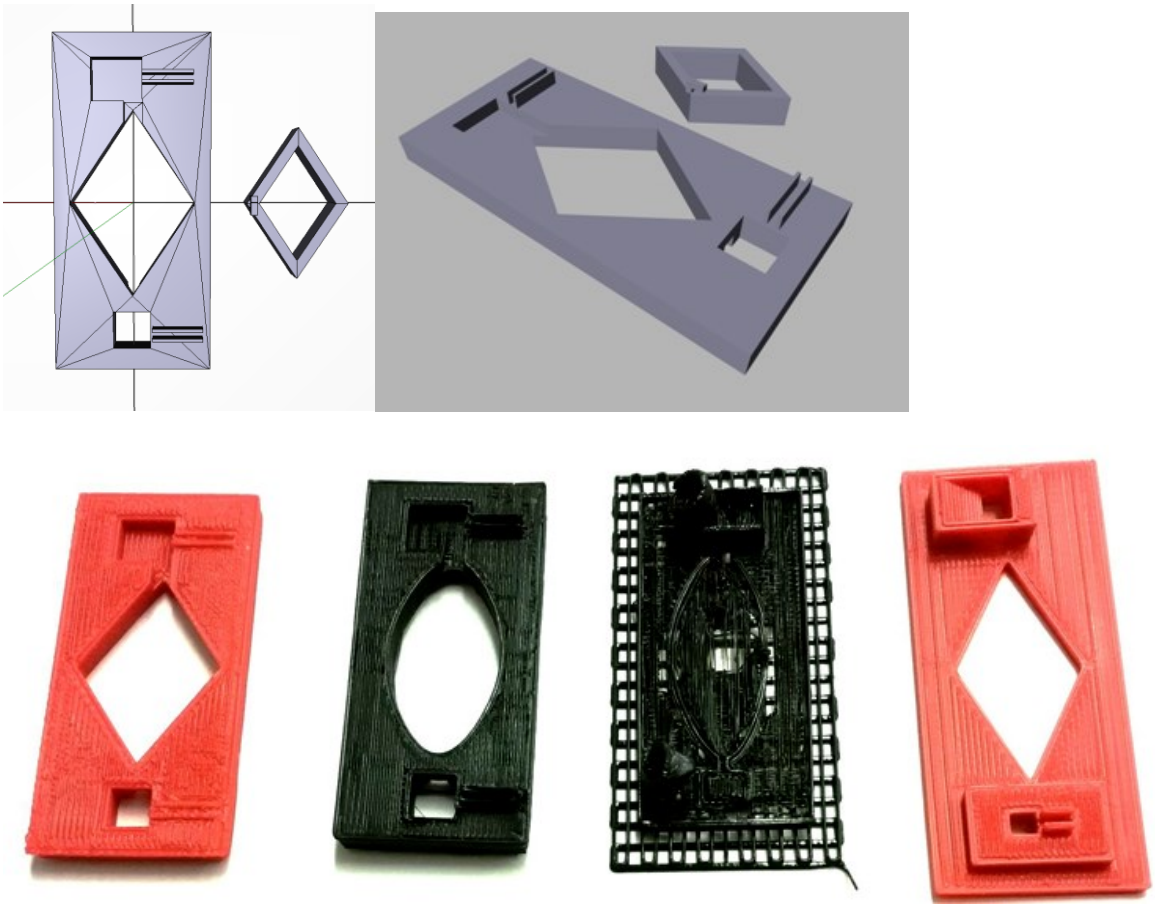


Figure 23 Series of prototype 3D printed perfusion systems. The computer-designed (CAD) version of the final printed model is shown above, while versions printed in ABS (red) and PLA (black) plastics are shown below, with various different shapes and features, from left to right: (1) Initial design with low-profile reservoirs for filling and extracting solution; (2) oval-shaped window for reduction in fluid micro-currents; (3) wireframe model for rapid diffusion of solutions [however there are parts that failed to print successfully]; (4) Raised reservoirs and ramping for addition of solutions with higher extraction pool for a higher meniscus.

One problem found with this system was the non-uniform distribution of media exchange across the imaging area, as assessed with coloured solutions passed through the insert and filmed with a digital camera for analysis (Figure 24). This showed that when a dyed solution is pumped from the insert inlet (at the top, on the figure) and removed from the contralateral side, a relatively uniform distribution occurred after ~20 seconds. However, once an immersible, dipping objective lens enters the imaging chamber, the water tension produced causes micro-currents and disruption to the laminar flow, presenting regions of high and low saturation.

To overcome this, a new method of delivery was developed, whereby a 20G syringe needle was secured to contact the object lens itself, above the meniscus of the imaging chamber. As

the solution is then administered slowly, it travels via adhesion down to the lens itself, entering the column of fluid retention between objective and sample. This causes an instantaneous saturation of the solution at the point of contact which then radiates outwards in a laminar pattern, also removing artefacts of peristaltic pump oscillations. The excess solution is still extracted via the outlet reservoir at the edge of the chamber.

From video analysis of saturation at the points marked by asterisks on Figure 24-B, a comparison was made of the perfusion systems with just the side inlet, the side inlet with the dipping objective present, and with the inlet being fed via the objective itself. This is summarised in Figure 24-E. The stable and equal saturation rates achieved with this latter method makes it the choice method for introducing substances to the sample.

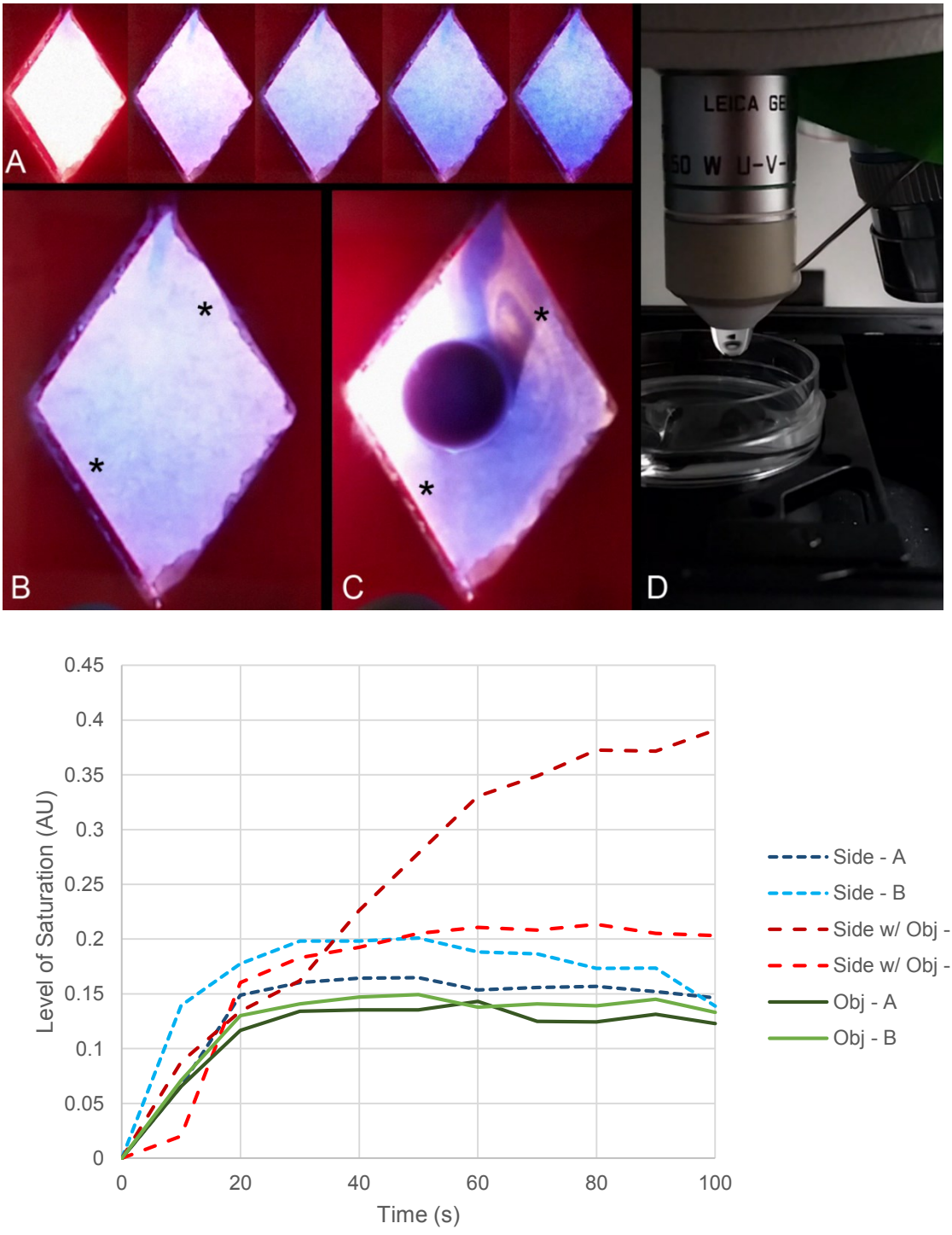


Figure 24 Comparison of perfusion systems based on inlet location. A shows a montage of the insert, mounted onto a glass slide with imaging solution coloured with a blue dye pumped through over two minutes. B and C show a close-up of the imaging area after 30 seconds of perfusion with and without a dipping objective assay present, showing the changes in fluid patterns as the blue dye is pumped in. D shows an alternative method of introducing solutions via the dipping objective itself, removing the artefacts of currents forming from a side-based input. The two points marked with asterisks in B and C were measured for changes in concentration (via colour intensity) over 100 seconds for each arrangement: side-inlet without objective, side-inlet with the dipping objective and objective-inlet alone. The use of this latter system appears to remove artefacts and saturation impairments introduced by the dipping lens.

7 FINDING THE BEST SENSOR

7.1 INTRODUCTION TO cAMP SENSORS

A robust readout of a highly-sensitive FRET sensor would be required to measure the minute changes in cAMP concentrations in different sub-compartments of the neurons being investigated.

As cAMP is so ubiquitous in its functions in many places throughout animal physiology, development of FRET sensors to study its activity has been a popular ongoing process over the last two decades (Boerner et al., 2011).

The first sensor, named 'FlCRhR' after its fluorescein-rhodamine pairing (Adams et al., 1991) utilised a complex construct of two PKA subunits that dissociated upon cAMP binding, thus resulting in a loss of FRET signal. While this led to some striking advances in the understanding of cAMP dynamics, it required direct injection of the fluorophores and so was limited to the large neurons of the sea slug, *Aplysia* (Bacskai et al., 1993). Seven years later, a genetically encoded form was developed, allowing for far greater flexibility in different systems, utilising a more advanced blue fluorescent protein (BFP)-GFP pair (Zaccolo et al., 2000). Since then, CFP-YFP variations have been constructed, bringing higher photostability, and further information of cAMP dynamics (Nikolaev et al., 2004).

After the discovery of Epac in 1998 (de Rooij et al.), this alternative cAMP recipient became incorporated into CFP-Epac-YFP sensors (DiPilato et al., 2004). These Epac-derived sensors saw improved dynamic range (Ponsioen et al., 2004), FRET efficiency, temporal resolution (Nikolaev et al., 2004) and increased signal to noise, mostly due to their simpler, unimolecular and linear arrangement.

With the advantages of Epac sensors, improvements followed in tandem with advances of fluorescent proteins, principally mTurquoise and later mTurquoise2, surpassing CFP with a

doubled quantum efficiency and single-exponential lifetimes (Goedhart et al., 2010), further increasing the signal to noise ratio and photostability (Klarenbeek et al., 2011).

Fluorescent Protein	Excitation (nm)	Emission (nm)	Brightness	QE
eGFP	488	507	33.6	0.60
mCherry	587	610	15.8	0.22
mRFP	555	584	13.0	0.25
mTurquoise	434	474	25.2	0.84
mTurquoise2	434	474	27.9	0.93
mVenus	515	528	52.5	0.57

FRET Pair	FRET Efficiency
GFP-RFP	0.08
GFP-mCherry	0.18
mTurquoise-VenusVenus	0.34
mTurquoise2-VenusVenus	0.40

Table 5 Fluorescent protein and their quantum efficiencies as used within this project. Below, the individual FRET pairs have their FRET efficiencies listed. Taken from http://nic.ucsf.edu/dokuwiki/doku.php?id=fluorescent_proteins.

This project was conducted solely on the use of these newer Epac sensors, principally due to their higher sensitivities: a requirement for detecting the subtle changes in cAMP dynamics in a single neuronal process. As a vast range of sensors are now commonly available from several groups, the choice for this project came down primarily to the combination of different donor-acceptor pairs.

In order for FRET to occur, there must be a substantial overlap of the acceptor emission and donor excitation spectra, and so the overarching colour choices are somewhat predetermined: some variant of blue-yellow or green-red. In the original CFP-Epac-YFP sensors, this overlap allows for a relatively robust signal to be detected, however due to the high level of bleedthrough, the spectra would ideally be more segregated.

Sensor Name	Donor	Acceptor	Reference
$^{T}Epac^{VV}$	mTurquoise	2x Venus	Klarenbeek et al. (2011)
$^{T2}Epac^{VV}$	mTurquoise 2	2x Venus	Klarenbeek et al. (2015)
$^{T2}Epac_{Q270E}{}^{VV}$	mTurquoise 2	2x Venus	Klarenbeek et al. (2015)
$^{GFP}Epac^{RFP}$	GFP	RFP	van der Krogt et al. (2008)
$^{GFP}Epac^{Ch}$	GFP	mCherry	van der Krogt et al. (2008)

Table 6 The FRET sensors used in this project with their respective source papers.

Other considerations in fluorescent protein choice include their proneness to photobleaching, the actual brightness of the expressed fluorophore, the Förster radius, dipole orientation, quantum efficiency, single-exponential lifetime decays and any biological interference with typical cellular function. Of particular concern is the issue of photobleaching when measuring ratiometric FRET recordings (i.e. intensity-based, without FLIM). As the measurement is then a ratio of donor:acceptor fluorescence, bleaching of the donor will create a misleading FRET ratio, whilst acceptor bleaching can do the reverse: counteracting any increases in FRET observed. mVenus consists of an F64L mutation in YFP, accelerating the maturation of the protein and increasing its tolerance to environmental changes including pH and temperature as well as reducing its proneness to photobleaching (Nagai et al., 2002). A direct comparison of HEK cells expressing YFP and mVenus after continuous excitation via confocal imaging is depicted in Figure 25, and displays the resilience of mVenus.

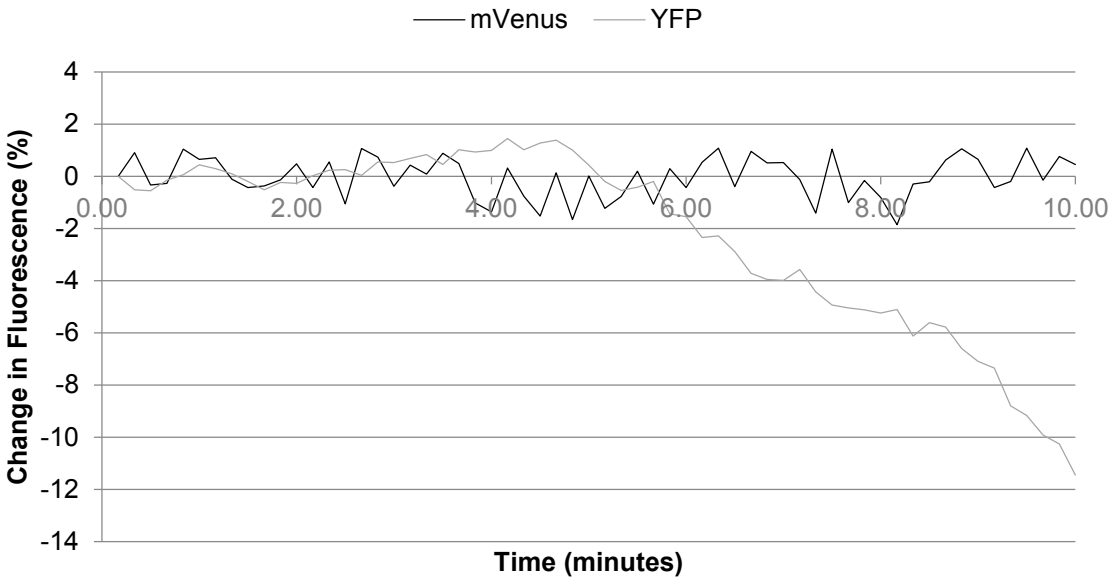


Figure 25 Photobleaching comparison of YFP and its newer variant, mVenus. Plasmids were expressed in HEK293T cells and imaged at fixed laser power and gain for a total of 10 minutes. The change in fluorescence was calculated as the percentage change from baseline recording for each time point (100 / $Intensity_0$ x $Intensity_t$). The YFP signal decreased after 5 minutes, indicated a bleaching of the fluorophore, whilst mVenus maintained a constant level of emission.

All of these factors have led to a shortlisting of five candidate Epac sensors to be trialled (listed in Table 6). First, the 'blue-yellow' variants are listed, starting with mTurquoise and a tandem repeat of mVenus. This doubling up of the acceptor has been found to improve signal to noise ratio (Klarenbeek et al., 2011), due mostly to there simply being more targets for donor-emitted photons. An mTurquoise2 sensor has also been included, as well as a version with a single point mutation, all originating from the Jalink lab at the Netherlands Cancer Institute (NKI) (Klarenbeek et al., 2015; Klarenbeek et al., 2011).

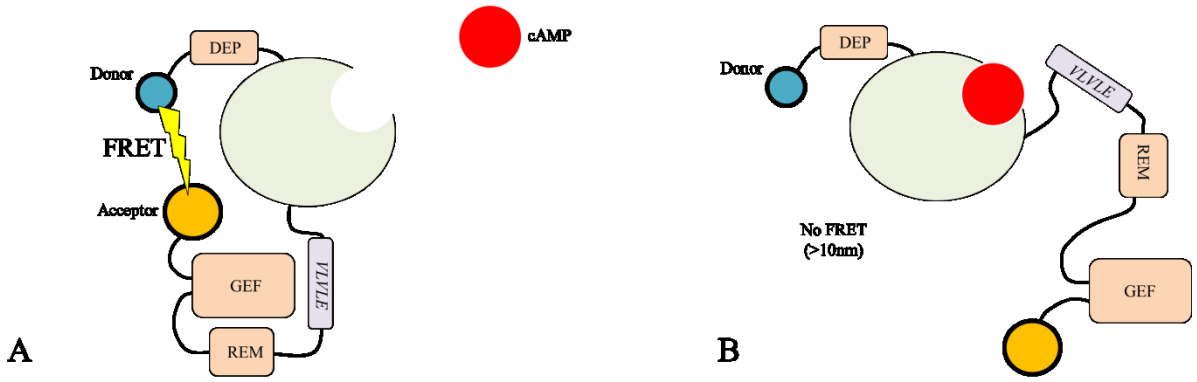


Figure 26 Schematic of Epac sensors **(A)** The resting, auto-inhibited state of the Epac sensor, unbound to cAMP. DEP = Dishevelled, Egl-10, Pleckstrin, REM = Ras exchange Motif, GEF = guanine nucleotide exchange factor, VLVLE = conserved Val-Leu-Val-Leu-Glu sequence. Note that FRET occurs in this state, as the donor and acceptor fluorescent proteins are within 10nm. **(B)** The sensor in its active form with cAMP bound. Due to the fluorophores now being further apart, no FRET signal is recorded. Adapted from Ponsioen et al. (2004).

Also from the NKI, are two green-red sensors, of particular interest to the project due to the nature of imaging live structures with multiphoton imaging systems (van der Krogt et al., 2008). The shift into the higher wavelengths not only allows imaging with lower laser power to prevent unnecessary damage and bleaching, but also minimises detection of alternative sources of fluorescence lifetime in the tissue, for example, autofluorescence, at the lower end of the spectrum.

All of these sensors have an adapted Epac linker region, transforming it from the endogenous Rap1 guanine-nucleotide-exchange factor to a highly efficient 'collector' of cAMP molecules. First, the membrane-associating DEP domain has been deleted, preventing the sensor from localising to the cell membrane (Qiao et al., 2002). This not only renders the sensors cytosolic (hugely increasing signal), but also impairs Epac's function in activating Rap1. Combined with further mutations (T781A and F782A), Ponsioen et al. (2004) found the sensors to be "catalytically dead", with no Rap1 activation. Second, in their final rendition of the sensor, $^{T2}Epac_{Q270E}^{VV}$, the Jalink lab added the single glutamine to glutamic acid mutation at position 270, portraying an apparent 2.5x increase in Epac affinity for cAMP. This discovery was first made by Rehmann et al. (2003) who identified that all other cAMP-binding domains consisted the presence of a glutamic acid residue, yet in the case of Epac, this was replaced for glutamine. Switching it drastically increased the affinity (AC_{50}) of the binding site for a cAMP

analogue (Dao et al., 2006). A schematic for the mechanism of conformational change in these FRET sensors is shown in Figure 26. Also note that this system of FRET response is somewhat 'inverted' whereby FRET occurs when the sensor is in its inactive, unbound state and then ceases upon cAMP binding. This is beneficial due to a) the confirmation that the sensor is expressing and behaving correctly prior to stimulation and b) a somewhat improved signal to noise ratio from the detection of a loss in signal rather than a net gain.

To determine the most sensitive and best-suited sensors to be carried forward with this project, the candidates were tested in preliminary trials in the different culture mediums highlighted in chapter 5. As the ultimate goal of the project was to record from deep neurons in tissue, both FRET and FRET-FLIM trials were carried out to ensure the greatest sensitivity and dynamic range for each sensor.

7.2 Analysis of Dynamic Range

A key indicator for the FRET sensor that will allow for the most accurate readout of cAMP is its dynamic range: i.e. the dynamic range of sensitivity from a baseline level to a saturated concentration of cAMP in the cell of interest.

In order to achieve this maximum value, the cell can be stimulated pharmacologically, in the case of this project, with forskolin. This plant-derivative is an adenylate cyclase activator, which therefore upregulates production of cAMP in most cell types and is used universally to raise its levels reliably (Seamon and Daly, 1981).

For establishing dynamic range, samples were transfected with candidate sensors and then stimulated while being observed for changes in FRET readout. Samples with the strongest responses to stimulation with forskolin would be taken forward to imaging in OSCs under 2P-FRET-FLIM.

7.3 HEK CELL STUDIES

For ease and efficiency of an initial screening phase, HEK293T cells were used as a readily available, easily cultured and well-characterised cell line to test sensors.

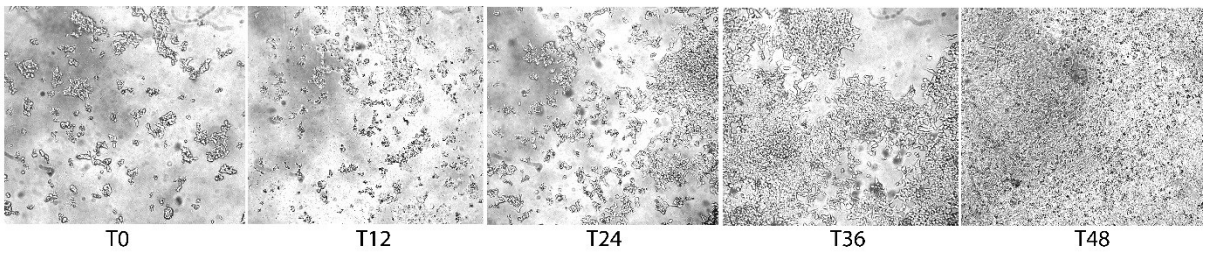


Figure 27 Images taken via bright field microscopy of HEK293T cells at 12 hour intervals after seeding.

In order to establish cAMP changes were indeed being manipulated as to be expected with the appropriate pharmaceutical agents, a cell assay was carried out for cAMP, producing a change in light absorbance based on its absolute concentration. Adenylate cyclase modulators were added to cells immediately prior to the screening to observe changes in intracellular levels of cAMP, as depicted in Figure 28. 3-isobutyl-1-methylxanthine (IBMX), a phosphodiesterase inhibitor, prevents the degradation of cAMP from enzymatic activity, whilst N-(cis-2-phenyl-cyclopentyl) azacyclotridecan-2-imine-hydrochloride (MDL-12330A) has been shown to inhibit adenylate cyclase activity, thus essentially blocking the effects of forskolin, as demonstrated in the findings. IBMX also shows an increased effect of forskolin, however is more effective in prolonging raised intracellular cAMP concentrations rather than immediate increase.

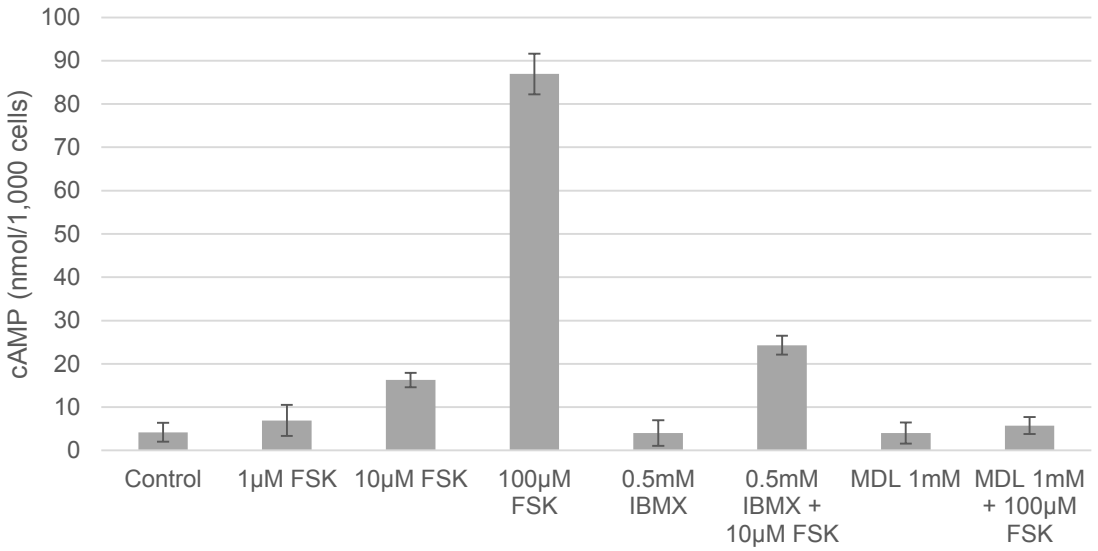


Figure 28 cAMP concentrations in HEK293T cells after drug addition. Cells were grown in 96-well plates and then treated with each drug for five minutes before being lysed. An ELISA with PKA conjugated to HRP was performed on each set of cells in triplet repeats and analysed via photospectrometer, excitating at 405nm.

7.3.1 HEK FRET

As the cells were grown as monolayers directly onto coverslips in culture, an inverted confocal microscope was ideal for imaging, measuring the direct FRET ratiometric values at each time point, before and after forskolin addition.

First, to obtain the reference values for the emission spectra of the sensors being expressed, an *xyλ* scan was recorded, whereby the PMTs scan through a pre-determined range of wavelengths and record intensity. This is shown in Figure 29, a combined plot of the donor, acceptor and complete sensor screened in separately expressing cells. This allows for the precise tuning of the microscope detectors to acquire donor and acceptor signals, with minimal spectral bleedthrough. PMTs were tuned to 455-465nm for mTurquoise acquisition, and 535-545nm for Venus recordings, catching the peak emission wavelengths and avoiding spectral crosstalk.

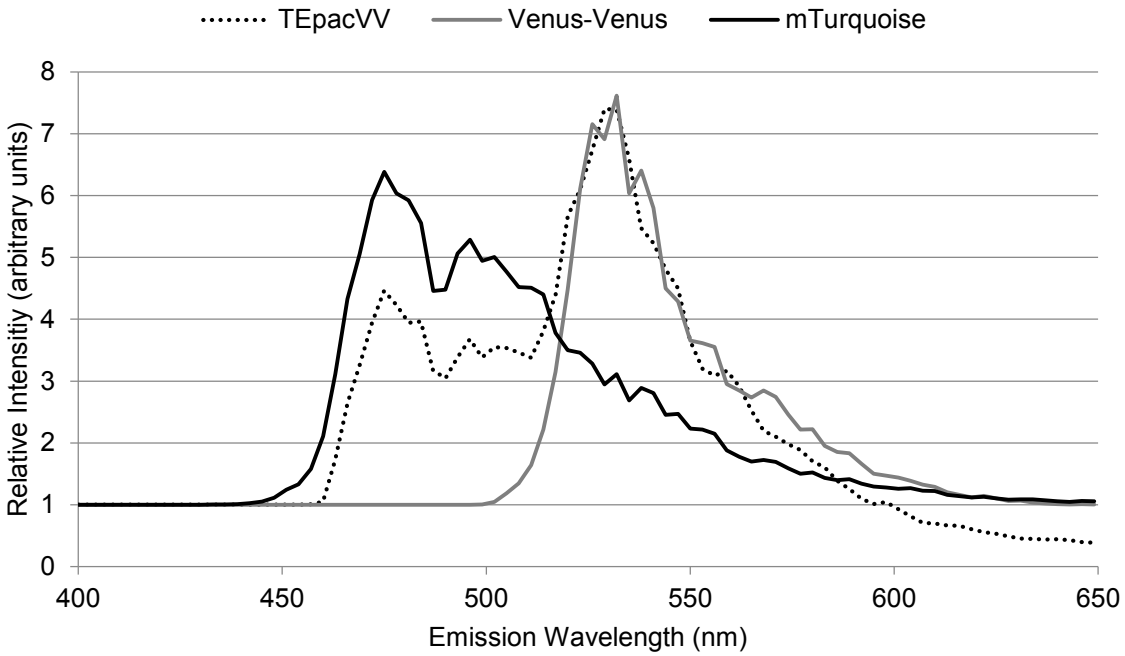


Figure 29 Fluorescent Spectra of an mTurquoise-Epac-VenusVenus FRET Sensor XYλ scans were acquired using confocal microscopy with a spectral detector, imaging HEK293T cells expressing the mTurquoise donor plasmid alone, the VenusVenus tandem repeated acceptor alone and the fully expressed sensor. The spectral overlap exhibited portrays the necessary spectral criteria for FRET to occur. Each fluorophore was excited with the appropriate laser line (474nm for mTurquoise and 514nm for VenusVenus).

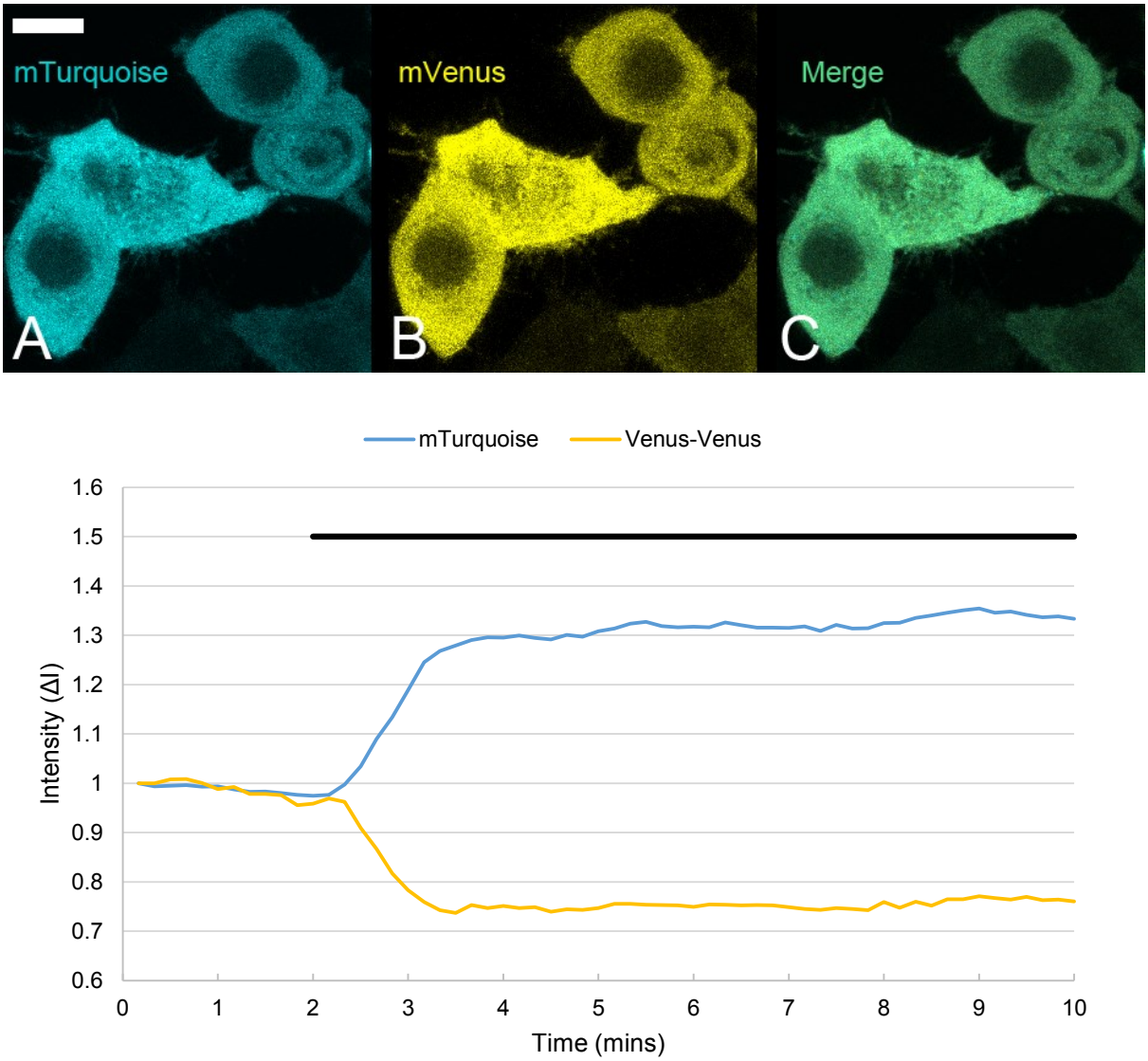


Figure 30 Example of HEK293T cells expressing $^{T}Epac^{VV}$ sensor. A shows only the mTurquoise channel, B the mVenus, and C a merge of both. Images were taken with confocal microscopy. Scale bar = 10µm. The graph below shows the blue and yellow channels that were being recorded during acquisition. Upon addition of 100µM forskolin (black bar), the mTurquoise intensity increases as the Venus channel decreases, indicating a loss of FRET activity.

Cells were seeded at a low enough density that individual samples could be isolated during imaging. Utilising the insert specified in Chapter 6, Figure 22, solutions of forskolin could be passed over the adherent cells during imaging at a pre-defined time point. Figure 30 depicts the cytoplasmic expression of the $^{T}Epac^{VV}$ sensor in HEK cells with each individual channel simultaneously recorded; the ratio of which provides the FRET measurement. Note that the sensors being used experience FRET at their resting, unbound state and so the yellow channel is essentially at its maximum intensity prior to the addition of forskolin. Upon activation

via cAMP binding (induced by the addition of forskolin), the sensor undergoes a conformational change, moving the donor and acceptor apart until there is no longer excitation of the latter, resulting in a brighter signal from the donor and a loss in intensity from the acceptor.

To determine the most sensitive sensor, imaging consisted of the expression of each sensor in different HEK cell preparations and recording intensities of both donor and acceptor channels over a period of ten minutes, with the addition of 100μM forskolin at 120 seconds. Images were acquired every ten seconds, a compromise of time resolution and reduction of photobleaching. A typical FRET response is displayed in Figure 31, with a colourmap representative of the ratio of donor:acceptor changing over time.

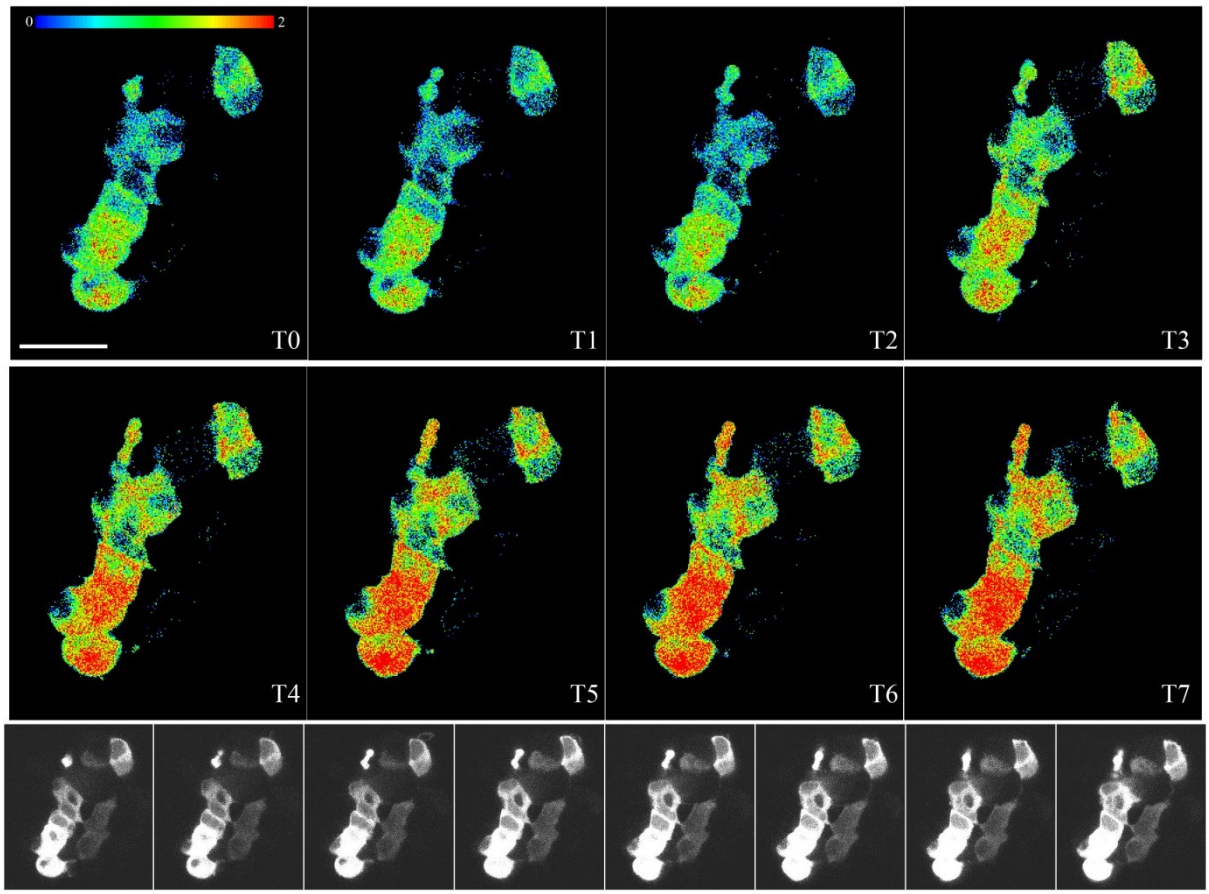


Figure 31 FRET Montage of mT2-Q270E-VV Sensor in HEK293T cells Blue and yellow channels were recorded from the donor/FRET signal and a ratiometric channel was generated. Time is in minutes, with forskolin added at 2:00. The colour shift from green to red signifies the change in FRET ratio. Cells were excited at 474nm, scale bar = 100μm. The raw donor channel is shown below to illustrate cell morphology over the same time scale.

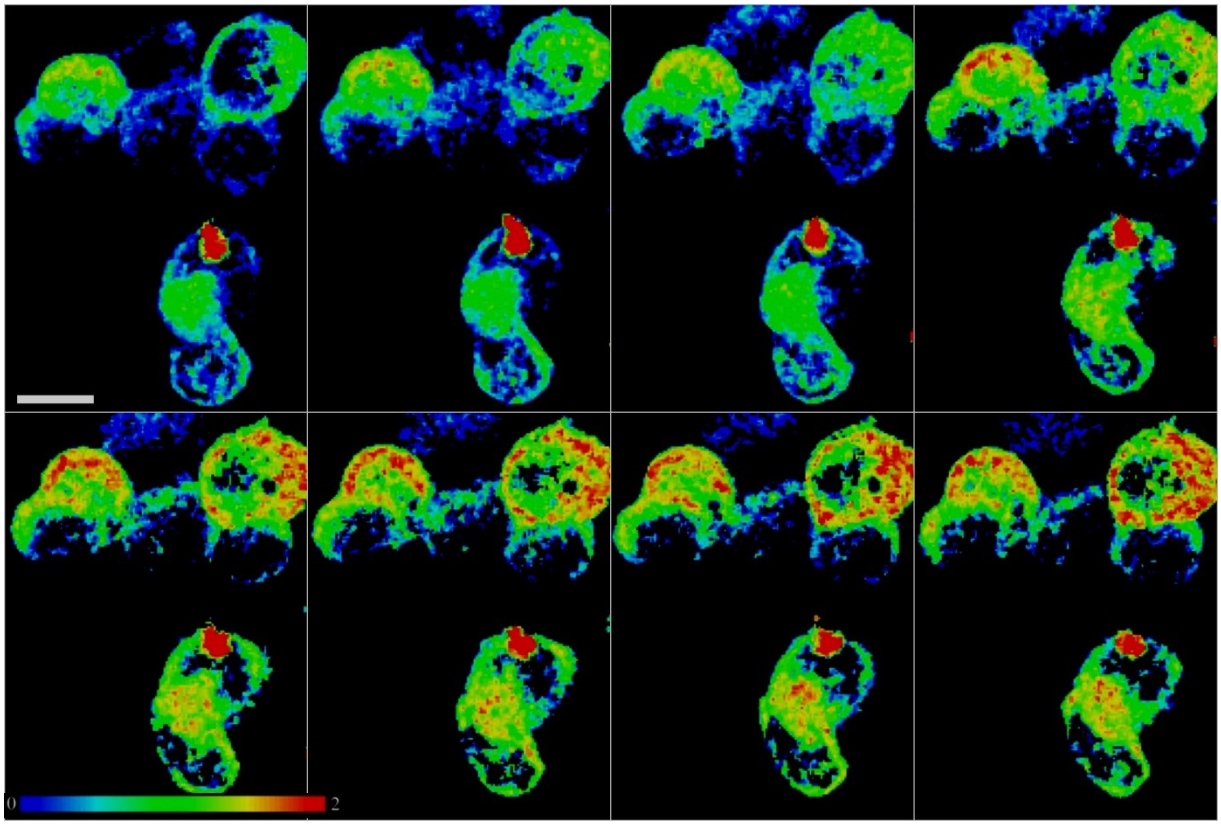


Figure 32 FRET Montage of GFP-mCherry Sensor in HEK293T Cells Green and red channels were recorded from the donor/FRET signal and a ratiometric channel was generated. Time series is as in the previous figure, with forskolin added at 2:00. Cells were excited at 488nm, scale bar = 80μm.

Each sensor was screened in the above manner to obtain a maximal response, producing the graphs in Figure 33.

From this data, two distinct groups arise, defined by the donor fluorescent protein: GFP or mTurquoise variants. The GFP constructs, GFP-mCherry and GFP-RFP, approximately produce a 50% FRET response, when compared to the 80-100% changes seen from the mTurquoise sensor responses. The sensor with greatest sensitivity was confirmed to be $^{T2}Epac_{Q270E}^{VV}$, in accordance with the literature from its creator (Klarenbeek et al., 2011), with a FRET percentage change from baseline of 102%.

From this data, the highly sensitive $^{T2}Epac_{Q270E}^{VV}$ was carried forward to the next series of experiments as the prime candidate for measuring synaptic changes. However, due to the nature of multiphoton imaging in a medium prone to light scattering (i.e. OSCs), the best performing GFP sensor, GFP-mCherry, was also taken forward. The higher shifted spectra of

GFP-mCherry reduces the amount of scattering and absorption in deep tissues, producing a higher signal:noise ratio.

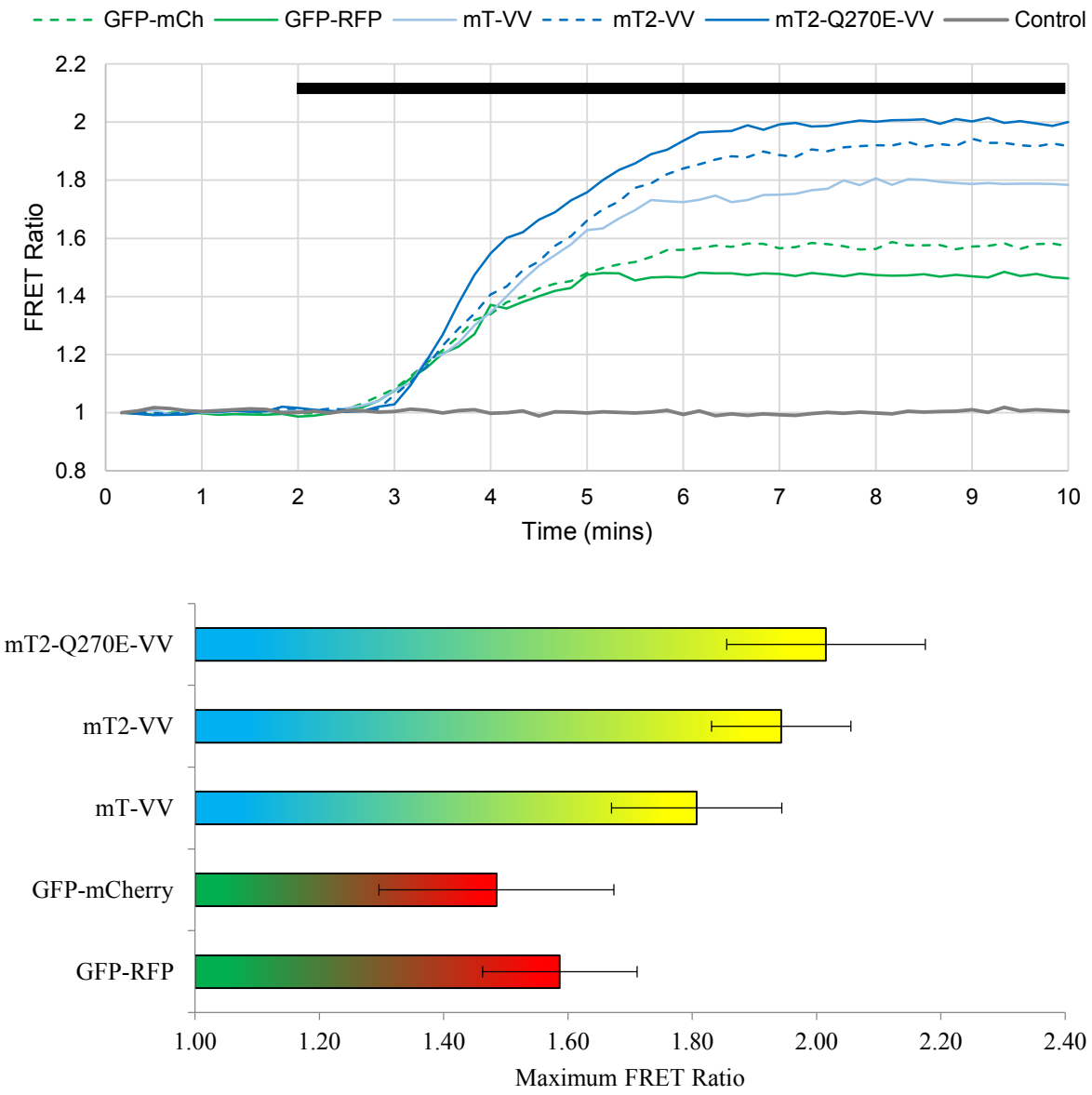


Figure 33 Comparison of Epac Sensors from the NKI Forskolin was administered at two minutes across all experiments (black bar) using HEK293T cells. The control is averaged across all sensors using a DMSO vehicle instead of forskolin. *45-60 cells were sampled across five preparations of cells for each sensor*.

7.3.2 HEK FLIM

The sensors from the ratiometric FRET experiments were then screened using a FLIM system. Initially, FLIM recordings were carried out on a 96-well plate reader system, custom built by the Photonics group at the Imperial College London physics department. The system is unlike

the other microscopes used in the project, as it uses a continuous, filtered white light source to illuminate the samples, in tandem with a CCD and spinning disk to acquire images; as opposed to the laser-derived confocal and multiphoton microscopy arrangments. This also meant that unlike the previous trials involving a perfusion system for drug exchange, solutions were pipetted directly into the well during imaging, producing a small 'dipping' artefact that can be seen as a slight deviation from the response in the results shown in Figure 34.

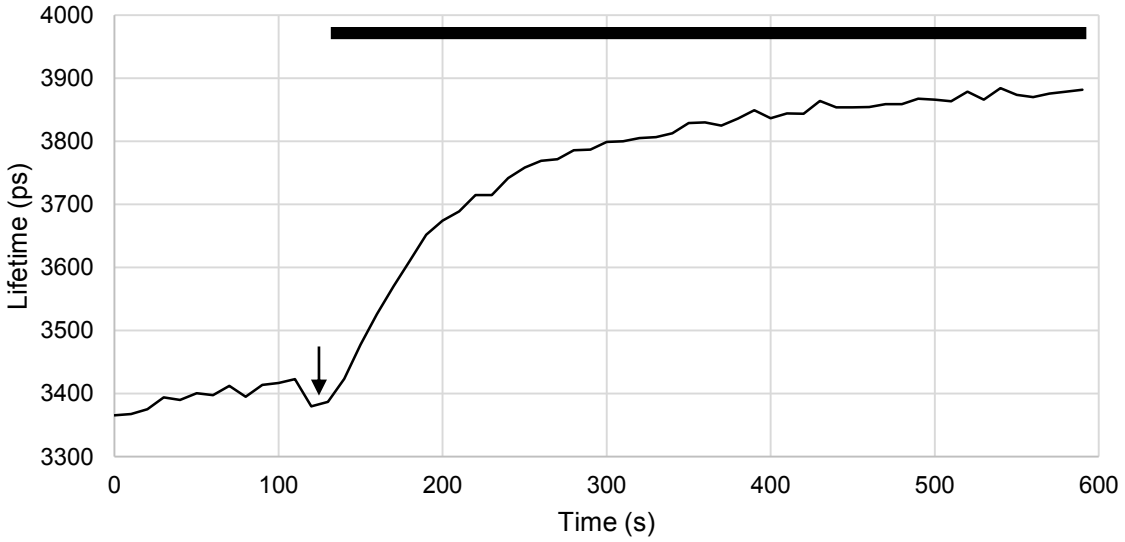


Figure 34 FRET-FLIM response of Sensors in HEK cells acquired on a plate-reader. 100μM forskolin was added at 120s (black bar). A small 'dip' is seen to offset the baseline immediately prior to stimulation (arrow) due to the direct pipetting of the drug into the well in which HEK cells were plated. T2-Epac-Q270E-VV sensor used.

The response is somewhat delayed after forskolin addition, with a more shallow increase in response taking >400 seconds to reach its maximum. This is most likely a response to the 'bath' method of drug application, resulting in improperly diffused drug molecules throughout the imaging well.

While this plate reader system is semi-automated and allows for fast acquisition of multiple samples, an adapted confocal system was also used to acquire preliminary FRET-FLIM data in these cells. Figure 35 displays the lifetime decay traces from a laser-based system, consisting of a confocal microscope with an attached FLIM detector and TCSPC system for

photon counting. This approach allows for more photons to be collected over a longer integration time, proving a comprehensive set of points to fit the lifetime decay. Note the lengthening of lifetime (right-shifted curve) upon administration of forskolin, caused by the loss of FRET as the sensor changes in response to increased cAMP production.

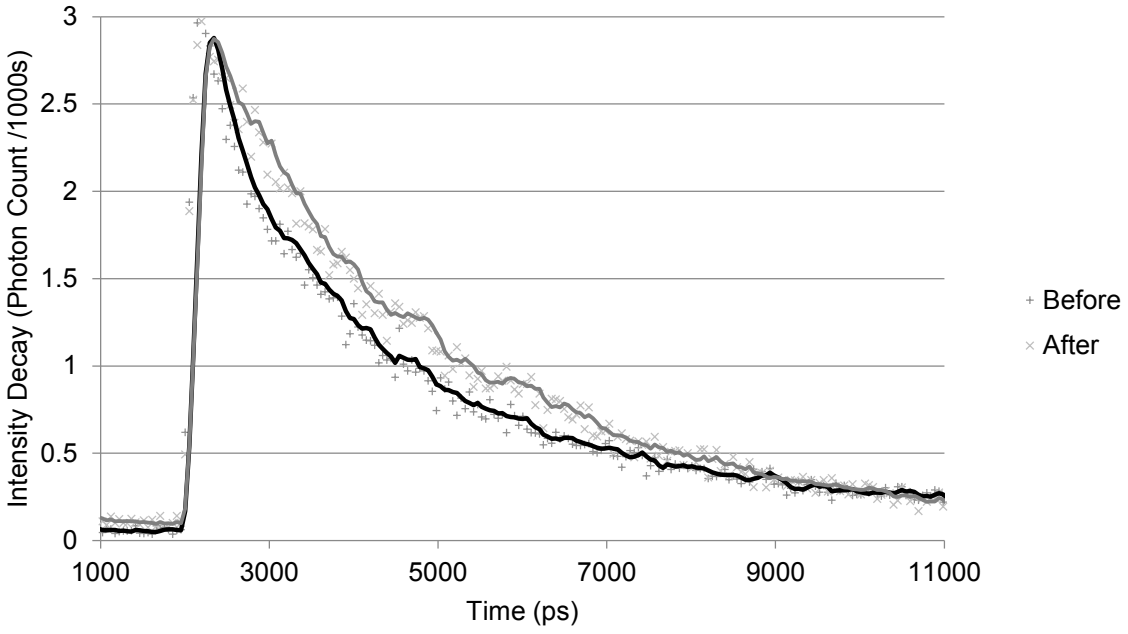
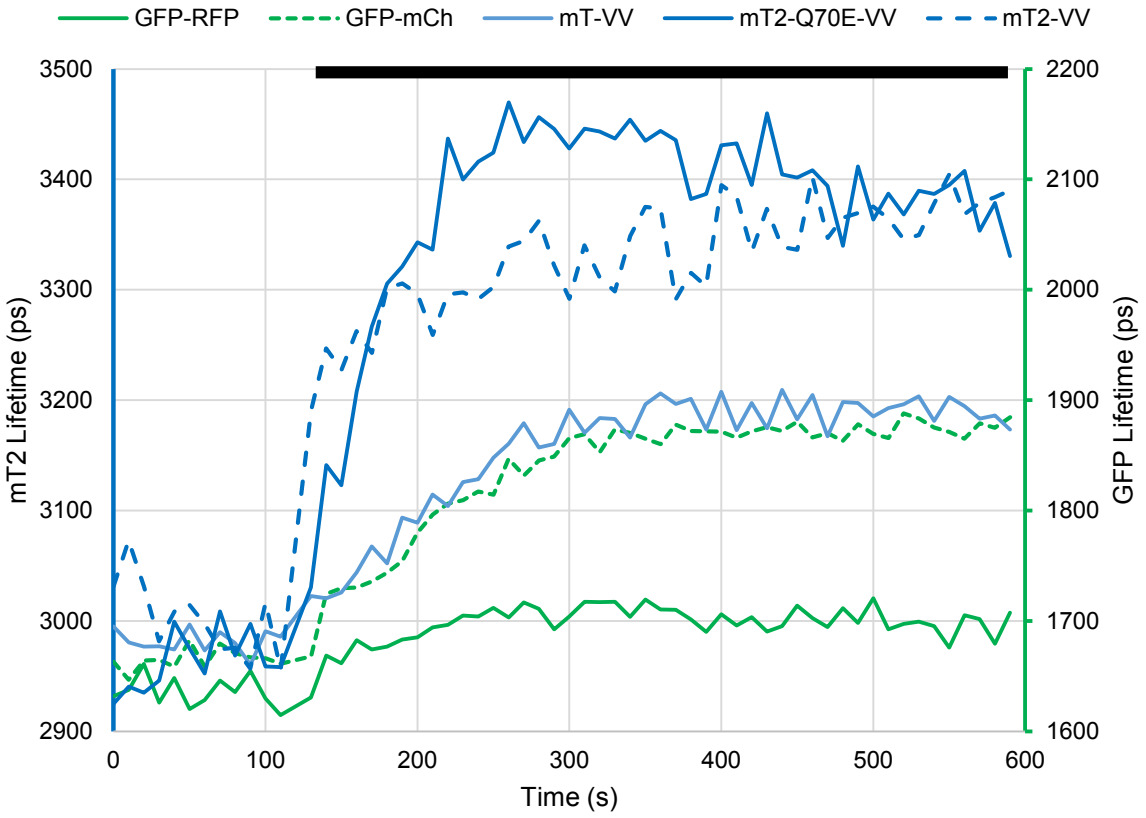
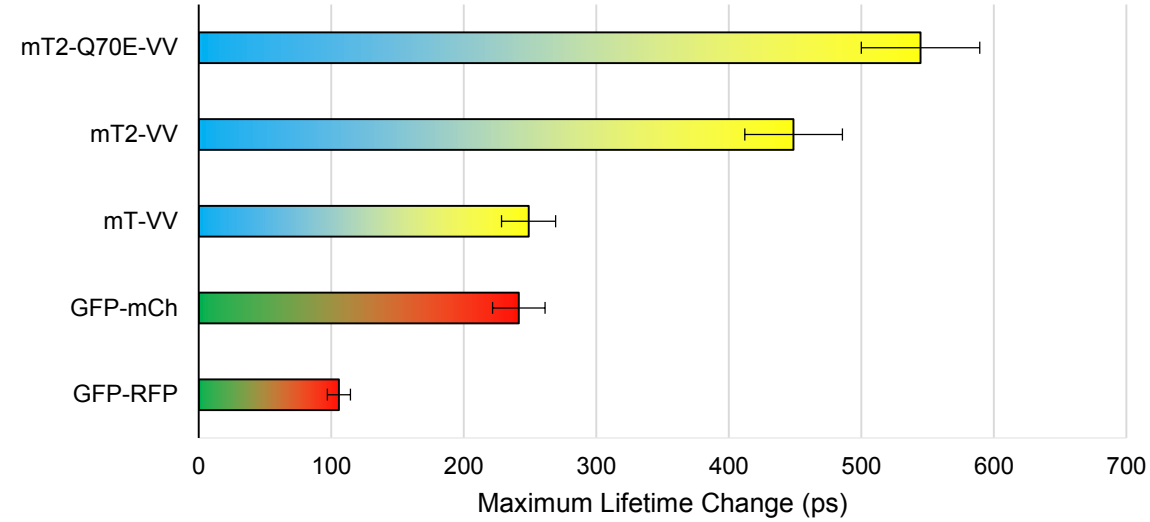


Figure 35 Lifetime Decay of FRET sensor in HEK cells. Lifetime decay with FRET changes in HEKs. Time correlated photon arrival times plotted to produce a decay curve of fluorescence lifetime in the mT2-EPAC-Q270E-VV sensor, before (black) and after (grey) 100μM forskolin addition. Images were acquired on an SP5 confocal system with a TCSPC system for FLIM.

All five sensors were also screened using this system, the results of which are shown in Figure 36. Unlike the separation of the donor-based sensors seen in the FRET experiments (Figure 33), there is more of an overlap in these FRET-FLIM recordings. However, the strongest responses were also seen in the same two sensors in each category: $^{T2}Epac_{Q270E}^{VV}$ (545ps) and GFP-mCherry (241ps).

From these initial HEK cell experiments, these two sensors were then moved into primary neuron cultures, to test their appropriate responses in a neural environment, whereby cAMP production and activity is altered in the physiology of a different cell type.


GFP-RFP
GFP-mCh
mT-VV
mT2-Q70E-VV
mT2-VV
mT2 Lifetime (ps)
GFP Lifetime (ps)
Time (s)
3500
3400
3300
3200
3100
3000
2900
2200
2100
2000
1900
1800
1700
1600
0
100
200
300
400
500
600



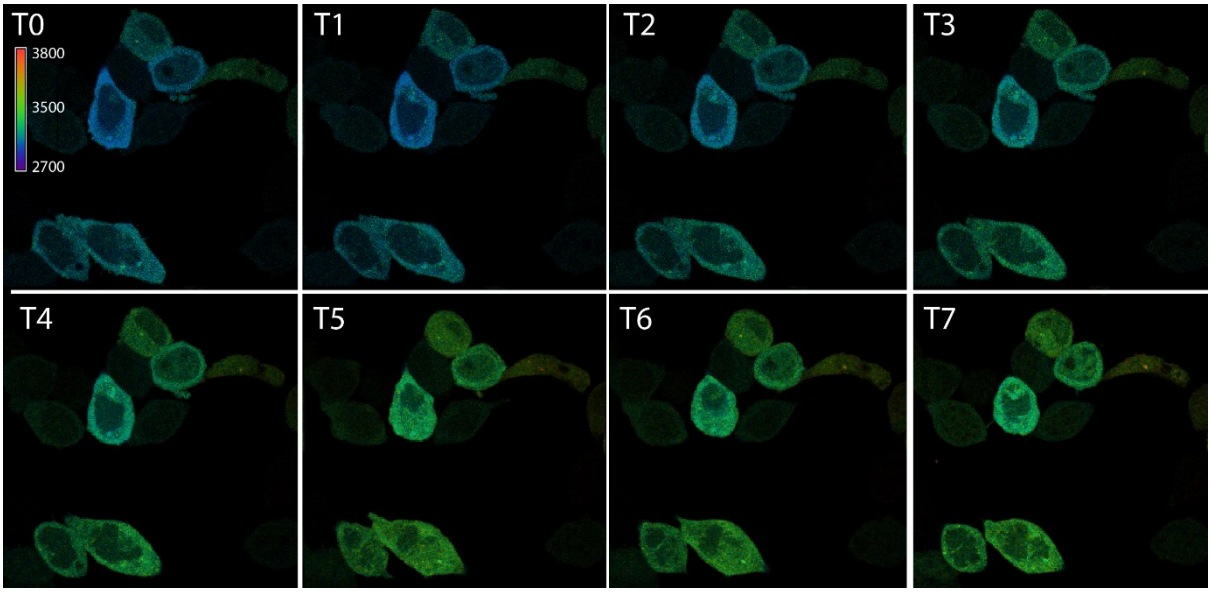


Figure 36 FRET-FLIM screening of sensors in HEK cells with confocal microscopy. Cells were imaged on a confocal system with a TCSPC card for photon counting. Forskolin was administered via perfusion pump at 120 seconds (black bar in top graph). The lifetime scales have been separated due to the different donor baselines. The graph below shows the maximum lifetime changes for each sensor generated from the graph above (n=3). The bottom figure depicts example images for the mT2-Q270E-VV response, showing the first seven minutes with forskolin added after two minutes.

7.4 PRIMARY NEURON STUDIES

As an intermediate stage from HEK cells to OSCs, primary neuron cultures were isolated from embryonic mice and grown *in vitro*. This provides the advantage of a single cell monolayer, ideal for confocal imaging, with some insight into neuronal morphology and expression patterns.

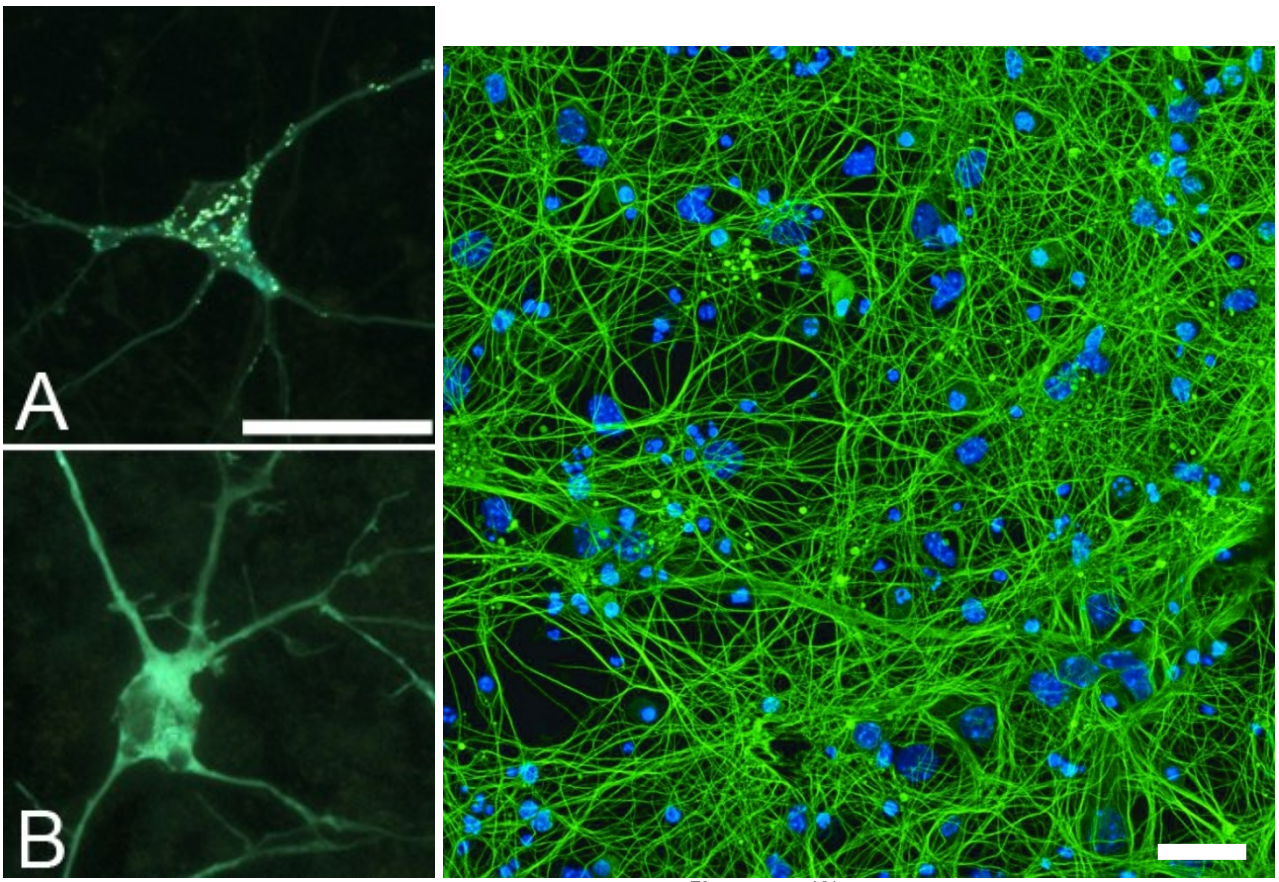


Figure 37 Primary neuron cultures in vitro. Left, Expression of the $^{T2}Epac_{Q270E}^{VV}$ sensor in PNCs: A shows the aggregation that can occur with higher concentrations of protein expression, while B shows the absence of such clusters with a reduction of DNA concentration (2µg/µl for A reduced to 1.5µg/µl for B). Right, a double staining with DAPI (blue) and phalloidin (green), showing the nuclei and actin respectively, of the processes and a formation of a monolayered neuronal network in vitro. Both images acquired via confocal microscope. Scale bar = 50µm.

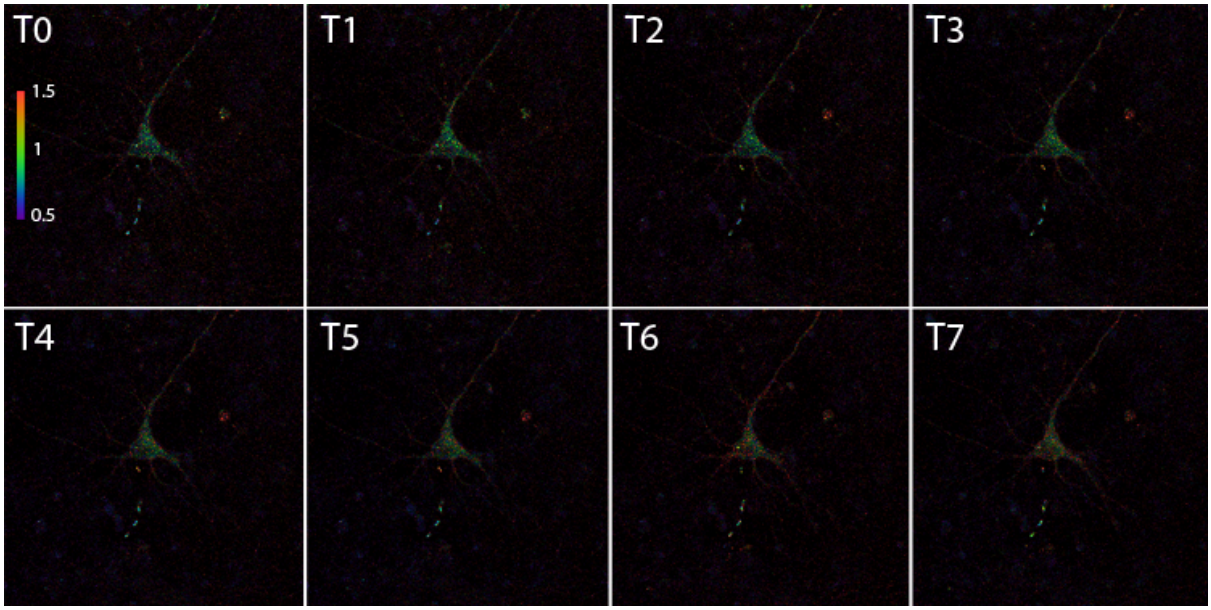
7.4.1 PNC FRET

Expression levels of sensors were typically lower in PNCs than in HEK cells, as were the number of healthy transfected cells. This is due to the transfection of neurons *in vitro* being substantially more difficult than in HEK cells, attributed mainly to their sensitivity to the local microenvironment and thus proneness to chemical damage from transfection reagents (Jiang and Chen, 2006). Aggregation of the sensor was also visible within the cytoplasm for cells with

the initial 2µg/µl concentration of DNA transfected. (Figure 37-A). This could be due to the mis-folding (Krasowska et al., 2010) or oligomerisation (Costantini et al., 2012) of the fluorescent proteins, and was eliminated when the concentration was reduced to 1.5µg/µl. As this appears to be caused by either over-expression of the sensor or unhealthy cell uptake, these cells were excluded from any quantification.

Due to the somewhat unreliable nature of cultured primary neurons, with combined relatively low survival and transfection rates, the number of sampled cells was lower than the above HEK cell experiments.

Figure 38 portrays the averaged response (*n=8*) to forskolin with the $^{T2}Epac_{Q270E}^{VV}$ sensor. Despite a stable baseline, and the typical response curve, the dynamic range appears greatly reduced when compared to the HEK cell studies, a 69% reduction in maximum FRET change. This would indicate that either the sensor is less sensitive in this culture, or that the neurons have a higher cAMP level at their resting state, and thus cannot purport a higher change without reaching the minimum FRETting contribution of the sensor (i.e. the resting state is a already close to the maximum possible response).



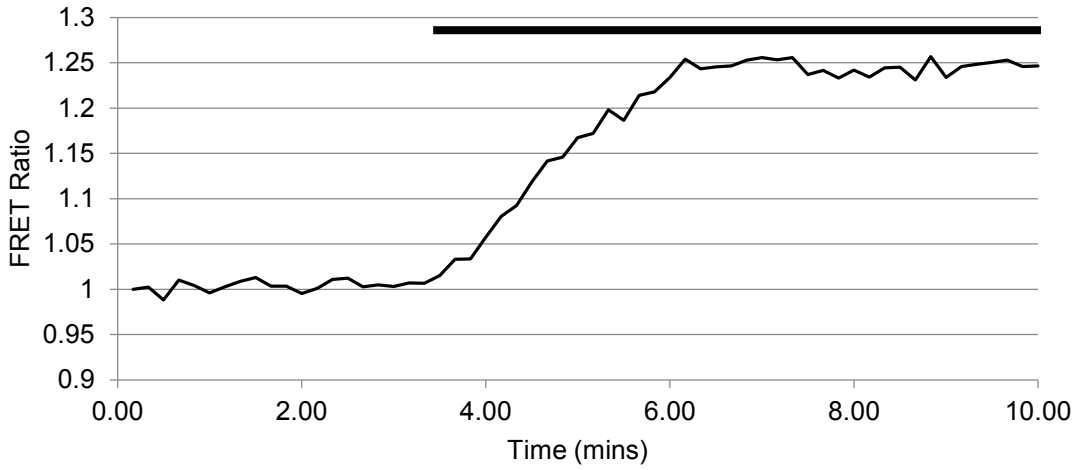


Figure 38 FRET in Primary Neurone Cultures 100μM forskolin was added at 120 seconds to mT2-VV expressing PNCs cultured onto glass coverslips. Images were acquired via confocal microscope with both blue and yellow channels for ratiometric FRET quantification. Above shows an example set of images for the first seven minutes of the mT2-VV experiment.

7.4.2 PNC FLIM

PNC FRET-FLIM was recorded on a modified, inverted confocal microscope with output to a hybrid PMT that could be recorded by the TCSPC system for FLIM measurements.

Upon addition of forskolin, lifetime increased by approximately 500ps for the $^{T2}Epac_{Q270E}^{VV}$ sensor, comparable to the HEK experiments in the previous section Figure 39.

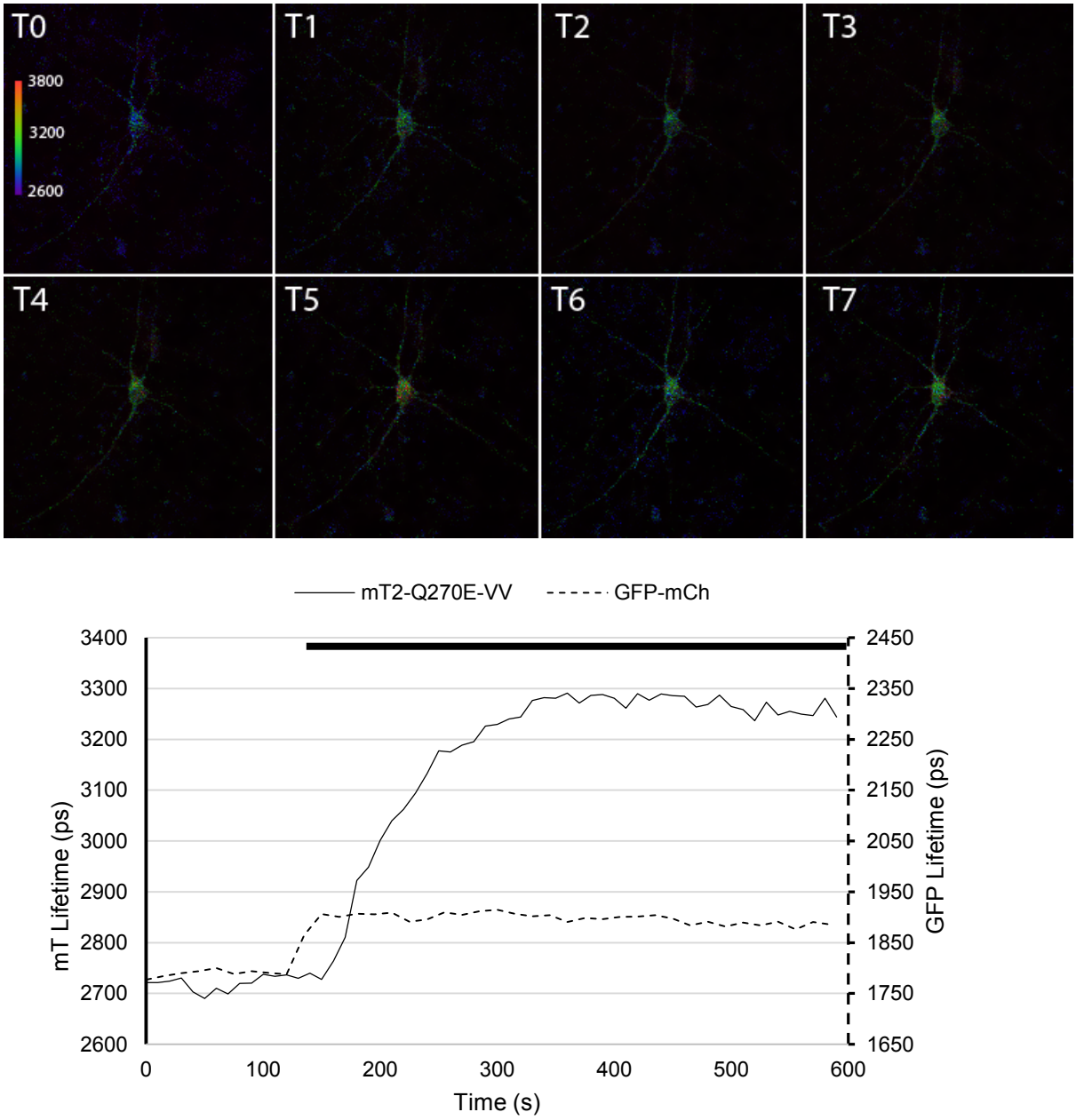


Figure 39 PNC 2P-FRET-FLIM Response to forskolin. 100µM forskolin was added at 120 seconds (black bar) to PNCs cultured onto glass coverslips. Images were acquired via confocal microscope with FLIM attachment. Above shows an example set of images for the first seven minutes of the mT2-Q270E-VV experiment.

7.5 OSC STUDIES

The organotypic slice cultures (OSCs) provide an ideal step towards an *in vivo* system, providing a more physiological environment and architecture than in PNCs.

As the sections are grown on culture inserts, consisting a synthetic membrane, they cannot be imaged on an inverted microscopy system. This, combined with the nature of the deep

neurons labelled with gene gun transfection, make confocal imaging inappropriate for a reliable ratiometric FRET response, and so this section contains only FLIM measurements of the sensors within the soma of labelled neurons.

7.5.1 OSC FLIM

FRET-FLIM recordings were made by removing the OSC from culture and securing it within the perfusion insert detailed in Chapter 6, Figure 23. This provided a system whereby an upright microscope equipped with a suitable dipping objective lens can image the slice whilst drugs are added and a continuous supply of imaging solution can be maintained.

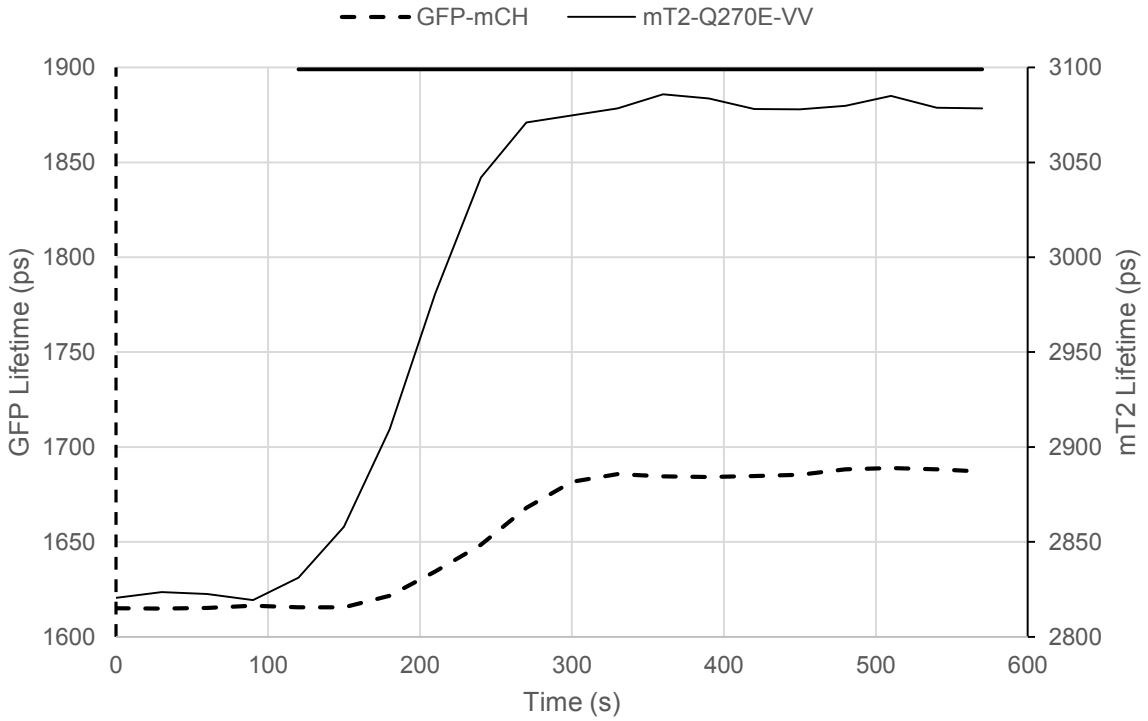


Figure 40 Forskolin-induced responses in OSCs for both GFP-EPAC-mCherry and mT2-Epac-Q270E-VV sensors. 100μM forskolin was added at 120 seconds via perfusion system. Images were taken on a 2-photon microscope with FLIM attachment. *n = 12 cells across 12 slices for mT2 and n = 10 cells across 10 slices for GFP sensors.*

Further to the previous experiments, the $^{GFP}Epac^{mCh}$ and $^{T2}Epac_{Q270E}{}^{VV}$ sensors were transfected into different 21-28 day old OSCs via biolistic technique. Upon stable expression of the sensors at five days post-transfection, sections were mounted and imaged over a 10 minute time course with the addition of forskolin at the two minute timepoint. The results from the two sensors is show in Figure 40. As was found in the PNCs previously, the resultant FLIM

signal after 100μM forskolin addition showed a higher degree of sensitivity in the mTurquoise2 variant, with a 275ps maximum lifetime change, compared to a 74ps shift in the GFP-based sensor.

7.6 PROCEEDING WITH THE OPTIMUM SENSOR

From the above findings, the sensors displaying the highest degree of sensitivity for each red-green and blue-yellow pairs were the $^{GFP}Epac^{mCh}$ and $^{T2}Epac_{Q270E}{}^{VV}$ sensors respectively.

The FRET-FLIM data for the maximal changes in these sensor's activity, used to determine sensitivity, is depicted for each culture medium in Figure 41. While the largest change in lifetime appeared in the $^{T2}Epac_{Q270E}{}^{VV}$ PNCs, the key finding is in the high sensitivity of this blue-yellow sensor in OSCs, when compared to the $^{GFP}Epac^{mCh}$ probe. As the levels of synaptic changes can best be observed with OSCs, this highly sensitive readout of cAMP activity from the $^{T2}Epac_{Q270E}{}^{VV}$ sensor made it the ideal choice for investigating changes in cAMP concentration at sites of synaptic plasticity.

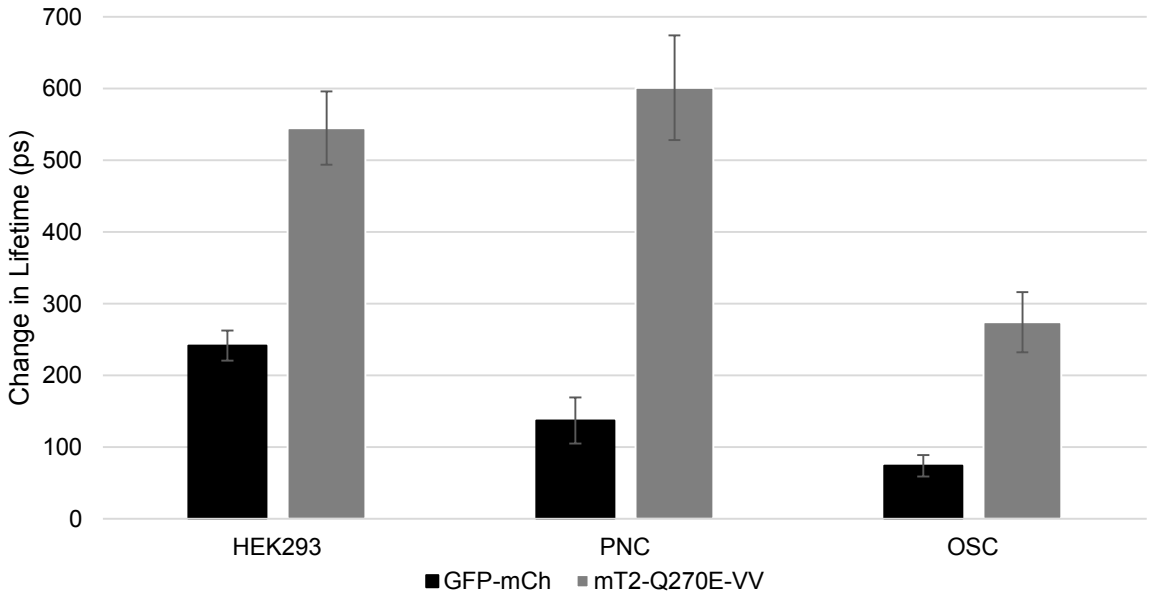


Figure 41 Comparison maximal FLIM measurement Mean response after forskolin addition in all mediums and for both GFP-EPAC-mCherry and mT2-Epac-Q270E-VenusVenus sensors.

The higher responses within the HEKs and PNCs could well be due to the accessibility of the forskolin to the cell monolayer, as opposed to potential diffusion issues in OSCs, with neurons being up to 150µm deep. The transfection efficiencies of the sensors into different cultures may also account for the differing levels of sensitivity. HEK293T cells are renowned for their ease of culture and transfection, producing the highest levels of fluorescent intensity and thus protein copy number. While intensity alone should not influence lifetime recordings, it is possible that a greater number of sensor complexes could bind more cAMP within the cells. HEK cells are also not neurons, and thus the role of cAMP in controlling downstream signalling pathways promotes different functionality and therefore different levels of activity would be expected (however, it should be noted that HEK cells do also express voltage-gated Ca^{2+} channels, regulated via the cAMP-PKA pathway (Gao et al., 1997)).

From this data, it appears that the far greater dynamic range of the mTurqoise2 sensor outweighs any spectral advantage of the GFP-sensor. The previous sections detail its response to a high dose of forskolin, and while this far exceeds the typical, physiological cAMP concentrations expected unstimulated *in vitro*, it highlights a range capable of detecting the small changes occurring in cAMP concentrations at synaptic sites.

In conclusion to this initial optimisation stage of the project, the ideal system for visualising neurons as close to *in vivo* as possible appears to be the OSCs, transfected via gene gun. The sensor of choice is the $^{T2}Epac_{Q270E}^{VV}$ construct, yielding a very high degree of sensitivity to cAMP changes.

In order to assess how these changes occur in relation to synaptic changes, high resolution imaging of synapses is required to determine changes in their size, and therefore strength. Only then can these plastic changes reminiscent of LTP and LTD be correlated to the functional readout of FRET-FLIM recordings.

8 COMBINING cAMP ACTIVATION AND SYNAPTIC STRUCTURAL CHANGES

8.1 RAPID SYNAPTIC CHANGES OCCUR IN OSCS

Typically in response to environmental changes, or direct stimulation to animal sensory systems, rapid synaptic changes occur. *In vivo* recordings have found pre-synaptic sites to undergo a 7-50% turnover in just seven days in mammals (De Paola et al., 2006; Stettler et al., 2006; Yamahachi et al., 2009). While there is an observed phenomenon of short-term synaptic changes, found on both sides of the synapse (Catterall and Few, 2008; Fioravante and Regehr, 2011) whereby calcium channels undergo modulation on a time scale of milliseconds to seconds; these are only short lasting and thought to underlie information processing, rather than long term storage.

To establish whether synaptic changes could be detected over a time period suitable for FRET-FLIM recordings, transgenic mice endogenously expressing GFP under a Thy-1 promoter were used to establish basal synaptic turnover rates. These 'GFPm' mice (Feng et al., 2000), express sparse neuronal labelling of GFP in the cortical regions. OSCs were generated from these mice, and allowed to mature *in vitro* for at least two weeks for full synaptic establishment.

2-Photon imaging with an upright imaging system was then used to record axonal processes at a high resolution in three dimensions for post-processing bouton analysis.

Initially, images were taken at 24hr time points, to observe gross morphological changes occurring over moderate time periods. Figure 42 portrays the software used, showing how each process is tracked in three dimensions, after which each swelling of fluorescence, the EPBs, are numbered and tracked throughout the time course (Song et al., 2016). An example

of long-term changes can be seen in Figure 43, showing the genesis and degradation of entire synapses over a period of four days.

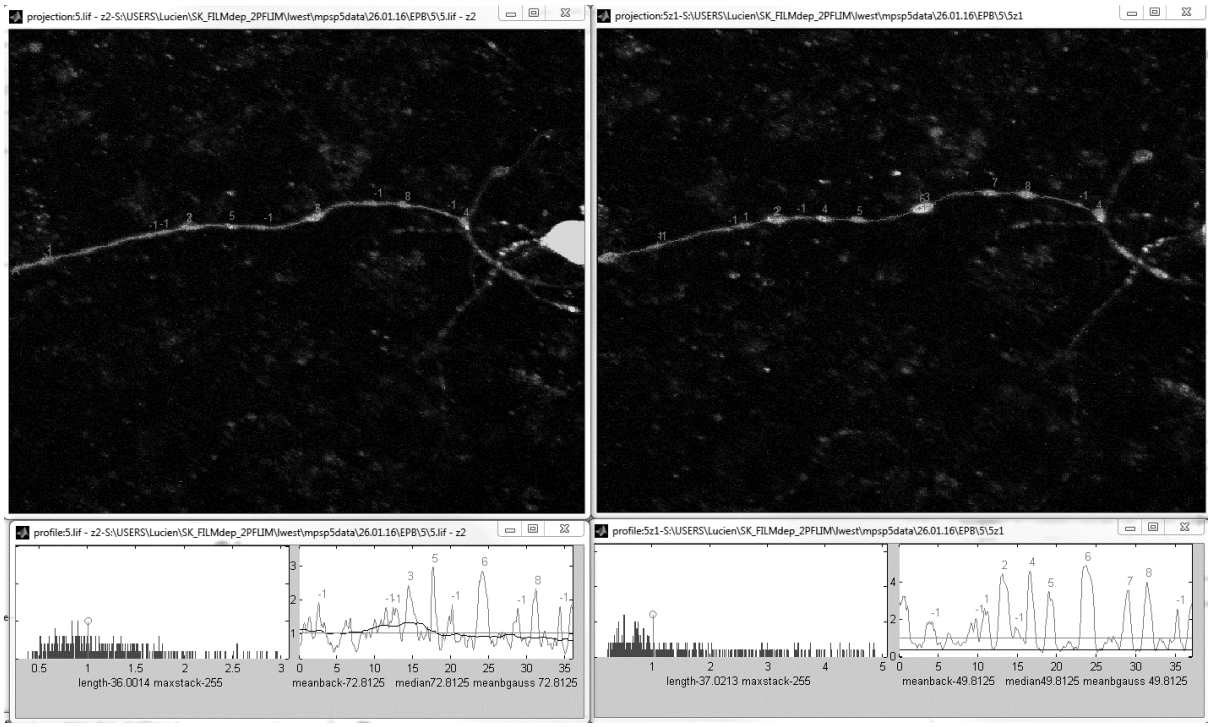


Figure 42 The EPBscore software This screenshot shows the comparison of two imaging sessions side by side, with the identification and numbering of each bouton along the axon. By comparing the intensities to the axon backbone, normalised size changes are recorded during the time course, with each EPB tracked throughout.

While this confirms a high rate of turnover for synaptic boutons in OSCs over a manner of days, FRET-FLIM experiments would ideally be carried out over hours, a limitation governed by the survival and physiological health of the cultures once immersed for imaging and kept outside of the incubator.

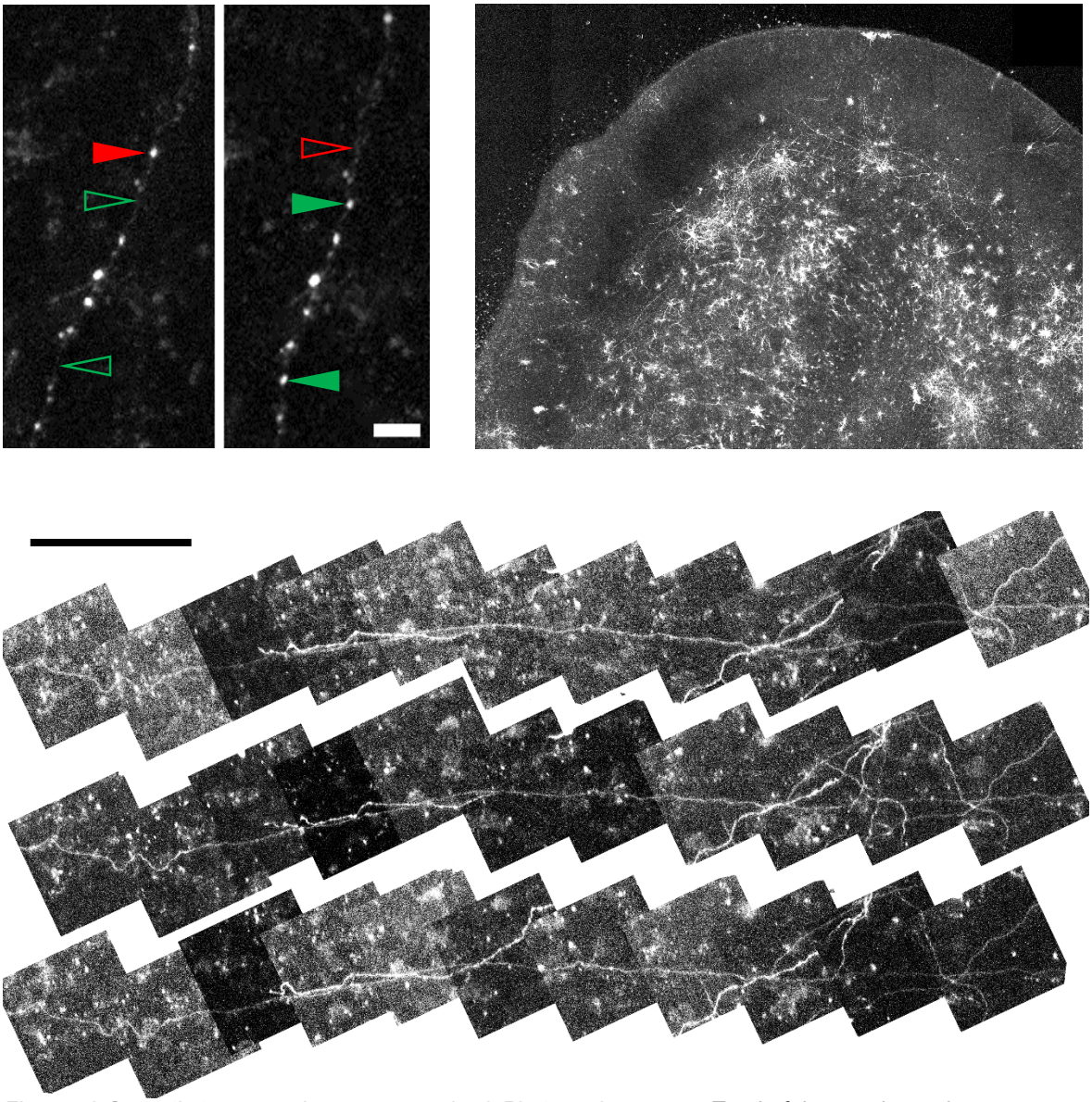


Figure 43 Synaptic turnover along axons under 2-Photon microscopy. Top-Left image shows the same axon over four days with synapses lost (red) and gained (green) (scale = 5μm). Top-right shows a 2-photon series of tiled images joined together for identifying healthy axons on a macroscopic scales. Bottom image shows the same axon stitched together over a series of images and then aligned for the time series (scale = 500μm).

To assess this, axons in OSCs were selected with high densities of synaptic boutons. These were then imaged at high resolution, and then imaged regularly for 90 minutes. To study net changes in size over this time period, the first and last image sets were then analysed with the EPBscore software to determine changes over time. Interestingly, size changes were seen to fluctuate even within just the first hour of imaging. While there was no overall change in total number of synapses, as seen over days, there was evidence to suggest synapses enlarging and shrinking over hours The results are shown in Figure 44, showing the distribution of data

mostly (42%) remaining in the ‘stable’ category, whereby no major change in size was detected.

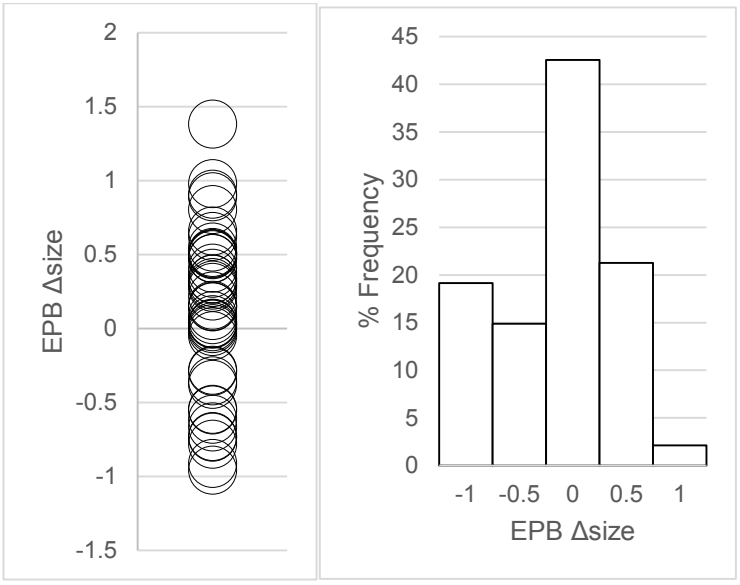


Figure 44 EPB Size Changes in OSCs over 90min time period. EPB sizes were calculated using EPBscore software which measures bouton intensities compared to the axonal backbone. Left shows the raw plots for the 47 boutons recorded with the change in size (size of bouton at t90-t0). Right shows a histogram of the boutons imaged.

8.2 cAMP Compartmentalisation

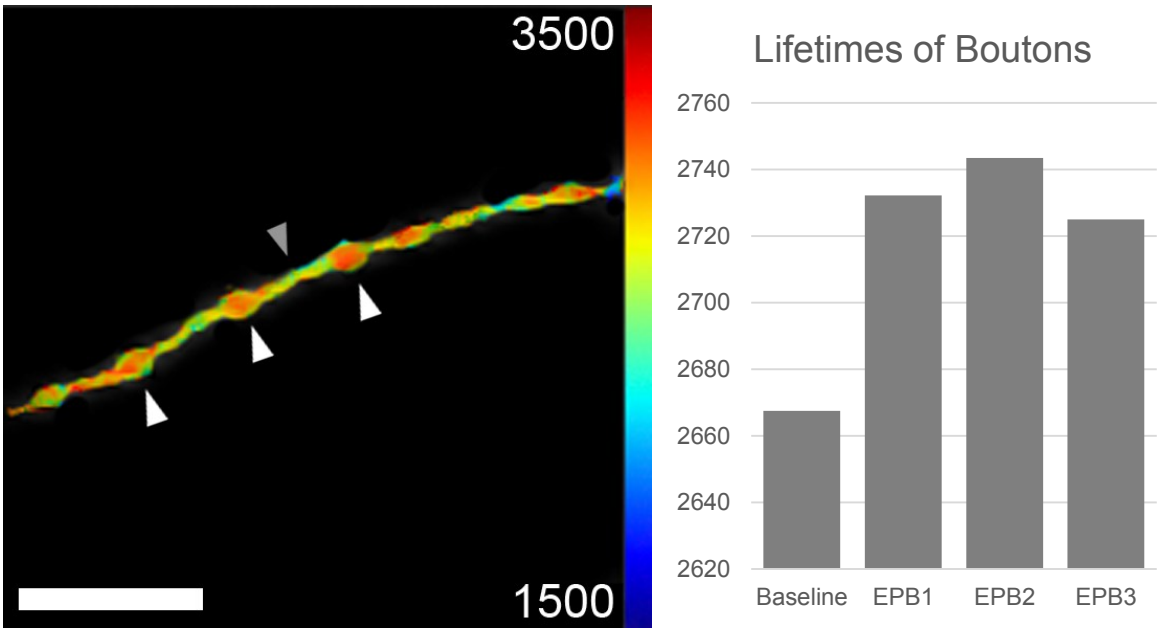


Figure 45 Example of compartmentalisation of cAMP at axonal boutons. Left FLIM image with colourmap displaying the signal from the FRET sensor along an axon of OSCs in vitro. EPBs have been indicated with white arrowheads, and the axon backbone with a grey arrowhead (scale = 5µm). Right Quantification of lifetime signals at the boutons and at the baseline (axon backbone) of the left-hand image.

From transfections of the $^{T2}Epac_{Q270E}{}^{VV}$ sensor in OSCs, and with high magnifications on a multiphoton, FRET-FLIM system, compartmentalisation of signal can be seen to cluster along the axon, at sites of EPBs. This implies a reduction in FRET, suggesting a higher cAMP concentration at pre-synaptic sites. An example of this can be seen in Figure 45, with boutons indicated by white arrowheads, when compared to the axon backbone (grey arrowhead). This level of resolution and signal to noise ratio verifies that the selected sensor is capable of detecting these minute changes in signal revolving around endogenous cAMP compartments in neurons.

Due to the limitations of time-resolution in FLIM imaging, i.e. the long periods in which photons are counted, the image must be binned at a relatively low resolution, typically $256px^2$. Due to the lengthy acquisition time, three dimensional imaging is prohibitively slow, and thus all images acquired in only two dimensions. This limits the ability and accuracy for structural changes to be measured using the EPBscore software.

To circumvent this, multiphoton z-stacks were acquired along with FLIM photon counts simultaneously. This is achieved by allowing the microscope software controlling 2-photon scanning to run concurrent optical sections as an *xyzt* series, with approximately six full stacks per minute. The FLIM detector counts all photons received, regardless of z-position resulting in a mean mapping of the entire stack, the same result as an average projection of the images applied in post-processing. This also has the advantage of taking the lifetimes of fluorescence molecules located throughout the cytoplasm, not just in the sub-micron section in focus. It also provides a useful antidote to z-section drift of the sample during imaging, an issue exacerbated by temperature equilibrations upon bringing 37°C sections onto a room temperature imaging platform.

The synapses themselves accumulate a high concentration of fluorescent proteins, in comparison to the axon backbone. This is due to the swelling of the process, drawing in a greater volume of cytoplasm and with it the fluorescent sensor. It is this higher level of intensity that the EPBscore software that measure bouton size and strength is based upon. In the case of cAMP compartmentalisation, there is a possibility that the increased sensor intensity at the synaptic sites could somewhat skew the resulting cAMP concentration observations. This could be a direct influence from there being more copies of the sensor, which can in turn lead to inter-cellular FRET signals (Ashkenazi et al., 2014), whereby the donors from one sensor complex can FRET with the acceptor of another. Other possible influences could be from the local micro-environments at the synapse (e.g. pH) affecting the fluorescent proteins (Ishii et al., 2007).

To control for this, the donor of mTurquoise2 alone was transfected into slices and the same experiment was carried out, imaging over a 90 minute time window and monitoring boutons along the axon. In total, 6 axons from different slices, along with their boutons (21 in total), were then pooled together and compared to their respective backbones, showing no significant difference (*t-test, p>0.1)* in lifetime between bouton and axon. An example of this from one slice is depicted in Figure 46.

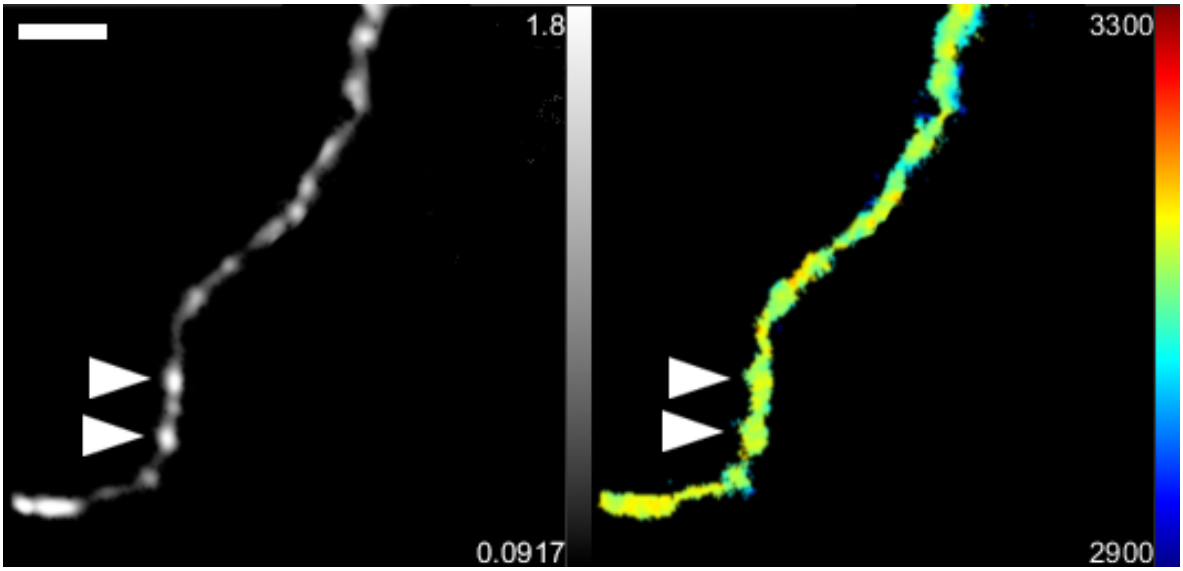


Figure 46 Donor expression only of mTurquoise2. The donor construct alone was transfected into OSCs and axons were imaged with EPBs present (white arrows). The left image shows an intensity-based projection for structural information, while the right image shows the fluorescent lifetime measurements across the region of interest. Scale bar = 5µm.

8.2.1 Compartmentalisation is maintained even after drug induced changes

Upon addition of forskolin to slices being imaged, compartmentalisation of cAMP signal within the boutons is preserved, showing a tandem rise in cytoplasmic concentration, yet spatially segregated from the surrounding axon.

Images were segmented to isolate a portion of axon backbone that did not undergo morphological changes as well as the boutons that could be clearly identified and resolved. The lifetimes were then fitted and the mean difference between them was calculated across the entire time series, providing a value of 173±23ns (n=11) difference. Lifetime differences at the initial time point and at the peak response after forskolin addition were then averaged and compared to reveal a ‘catching up’ axon baseline to bouton of 72ns (t-test, $p<0.01$), shown in Figure 47.

These results would indicate not only a segregation of cAMP concentration within *en passant* boutons, but also either a localised upregulation, caused by adenylate cyclase complexes

native to the synapse (Bonci and Williams, 1996; Williams et al., 2001); or an increased level of intracellular trafficking of cAMP to the synapses, preserved during adenylate cyclase stimulation, made possible by the rapid diffusion of cAMP through the cytosol from isolated adenylate cyclase receptors in the plasma membrane (Kotaleski and Blackwell, 2010).

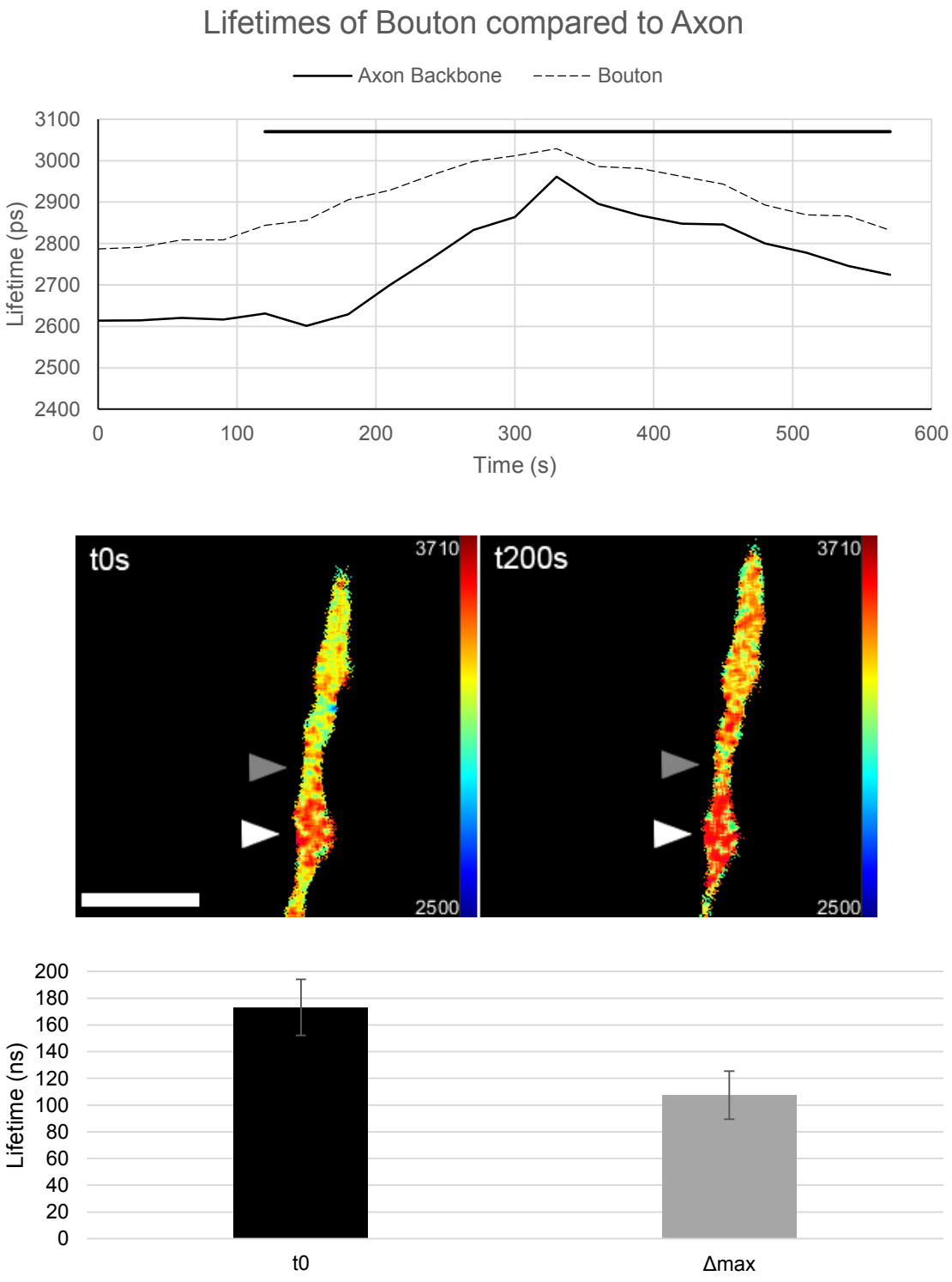


Figure 47 cAMP compartmentalisation preserved when forskolin is added Top: Plot of lifetime over time series of axons with individual boutons sampled and compared to the surrounding axon backbone. 100μM forskolin added at 120 seconds. Middle: Images from the dataset showing an axon with EPB before and after stimulation showing lifetime. Bottom: comparison of the peak values between axon backbones and EPBs at the maximal responses after forskolin stimulation. At t_0, before the addition of forskolin, there is a difference of 173ps between the lifetime of the boutons and axon backbone. Upon addition of forskolin, at the maximum response, Δmax, the difference between boutons and axon has reduced to 107ps. n=*12 boutons across 3 axons in 3 slices.*

8.3 INCREASED cAMP LEVELS ARE DETECTED AT SITES OF SYNAPTIC STRENGTHENING

By combining the multiphoton images generated from the acquisition software and the FLIM data acquired from the TCSPC equipment, the volumes and volume changes of pre-synaptic sites can be directly correlated with cAMP concentrations.

First, the three dimensional optically sectioned images that were obtained as high resolution stacks before and after the time window were processed using the EPBscore software, effectively scoring bouton size and intensity in relation to the axonal backbone. The same boutons were then segmented with the FLIMfit software and the lifetime decay was fitted for each 60s timepoint over the imaging session. An area of the axon that did not undergo synaptic events was also segmented to provide a baseline value. These lifetimes were then averaged, the baseline was subtracted, and these lifetime differences were combined with the EPBscore readout to provide a dataset of both size change and FLIM signal for each synapse in comparison with its axon.

Upon plotting of the data, a trend became apparent for synapses that showed in increase in size over the imaging period, also displaying an increased lifetime when compared to the axonal backbone on which they were situated (Figure 48). When the distribution of synaptic change is compared to the data collected from GFP-expressing OSCs from section 8.1, the mean synaptic changes are calculated as 0.1105 for the baseline, no FRET sensor group, and 0.2410 for this FLIM-measured series. These are not significantly different ($p>0.1$), indicating that the distribution of synaptic changes were not affected by the FRET sensor or imaging protocol.

To interpret the data, two groups were defined: synapses that increased in size over the 90 imaging period, and those that remained stable or decreased (enlarged and non-enlarged, respectively). These groups were isolated via k-means cluster analysis. This method clusters statistically similar groups, derived from comparisons of their data attributes (Kanungo et al.,

2002; Scott and Knott, 1974). Using this method, as opposed to simply segregating groups based on positive or negative integers in size, allows for unbiased separation and accounts for possible noise in the systems, both optically and biologically: as seen from the clusters, size changes of between 0 and ~±0.25 are discarded from the enlarged group, suggesting these are within baseline error rates.

This data is displayed in Figure 48, whereby each data point represents an *en-passant* bouton either growing or shrinking (x-axis) with a higher or lower lifetime than the axonal backbone (y-axis). The different series represent the different *k* clusters, namely the enlarged boutons (red, *n*=23) and the non-enlarged (black, *n*=35).

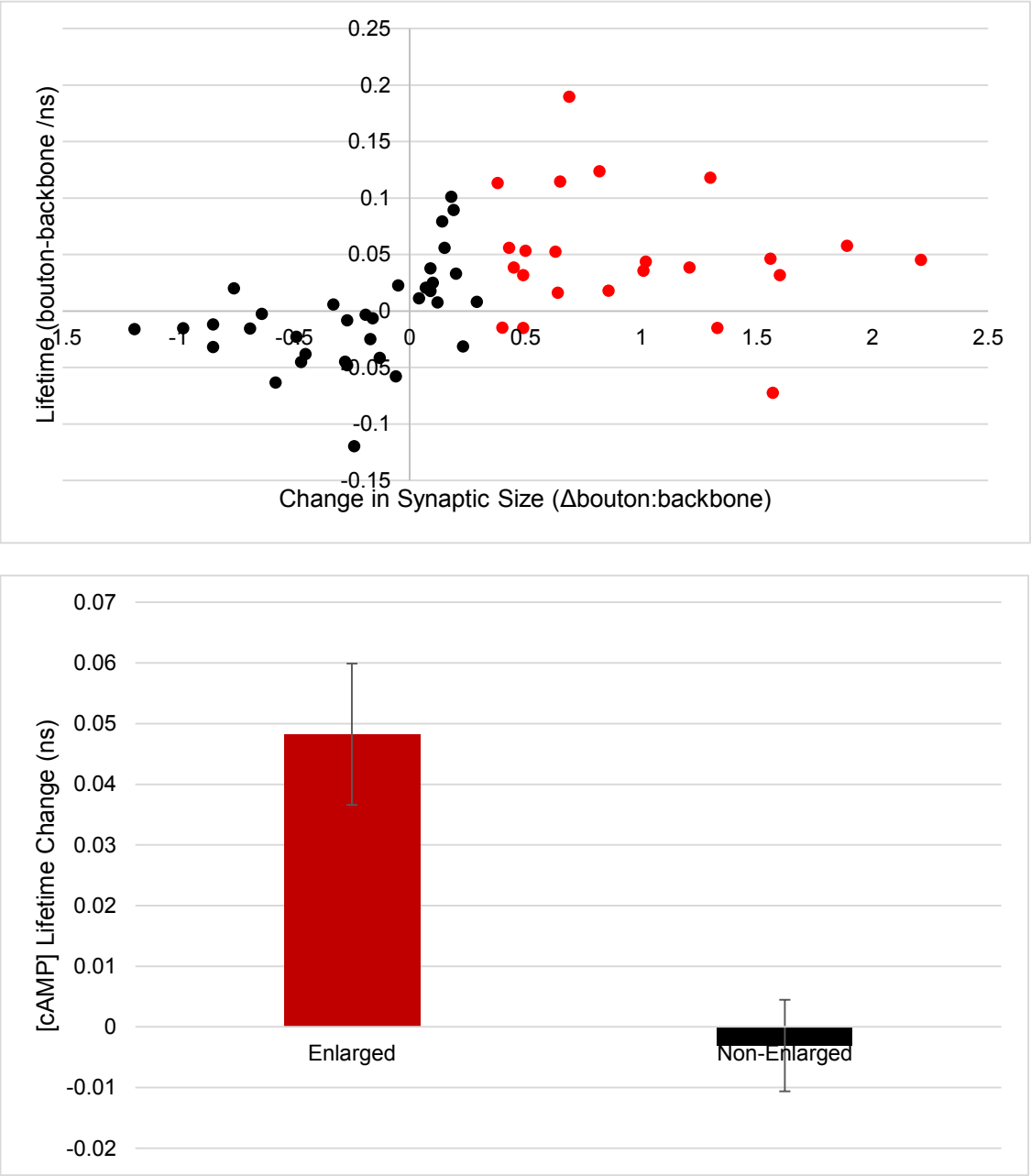


Figure 48 Correlation of cAMP concentration (FRET-FLIM) with bouton size changes (2P) Above: Individual synapses plotted by their change in size (according to a change in the bouton:backone ratio at t0 and t90) vs the changes in FRET lifetime recorded. Therefore, the top-right portion (positive in both axes) depicts synapses that grew in size and displayed an increased cAMP concentration. The red and black data points represent the enlarged and non-enlarged clusters respectively after k-means cluster analysis. Bottom: Pooling of these two clusters and plotting of averaged cAMP signal. *n = 59 total synapses across 21 axons with 1 axon per slice.*

The different groups can then be compared statistically, first identifying that there is a significant difference in lifetime (and therefore presumably cAMP concentration) in the synapses between them ($p<0.01$, two-tailed student's t-test, assuming equal variance), yet linear regression showed no correlation ($R^2=0.03$) in the enlarged group.

This suggests that the increased concentration of cAMP is found almost entirely in enlarging, and therefore strengthening, boutons, yet there is no linear relationship in size change and cAMP concentration. There was also no significant correlation via linear regression of cAMP concentration within boutons that remained stable or decreased in size. This shows an association between cAMP-dependent pathways and the strengthening of synapses, theoretically LTP-inducing, however was not observed in weakening (suggestive of LTD) and stable boutons.

This is concurrent with the findings of other groups, who have shown the upregulation of cAMP at synapses undergoing LTP (Huang et al., 1994; Weisskopf et al., 1994a). However, a marked decrease of cAMP sites of LTD has been reported (Atwood et al., 2014; Bailey et al., 2008; Tzounopoulos et al., 1998), yet was not significantly observed in the data.

9 MATERIALS AND METHODS

9.1 DNA

9.1.1 Constructs

9.1.1.1 FRET sensor constructs

Plasmids for the FRET sensors H74, H126 and H134 were kindly donated via MTA from the lab of Kees Jalink from the Netherlands Cancer Institute (Klarenbeek et al., 2011).

The CFP-EPAC1-YFP and CFP-EPAC2-YFP sensors were obtained from the lab of Dr. Ulrike Zabel, University of Würzburg.

9.1.1.2 Fluorescent Proteins

mCherry (pmCherry-C1, Clontech), eGFP (peGFP-N1, Clontech) were kindly donated by Dr. Alex Sardini

mTurquoise, Venus and eCFP were provided by the Kees Jalink Lab.

9.1.2 Amplification

Plasmid DNA to be amplified was transformed into One Shot® TOP10 Chemically Competent E. coli (ThermoFisher Scientific) using the 'rapid chemical transformation procedure': Centrifugation of samples, thawing of cells on ice, addition of 5µl DNA, five minute incubation on ice and then direct spreading onto LB agar plates at 37°C. Depending on the antibiotic resistance within the plasmid (namely Kanamycin or Ampicillin, Sigma), plates were prepared from molten LB agar mixed with 50µl/ml of the appropriate antibiotic.

After overnight incubation, isolated colonies were selected with a pipette tip and were used to inoculate LB Broth with appropriate antibiotic for another 12-16hrs.

Purification of plasmids were then carried out with a range of QIAGEN Plasmid purification kits: Mini, Maxi and Giga sizes following the respective protocols.

To assess levels of protein contamination and DNA concentration, samples were then taken and analysed via the Nanodrop (Themo Scientific) System, being loaded after blanking with the same elution buffer.

9.1.3 Sequencing

Sequencing of amplified plasmids was performed to confirm the amplification of correct DNA sequences. Primers were designed with the use of the Geneious software (Biomatters Ltd.) suite and in line with typical primer requirements (appropriate annealing temperature and length).

Samples were combined with primers and processed in house by the sequencing facility before being checked against template strands in the aforementioned software.

9.2 ANIMALS

For initial bouton observations, Thy1-GFP-M transgenic animals were used (Feng et al., 2000), sparsely expressing GFP in excitatory neurons in both cortical and sub-cortical regions. To screen for GFP positive animals, ear notches were taken and then viewed under dissection microscope under the appropriate filter and wavelength to observe GFP-expressing cells in the epithelial tissues of the pinna.

For sensor tests, as the animals needed to be void of any transgenic fluorescent signal, wild-type CD1 animals were used (Harlan).

All experiments were carried out in accordance with the United Kingdom Animals Scientific Procedures Act of 1986. In addition all procedures were authorized via personal licence, held under the project licence of the Neuroplasticity and Disease group.

9.3 LIVE CULTURES

9.3.1 HEK Cell Culture

Initial expression of fluorescent proteins and sensors were tested in human embryonic kidney cells (HEK293Ts).

Cells were grown in volume in T175 (ThermoScientific) culture flasks, and initially seeded at $4.6x10^6$. Maintenance media constituting: 445ml DMEM (Gibco), 5ml Penicillin/Streptomycin (Sigma) and 50ml foetal bovine serum (Sigma) was used to supply cell requirements. Three times per week, cells were split by: removing media, washing with phosphate buffered saline (PBS), applying trypsin (Trypsin + EDTA, Sigma), five minute incubation at 37°C, further PBS wash and then application of fresh media. The passage count was kept below 60 to avoid excessive divergence from the parent line. Cultures were kept at 37°C with 5% CO_2.

Cell were counted via haemocytometer, and viability was assessed using a Guava easyCyte flow cytometer (Millipore).

For confocal imaging experiments, cells were seeded onto glass-bottom 35mm petri dishes (MatTek) at a seeding density of $0.3x10^6$ and allowed at least 48hrs to adhere to the base and equilibrate. No coating was required for cell adhesion.

For plate-reader experiments using the photonic's group microscopes, HEK cells were cultured onto optically clear 96-well plates (VisionPlate 96) at a seeding density of $5x10^4$.

9.3.1.1 HEK cell transfection

Transfections were performed with polyethylenimine (PEI, SIGMA), which provided the highest rates of transfection compared to calcium carbonate and lipofectamine based methods. For a 35mm dish, 12µl PEI per 2µg of DNA was mixed into 2ml serum-free media, and applied to the cells for 3 hours. A full exchange of serum-enriched media then completed the process, with visibly transfected cells appearing within 24hrs for CMV-promoted plasmids.

9.3.1.2 cAMP ELISA

For establishing cAMP concentration responses to pharmaceutical stimulation, the Cyclic AMP XP Chemiluminescent Assay Kit (Cell Signalling Technologies, #8019) was used with HEK293T cells in culture.

The procedure consisted of first dissociating cells from culture, lysing to produce a homogenous solution, stopping the reaction and then incubating with horseradish peroxidase (HRP) conjugated to PKA. This produced a varying absorbance spectrum linked to absolute cAMP concentration, run in tandem with a serially diluted cAMP standard (2.4μM) to produce a standard curve to extract concentration values from.

The 96-well plate was analysed via photospectroscopy (ThermoFischer Plate Reader) and levels of absorption at 450nm were converted to concentrations.

9.3.2 Primary Neuronal Culture

Primary neuron cultures were prepared initially by myself, but then continued by Anna Slaviero of the animal physiology team (APT). The following protocol is an adapted method from Lesuisse and Martin (2002) and Kaech and Banker (Kaech and Banker, 2006).

Animals were time-mated and plug-checked to determine embryonic ages of female pregnant mice between 6 weeks and 6 months of age. At embryonic day 17-18 (E17-18), females were euthanized via cervical dislocation and an incision was made across the abdomen to reveal the uterus. This was then cut along the cord to open up the sacs using blunt dissection techniques, removing the membrane to reveal the embryos for removing onto plates. The heads were then removed and placed into PBS on ice to store during cerebral dissection. Under PBS, the cortices were then removed using forceps and scissors, with the skull being only a thin membrane at this point, no stronger tools were required. The meninges were then removed with forceps using a peeling action, with care taken not to damage the tissues. Cortices were then transferred to another dish of ice-cold PBS.

Under a laminar flow hood, extraction of cells was performed carefully and in a highly sterile environment. First, PBS was aspirated off, with only enough to keep cortices submerged remaining. The tissues were then gently dissociated with the side of a scalpel blade, with extremely light strokes made over the cortices. 2ml of trypsin was then added to the dish and then transferred with tissue to a 15ml tube (BD, Falcon) and incubated for 20 minutes in a water bath at 37°C. The tube was then removed, with care taken not to resuspend the tissues that have descended. Trypsin solution was then removed via aspiration to leave only cells. 2ml of 37°C DMEM and FBS (GIBCO, SIGMA) was then added and the tissue was resuspended using a plastic transfer pipette. Once homogeneity was achieved after approximately 12 repetitions with the pipette, a 1ml pipette tip was then used with a P1000 pipette (Gibson) to further resuspend the cells. 10ml DMEM+FBS was then added and the solution was centrifuged at 1500rpm for a total of three minutes.

The supernatant was then discarded via aspiration and 5ml of neurobasal media was added (GIBCO), with 20% more applied to larger pellets. The pellet was then resuspended to evenly distribute cells through the media. Coated 35mm petri dishes (BD) were then filled with 3ml warmed PNC media each. 300µl of cells were then pipette onto the centre of each plate, with minimal disruption, promoting higher densities of cell populations. Plates were then placed at the back of a 37°C, 5% CO_2 incubator, ensuring adequate CO_2 supply was received.

Plates used for culture PNCs were coated prior to dissection in order for cell adhesion to occur. For 5cm dishes, the following protocol was used for coating: 200µl PolyL-Lysine at 1mg/ml was diluted in 20ml PBS, with 1ml of this solution added to each plate and left for four hours to overnight. The lysine solution was then removed via aspiration and plates were further washed three times with sterile PBS. 1ml of 100µl Laminin (SIGMA) disulted in 10ml PBS was then added to each plate and left overnight at 37°C in an incubator. This was then removed the next day and plates were stored under PBS at 4°C until ready to use.

Cultures were then checked after 24 hours and dying/dead cell- containing cultures were discarded. After 48hrs, a further 1ml of neurobasal media was added. From then on, media

was exchanged every 4-5 days. This was performed as a half change, whereby 2ml of media is removed from the total 4ml and replaced with fresh media. If a lot of debris was present, the existing media was syringe-filtered with 0.22µm pore filters.

PNC media consisted of: 500ml Neurobasal media (GIBCO), 10ml B27 supplement (50X, GIBCO), 5ml Streptomycin/Amphotericin B (Life Technologies), 750µl Glutamine 200mM (GIBCO), 1µl β-mercaptoethanol (SIGMA). The trypsin solution for cell dissociated was made up from 2.5ml Trypsin/EDTA (Life Technologies) and 7.5ml PBS.

9.3.2.1 PNC Transfection

Transfections of PNCs were carried out using Lipofectamine 2000 (Life Technologies) using an adapted protocol from Dalby et al. (2004). 0.8µl of DNA to be transfected was diluted in 50µl OptiMEM (Life Technologies), a serum-free media. 2µl Lipofectamine 2000 was then diluted in 50µl OptiMEM and allowed to stand for 10 minutes at room temperature. The DNA and lipofectamine solutions were then combined allowed to form complexes for 20minutes at room temperature. This provides the approximate 100µl of transfecting solution for one 35mm culture, and so was multiplied by the number of samples to be transfected. Once added, the cultures are left in the incubator for four hours and then topped up with standard PNC media.

9.3.3 Organotypical Slice Culture

OSCs were prepared from a protocol adapted from (Gogolla et al., 2006a).

A 6-well plate (BD) was prepared by adding 1ml of OSC media to the well and then adding a PTFE 0.22µm membrane culture insert (PICM0RG, MiliPore) to rest on top and stored in a 37°C incubator until ready for use

Pups were taken at P3-P5. First, the head was removed with surgical scissors and excision of the brain was carried out by first removing the skin, and then cutting through the skull with fine scissors.

Brains were then removed using a curved blade and submerged in ice-cold OSC media as quickly as possible. Under dissection microscope, the cortices were then removed, carefully avoiding the midbrain. Each cortex was then placed on a tissue chopper and 400µm sections were made using 60% blade force and 30% speed. Slices were then washed into ice-cold media and hemispheres were kept separate.

The slices were then dissociated via flame-smoothed glass Pasteur pipette, broken along the shaft to produce a wider aperture. Pipetting up and down separated the slices with minimal mechanical trauma incurred.

Slices were then left on ice for at least 30 minutes before being placed back under dissection microscope to select for the best specimens, using plastic inoculation loops to gently tease apart conjoined sections.

Selected slices were then individually pipetted onto the membrane inserts in the 6-well plates prepared earlier, one section per insert. After 5-10 minutes, excess media was removed via aspiration and finally plates were moved to a 37°C, 5% CO_2 incubator.

Slices were then maintained by replacing all media with fresh OSC media twice per week and would usually remain healthy for 2-4 months.

OSC media was made up from 394ml sterile water, 6.304g MEM Hanks Powder (GIBCO), 0.5ml 1M $CaCl_2$, 1ml 1M $MgSO_4$, 0.22g $NaHCO_3$, 100ml heat inactivated horse serum (Life Technologies), 5ml 100X Antibiotic Antimycotic Solution (10,000 units penicillin, 10 mg streptomycin and 25µg amphotericin B /ml, SIGMA), 24µl 25% Ascorbic Acid, 0.5ml 1mg/ml insulin (Life Technologies). This was pH adjusted to 7.27, osmolarity adjusted with distilled water to 300osm and sterile filtered at 0.22µm. Stored at 4°C for up to one month.

9.3.3.1 Electroporation

Electroporation trials, as detailed in section 5.2.1, were carried out with glass electrodes (Harvard Apparatus), pulled on an electrode puller (Harvard). Silver wire (250µm, RS

Components) was then used inside the electrode and coiled up to be used a ground electrode when required. Electronic pulses were delivered using an electroporator (Nepagene) set at either 25V or 50V, running at 100ms trains every 50ms. Oscillator recordings were taken in parallel with the anode.

When constructing electrodes for different trials, 250µm silver wire was manipulated to fit a 10µl pipette tip. This included the use of a flame to melt and pull wire into fine points, as well as epoxy adhesives to attach it to the tip.

9.3.3.2 Viral Transduction

The viruses used were AV-CRE-EGFP, LV-GFP and AAV9-SYN-EGFP. Aliquots were defrosted and used within 2 freeze-thaw cycles and 10 µl was topically applied to slices and left to transduce for 1-4 days.

9.3.3.3 Gene gun

Biolistic transfection was carried out with the Helios Gene Gun (BioRad) with different preparations of bullets.

9.3.3.3.1 Bullet preparation

First, a total of 50µl of DNA solution was made up with up to 50µg DNA diluted in the distilled water to match the total volume. Up to 8mg of the selected diameter gold particles were then weighed out and set aside. 100µl 0.05M spermidine was added to the gold and sonicated for approximately twenty seconds whilst dipping the microcentrifuge tube in and out of the sonicator, preventing over sonication. The DNA solution was then added to the gold along with 100µl $CaCl_2$, the latter added drop-wise while vortexing simultaneously to avoid precipitation. DNA was then left to precipitate onto the gold particles for 10 minutes at room temperature. DNA was then centrifuged for 30 seconds to pellet the bullets. This was followed by three washes of new, unopened ethanol with sonication and centrifugation between each step.

The pellet was then resuspended in 3.5ml 50µg/ml polyvinylpyrrolidone (PVP) dissolved in ethanol. This was performed 200µl at a time to ensure complete transfer. One metre of plastic tubing was connected to 0.4bar of oxygen-free nitrogen on a rotating stand to enable complete drying of tubing for 20 minutes minimum.

The tubing was then connected to a 10ml plastic syringe (BD) and the gold-PVP solution was drawn up into the tubing. This was then left to settle in the tubing for five minutes before tubing was rotated 90° and then 180° to fully coat the lumen. The PVP solution was then drawn off slowly and then nitrogen was reapplied for 10 minutes with continuous tube rotation to complete drying.

Tubing was then cut into 12mm sections with a razor blade and stored in glass vials with a desiccation pellet present to remove residual moisture.

9.3.3.3.2 Biolistic firing protocol

Gene gun components – the barrel, membranes and magazine, were perpetually stored under 70% ethanol to prevent contamination. These were first air dried in a laminar flow cabinet. Individual tubing sections coated with the DNA-Gold to transfect were inserted into the revolving magazine at pre-allocated positions. The gauze was then attached to the barrel and this was screwed into the gene gun along with the insertion of a 9V battery. Medical-grade helium was then connected via specialised regulator (BioRad) and a pressure of 200bar was applied.

Upon complete charging of the equipment, one empty chamber was fired to clear out the barrel, followed by the positioning of the barrel 2-3cm above the section to be shot and bullets were then discharged in order.

Brain slices were then placed back in the incubator and monitored for plasmid expression.

9.4 DRUGS

The drugs used for modulating changes in cAMP levels during live cell imaging trials were: Forskolin (Sigma, F6886), 3-isobutyl-1-methylxanthine – IBMX (Sigma, M2547) and MDL-12,330A (Santa Cruz, 40297). The cAMP analogues were 8- Bromo- 2'- O- methyladenosine- 3', 5'- cyclic monophosphate, acetoxymethyl ester (8-Br-2'-O-Me-cAMP-AM) and 8- Bromo- 2'- O- methyladenosine- 3', 5'- cyclic monophosphate (8-Br-2'-O-Me-cAMP) (both BioLog, B022 & B028 respectively). Finally, ionomycin (Sigma, I9657) was used to stimulate Calcium release with the Troponin-C sensor. All compounds were dissolved in either DMSO or distilled water, as recommended in their data sheets. Unless otherwise state, forskolin was used at 100µM.

9.5 SOLUTIONS

9.5.1 Physiological Solution –HEK Cells

HEK293T cells were imaged in an ion balanced, physiological solution buffered with HEPES in the case of unenclosed microscopes. This was omitted in the case of SP5 experiments that included a CO_2 perfusion system and maintained acidic pH.

NaCl	KCL	MgCl2	CaCl2	HEPES	D-Glu
130mM	5mM	0.5mM	2mM	10mM	5.5mM

Table 7 Physiological solution for HEK cell imaging.

The above salts were dissolved in sterile water and pH adjusted to 7.4. Osmotic balance was maintained at 280-300osm.

9.5.2 Artificial cerebrospinal fluid – OSCs

When imaging OSCs, an artificial cerebrospinal fluid (aCSF) was prepared, allowing for maintenance of ion and osmotic balance during imaging. The last two salts were added on the day of experiment to prevent precipitation over time. This was pH adjusted to 7.3 and adjusted to meet 300osm.

						Added on day of experiment	
NaCl	**HEPES**	**NaHCO3**	**D-Glu**	**KCL**	**NaH2PO4**	**MgCL2**	**CaCl2**
130mM	20mM	2mM	25mM	2.5mM	1.25mM	2 mM	2mM

Table 8 Artificial CSF solution for OSC imaging.

9.6 PERFUSION SYSTEM

In order to establish optimum solution exchange, a perfusion setup consisting of a plastic insert and a micro-dialysis pump were utilised. For HEK cell studies, a 35mm petri dish insert (Harvard Aparatus) was affixed via vacuum grease (Sigma) to the inside of a glass-bottom 35mm imaging dish (MatTek). For OSCs, a custom 3D printed insert was adhered to a standard glass imaging slide with grease. To construct this insert, a MakerBot Replicator I (MakerBot Industries) filament extrusion 3D printer was used with both ABS and PLA plastics (MakerBot Industries). An acetone-plastic 'slurry' was applied to the base plate prior to building to aid adhesion and minimise warping. Base plate temperatures were set at 110-120°C, whilst extrusion heads were set to 220°C for ABS and 205°C for PLA. CAD designs were made using Cinema4D (MAXON) software for customised renderings, and then the programming language and environment openSCAD (www.openscad.org) for full virtual design. The ReplicatorG (www.replicat.org) software then allowed for the toolpath to be created into GCODE and parameters for print speed and temperatures were allocated. Each insert took approximately 40 minutes to build. To promote smooth surfaces, some inserts were subjected to a vaporised acetone chamber, whereby 3ml of acetone was applied beneath the structure on an aluminium foil raft and placed in a glass chamber on top of a 60°C hotplate for 20 minutes, smoothing the surface of the model.

The 2-channel perfusion pump (REF) was used with micro-dialysis tubing (Cole-Palmer) of 3mm internal diameter, and 6mm outer diameter. This allowed for attachment of a 20G syringe needle for attachment to either inserts or dipping objective lens. The inlet for the solution was a 50ml centrifuge tube (BD Falcon) with holes made on top for tubing, and was connected to

a tubing 3-way tap (Harvard Aparatus) which allowed for two reservoirs (one containing vehicle and one with drug solution) to be switched between during imaging. The outlet from the insert was sent via the pump to a waste container.

Calibrations for pump speeds were carried out using phenol red dyes and a spectrophotometer to assess the rates of diffusion and speed of full saturation of samples. Unless otherwise stated, the pump rate was set to 25%, a media exchange speed of 1.1ml/min.

Washes of 1%DMSO in sterile PBS were used to rinse the system of residual drugs in between imaging trials.

9.7 SINGLE PHOTON IMAGING

Ratiometric FRET recordings in cell monolayers, utilised a commercial SP5 (Leica) inverted confocal microscope. Laser lines and powers were as follows: Argon 80% (this high power reduces laser oscillations in a gas-laser system), 488nm 3% for eGFP.

Imaging of live cells was performed on a Leica SP5 II confocal with the manufacturer's LAS software. For blue-yellow sensors, an excitation laser of 458nm was used, while the donor and FRET channels were recorded through PMTs with detection bandwidths tuned to 462-494nm and 587-673nm respectively. For red-green sensors, an excitation laser at 476nm was used, and PMTs of 484-541nm and 587-737nm.

Unless otherwise stated, images were captured at 700Hz using z-stacks of 10-13 planes, every 10 seconds across one or two ROI's.

To maintain temperature and allow for the exchange of drugs across the sample, a two-channel peristaltic pump was used connected to a reservoir of imaging solution and attached to a customised insert that affixes to the MatTek glass-bottomed dish. A second line was connected to withdraw liquid from the sample from a certain level. The entire set up was kept

in a thermostatically-controlled case at 37°C. Air with 5% CO_2 was added to provide optimal imaging conditions and maintain pH acidity for culture health.

9.8 TWO PHOTON IMAGING

Two photon imaging for this project took place across three different microscopes on different campuses.

The system used for morphological experiments with GFP in slice cultures was a commercially available 2P laser scanning microscope (Bruker – formerly Prarie Tech.) being supplied via tuneable Ti-Sapphire laser (Coherent). Images were acquired via the PrarieView software suite, also controlling the laser centre wavelength. For this system a 40X (numerical aperture 0.8) or 20X (NA 0.9) (Olympus) water-immersion objective was used ranging from optical zooms of 1-4 each.

A similar system was used at the Max Planck Florida Institute, rather it was controlled via ImageScan MATLAB software and utilised a 63X immersion lens.

For the bulk of the data acquired requiring FLIM recordings, an adapted upright SP5 (Leica) single-photon system was adapted to receive multi-photon input from a MaiTai eHP DeepSee laser (Newport). This system was fitted with a 25X 0.95NA water-immersion lens.

The FLIM detector was a BH150 (Beckler & Hickl) being run on an additional workstation with the included SPCimage acquisition software and coupled with an appropriate PMT.

An instrument response function (IRF) was recorded at the start of each experimental day using gold nanorods (Sigma). The decay was finely sampled (256 binning) and then imported into FLIMfit software to aid fitting of sample data.

9.9 IMAGE ANALYSIS

9.9.1 Grid Scan Stitching

For multiphoton imaging of large sections at high resolution, the Bruker PrarieView software allows for a series of z-stacks to be acquired in a grid layout, with a specified overlap to enable stitching of images.

While ImageJ and other imaging software have the ability to automatically join images (typically just two-dimensional media), the order of scanning and file writing form PrarieView is incompatible. Therefore a custom MATLAB script was written to place images in order, accepting direct input from the 2Photon imaging folders.

First, the filename was generated from user-selection of the first file in the series. This was then followed by input of the system-generated metadata file, containing the number of images and the coordinates of each image. This then allowed for the conversion of coordinates into pixel locations, which allowed for mapping of the matrices. A blank matrix was first created of the coordinates for which the grid scan to be studied was represented, and then pixels in the images were simply copied over in a linear fashion to essentially copy a series of coordinate-ordered pixels into their respective positions on the final image. This was then stamped with each of the filenames per image in order to identify where each image was located and then exported as a full-sized tiff for later analysis.

9.9.2 EPBScore

Automated and unbiased measurements of neuronal features represents a known bottleneck of neuroimaging modalities. The neuroplasticity and disease lab have developed EPBscore, a MATLAB-based system that can track and measure the size (i.e. strength) of boutons along axons over time based on their intensities when compared to the axonal backbone. This has previously been validated via electron microscopy (Grillo et al., 2013).

The software accepts TIF stacks generated by PrarieView software at different time points. It then aligns the images across time points and compares the sizes of boutons over time by comparing pairs of images. The output is then a dataset consisting of relative bouton sizes and the turnover ratio for the entire axon can then be calculated as a measure of synaptic remodelling.

9.9.3 Ratiometric FRET Quantification

To extract the FRET ratios from the image stacks acquired, two different approaches were investigated to determine the optimal system, one using MATLAB and the other Volocity. Both systems were used with a workflow described in Figure 49. First, the data was extracted from the imaging system and compiled into four dimensional stacks (*xyzt*). Objects were then identified and thresholded to identify cells across the z-stacks in three dimensions. The mean intensity values for both recorded channels were then calculated and the ratio of Donor/FRET signal was used as the final FRET reading.

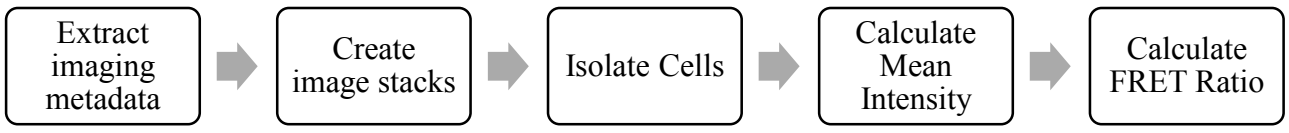


Figure 49 Workflow of Analysis Both MATLAB and Velocity suites were used to analyse data using the above workflow.

The MATLAB approach consisted of a custom written program that manually stacked the images and removed all pixels less than 30% of the average image intensity, removing the background and isolate the objects. Cells were then manually cropped across all z-stacks in a ‘cookie-cutter’ approach and the mean of each three dimensional image stack, minus the background and any over-exposed pixels, was plotted for each ime point.

The Volocity approach made use of the software's inbuilt object detection system to identify populations of cells and continued to track these objects in three dimensional space to account for cellular movement during imaging or motion artefacts caused by the constant flow of media of the sample. Mean intensities were then automatically calculated and the ratio established as in the previous method.

Both systems have advantages and disadvantages: The MATLAB software allows the user to define specific cells, as can be recognised by boundaries, whereas the Volocity system has difficulty in discerning objects with adjacent boundaries; however, Volocity is much faster than the MATLAB system due to its automatic object recognition.

Both systems were compared on identical image sets and FRET values appeared to have a higher signal to noise ratio, with improved range of samples and accuracy in the Volocity system, and so it was adopted for all analysis.

9.9.3.1 Corrected FRET Values

In order to account for spectral bleedthrough, the corrected FRET method was used from Xia and Liu (2001). This uses samples in which only the donor and only the acceptor fluorophores are expressed to establish coefficients to correct for the leakage and cross-excitement of the acceptor protein from the donor laser.

The following equation is used to calculate a corrected FRET channel ($FRET_{corr}$) for each time point:

$$FRET_{corr} = FRET - B\ (CFP) - D\ (YFP_{dir})$$

Where FRET is the ratio measured, B is measured using the donor only and recording in both channels and is calculated as FRET/donor. D is calculated as acceptor-only expressing cells being exciting first by the donor laser (IDA) and then by a laser tuned to the excitation spectrum of the acceptor (IAA) and finally IDA/IAA. YFP_{dir} is used to offset any photobleaching (if required) by using a recorded trial of excited acceptor only and then dividing the T0 value by the time point being measured.

9.9.4 FLIM analysis

FRET-FLIM results were imported into FLIMfit, a MATLAB-orientated software written by Sean Warren of the Photonics lab. The software applies the non-linear least square fitting model (Grinvald and Steinberg, 1974) to fit FLIM measurements, by minimising the χ^2 fitting parameter. Data is first input as the raw images acquired from the Beckler & Hickl TCSPC device and is then segmented based on intensity to isolate structures of interest.

An instrument response function (IRF) dataset is loaded into the system, acquired from gold nanorods on the same day as sample imaging. Finally a decay profile is fitted based on either a mono- or bi-exponential curve.

9.9.5 Calcium Imaging Analysis

A custom MATLAB program was written to first load the images acquired as a virtual stack, with the frame rate specified. A box is then drawn around the cell of interest by the user based on an average projection in order to see active neurons throughout the entire image set.

The background is then removed based on a threshold of intensity and the image stack is cropped to isolate the pixel within the region of interest. The pixels are then averaged for each frame and plotted against time.

In order to calculate an approximate interval for regular activity, a fast Fourier transform was carried out and the peak frequency indicated by the GUI output (Figure 50) for the user.

9.9.6 Statistics

Statistical tests were performed with either MATLAB, R or in Excel.

K-means clustering was performed in R using the *kmeans()* function, which takes the matrix of data, number of k-centres as cluster counts, maximum iterations and how many random stets are required. The algorithm of Hartigan and Wong (1979) was used as the default.

One-way ANOVA with Tukey post-hoc analysis was performed in MATLAB, where the FRET sensor comparison data was stored in a large cell array. This was performed with the MathWorks multiple comparison function, 'multcompare', applied to the output from an 'anova1' function as follows: *[p, mainout, dataoutput] = anova1(input); [comp, mat, handle, names] = multcompare(dataoutput, 'alpha',.01, 'ctype', 'tukey-kramer');*.

Student's t-tests were performed in both MATLAB with the 'ttest2' function and in Microscoft Excel with the 'T.TEST' function. F-tests were also carried out in Excel via 'F.TEST' functionality.

10 DISCUSSION

This project began with a selection of FRET sensors designed to monitor the activity of cAMP, a ubiquitous second messenger with critical roles in regulating synaptic plasticity, a process important for learning and memory. The use of FRET combined with multiphoton microscopy and FLIM recording permitted the readout of FRET sensors expressed deep within mammalian tissues prepared *ex vivo*.

Combined with the observations of pre-synaptic remodelling sites *in vitro*, the compartmentalisation and time course of cAMP activation could be visualised and measured.

10.1 MICROSCOPY

In order to successfully record FRET signals from cells, the appropriate imaging system was optimised for each culture and experiment. Confocal imaging provides a high degree of spatial resolution, with flexibility of varying laser lines and PMT tuning parameters, however ultimately lacks the penetration needed to delve into tissue cultures. It also provides a far higher power output, being single-photon in nature, and thus can result in not only photobleaching of fluorescent proteins, but also phototoxic damage to the sample. This was to be minimised as much as possible in neuronal cultures.

Multiphoton systems, with lower energies not only minimise photobleaching, but allow for a far greater degree of depth penetration using the far infrared spectrum. Once tissue cultures were introduced over cell monolayers in this project, 2-photon microscopy became absolutely necessary for resolving deep neurons.

As the culture format changed, so did the microscope. Cell monolayers grown onto glass are excellent for inverted systems, whereby the objective approaches from beneath the sample and imaging takes place directly through the glass and into the adhered cells. This minimises

change in refractive index, as light passes simply from coverslip-matched immersion oil and into the sample.

In tissue, however, the OSCs were not cultured onto glass but rather membranes. While experiments in 'bridging' apertures with the membrane to permit inverted viewing were attempted, the main limitation was the inability to continuously submerge the section with imaging solution or add stimulants. After visiting the lab of Professor Ryohei Yasuda (Max Planck Institute Florida), their use of upright microscopes combined with imaging chambers for sections anchored with weights emphasised the need for an upright system for experiments.

The FILM department at Imperial College London provided such a multiphoton, upright system with FLIM detector, allowing for slices to be imaged whilst submerged in a water-based imaging solution, with the appropriate dipping objective lens. For tissue cultures, this allowed extended imaging sessions of samples with adequate hydration as well as straightforward solution exchange.

In order to ascertain morphological data to measure bouton size, high-resolution, 3D scanning was required through the z-axis. Typically, FLIM recordings are only based on single optical planes due to the time constraints in imaging for scanning-based systems (systems utilising more rapid acquisition, such as the Nipkow spinning disc (Adams et al., 2003; Egner et al., 2002) system would negate this), as typically 30-60 seconds of photon collection is required to generate complete lifetime decay profiles. The coupling of multiphoton optical sectioning techniques with constant photon collection throughout the stack therefore allows for not only structural information to be collected, but also an average lifetime of three dimensional structures to be acquired simultaneously.

Drugs were applied via perfusion chamber and micro-dialysis pump. One of the imaging obstacles was the requirement for controllable fluid dynamics for rapid, linear fluid exchange. The custom insert developed and printed not only provided this, but was also capable of

allowing fast switching of samples and was straightforward to clean. With further refinement of the design and possibly with the latest advancements of 3D printing, the system could be improved. One potential issue is the inertness of the plastics. Initially ABS (Acrylonitrile Butadiene Styrene) was used due to its higher resistance to impact and warping, however later this was switched to a biodegradable plastic, PLA (polylactic acid) as it is of a more 'food-safe' variety and therefore was considered to be less reactive to the imaging solutions (in particular DMSO dilutant). In the time spent in contact with tissues (<1hr), it seems unlikely any effect would be seen *in vitro*, indeed PLA is now commonplace in medical implants (Jain, 2000).

As a portion of this project revolved around the morphological analysis of boutons, the modern techniques of super-resolution microscopy, surpassing the diffraction limit of light and providing far higher resolution images, were explored as a means of gaining greater insight into synaptic structures. Using structured illumination microscopy (SIM), whereby a grid-like pattern is projected onto the sample and the distortion of the reflected light provides structural information, morphological details were observed beyond the resolution of standard confocal microscopy, such as the individual rings of actin that make up axonal structure (Appendix, Figure 51).

However, when exploring synaptic structures, this technique did not ultimately provide more information than multiphoton imaging, and this, combined with a lack of depth penetration, led to the discontinuation of its use within the project. The future use of other super-resolved modalities that can provide even greater resolution, such as STED or STORM, may provide a higher degree of structural information of interest to combine with FRET recordings.

10.2 Fluorescent probes and FRET sensors

A selection of FRET probes were made available from the Karl Jalink lab at the start of the project in 2012 (Klarenbeek et al., 2011). These were already a stark advancement on the previous CFP-Epac-YFP sensor that was in general use. The use of an mTurquoise donor

and the Q270E mutation in the EPAC linker allowed for a far higher sensitivity and more robust signal, paramount to the detection of subtle concentration shifts in axons.

Published data from the source did imply the mTurquoise2-EPACQ270E-VenusVenus and GFP-EPAC-mCherry sensors to have highest dynamic ranges and sensitivity, however this was re-iterated to ensure they behaved optimally in neuronal cultures, a unique cell type in mammalian physiology. The reason for both to be of interest initially (as opposed to just the higher-sensitivity of the former) was the low-energy wavelengths required for a red-shifted sensor. This allows for less damage to occur during imaging, however the larger spectral gap between donor and acceptor ultimately appeared to limit its sensitivity, and given that multiphoton imaging already reduces phototoxic/bleaching effects, the blue-yellow pair resulted in the chosen sensor.

Interestingly, the lifetime values for resting cells varied between cell types. In HEK cells, the baseline was seen to be ca. 3400ps, whereas in neurons this was lower at ca. 2700ps. While technical reasons behind this could lie in the different microscopes used with different light sources, this could also suggest a higher concentration of cAMP in resting neurons than in HEK cell. As the neuron is undergoing constant re-shaping and extensive electrical activity, this may upregulate intracellular cascades, elevating cAMP, a messenger relatively high in cell signalling processes. Another explanation could be the sensitivity of neurons to changes in environment and, despite being given time to equilibrate at the imaging station, may have induced cellular activity pathways, again being driven by cAMP synthesis.

As this baseline FRET-FLIM level can alter, depending on resting conditions of different cell types, there is a theoretical maximum FRET change that can be measured for a particular cell type, i.e. the initial lifetime cannot go below that for the resting state of the cell. This could therefore reduce the effective dynamic range with these sensors, and so higher level changes may plateau off due to saturation of the sensor in either its bound or unbound state.

The use of mTurquoise2 as the principal donor fluorophore in this project reflects its prevalence in FLIM studies, being one of the most popular fluorophores to use. As with all fluorescent proteins, there is some level of sensitivity to pH and temperature change (Ishii et al., 2007). While mTurquoise2 is known to be stable and resistant to the environmental differences (Goedhart et al., 2012), it is possible that the lifetime-FRET values could be altered if localised, pH-differing microenvironments were present at the presynaptic boutons. Indeed, the presence of acid-sensing ion channels (ASICs) has been found in neurons for over 30 years (Gruol et al., 1980; Krishtal and Pidoplichko, 1981), with evidence of H^+-gated currents playing a role in synaptic plasticity (Cooke and Lilley, 2002). This led to the experiment (Figure 46) being repeated with the donor only, thus ruling out any pH-induced changes as differences of lifetime at the boutons even without FRET activity.

10.3 STIMULATION

To establish dynamic ranges of sensors, the adenylate cyclase activator, forskolin, was used extensively to invoke an increase in cytoplasmic cAMP. There are, however, a range of drugs commonly used in cAMP manipulation. MDL-12,300A is a popular adenylate cyclase inhibitor, whilst IBMX, a phosphodiesterase inhibitor, prevents the degradation of cAMP. Klarenbeek et al. (2011) made use of IBMX combined with forskolin to produce a maximal response by completely saturating intracellular cAMP in HEK cells. As neurons are particularly prone to chemical imbalance-induced toxicity, such a strong stimulus may have induced uncharacteristic responses in cells. MDL-12,330A was used in HEK cells to provoke a gradual cAMP decrease (see Appendix, Figure 52), however as the aim was to determine the highest sensitivity to positive stimulation, forskolin alone was used. A number of groups have made use of MDL with a membrane-permeable cAMP analog (or rather, EPAC-specific activator), 8-Bromoadenosine 3′,5′-cyclic monophosphate (Kogan et al., 1992; Rossato et al., 2009; Yin et al., 2006). By simultaneously blocking endogenous cAMP production with MDL and submersing cells in known concentrations of 8-Br-cAMP, more precise control of cytoplasmic

cAMP concentration is obtained, potentially allowing for a direct correlation of known cAMP levels and FRET readout (Boerner et al., 2011). This was attempted with HEK cells in this project, and while it did produce a slight increase in cAMP concentration as evaluated by ratiometric FRET measurements, it proved ineffective against neuronal cell types in tissue. As it has been reported to show increased Epac activity in primary neuronal cultures by other groups (Freund and Palmer, 1996; Ivins et al., 2004), this is most likely due to a lack of penetration of small concentrations of the analog, and thus was not deemed useful in OSC experiments.

Alternative stimulation was considered, drawing on global depolarisation of slices with chemicals such as potassium chloride; as well as electrical stimulation with trains delivered as local fields across the tissue. These approaches are relatively acute however, and so the sustained changes that are required for the relatively slow temporal resolution of the FLIM-FRET system (ca. 60 seconds) were better produced with perfusion of forskolin.

Ultimately, as the project was primarily focussed on endogenous cAMP activity at synaptic sites, stimulation was not required in OSC experiments once the sensor, imaging system and basal synaptic turnover rates had been optimised.

10.4 Morphology and Bouton Size

Measurement and recording of synaptic size and intensity has been shown to be strongly correlated to synaptic strength (Cheetham et al., 2014; Grillo et al., 2013; Pierce and Lewin, 1994). By utilising high-resolution, three dimensional scanning of axonal processes, volumetric analysis of boutons can indicate the strengthening, weakening and overall turnover of synapses and neuroplasticity in general. Using EPBscore software, synaptic boutons are routinely measured in the current lab, being tracked over days, weeks and months in both physiological and pathological conditions (Canty et al., 2013a; Canty et al., 2013b; De Paola et al., 2006; Grillo et al., 2013; Song et al., 2016). The software overcomes a major ‘bottleneck’ of synaptic investigations, allowing for a semi-automated method for accurately detecting

subtle changes in synaptic size and therefore strength. Previously, manual measurements would take days of tracing processes by hand, sampling each individual point. This also introduces a human bias component, whereby each dataset can be interpreted slightly differently depending on the individual analysing it. Through the use of automated software, every series of images is objectively quantified, always to the same set of parameters and thus provides a reliable and reproducible comparison between conditions (Song et al., 2015).

Studies of EPBs on an hourly time scale are scarce, given that the changes occurring over a period of several days are far more pronounced, namely in the overall turnover of synapses, with some degree of bouton elimination as well as formation. This project witnessed only those changes happening within the 90 minute imaging window, and without the external stimulation of learning a novel task or sensory manipulation possible *in vivo*. This suggests that the findings reflect the activity of a basal, intrinsic turnover of synapses, as opposed to the marked response to the acquisition of new memories. However, it is the correlation of synaptic strengthening with cAMP activity that provides insight into the requirements for bouton enlargement, shown to underly LTP and long-term memory.

10.5 cAMP ACTIVITY IS UPREGULATED AT SITES OF PRE-SYNAPTIC ENLARGEMENT

When synapses undergo LTP and a strengthening of their connection between adjoining cells, a large number of intracellular signalling cascades occur on both sides of the synapse. At the pre-synaptic site, the axonal bouton, probability of neurotransmitter release increases as the synapse strengthens. This process involves the packaging of transmitters into vesicles and then the entire docking cycle, involving a plethora of signalling cascades from the binding and recycling of vesicles at the membrane through to the exocytosis into the synaptic cleft.

It has long been known that cAMP plays a crucial role in LTP, primarily via the PKA-dependent pathways (Bolshakov et al., 1997; Chavis et al., 1998; Frey et al., 1993a; Ma et al., 1999; Woo et al., 2003), and also Epac-dependent cascades (Ma et al., 2009; Ostroveanu et al., 2010;

Poser and Storm, 2001). In order to establish the links between cAMP and LTP, most of these studies make use of inhibitors and activators of cAMP itself or its subsidiary signalling proteins, blocking and stimulating individual pathways and observing the end effect on either animal behaviour or neuronal morphology. Whilst this does provide strong evidence for the necessity of cAMP to drive synaptic changes, it lacks the spatial and temporal resolution required to fully comprehend where, when and how it exerts its effects.

After developing the appropriate system, this project has, for the first time, directly observed cAMP dynamics during synaptic size changes on a rapid time scale with strict compartmentalisation.

This suggests the potential requirement for cAMP directly at the site of the presynaptic bouton in order for a strengthening to take place, as opposed to somal activity driving secondary synaptic changes via transcription of transportable proteins. The spatial segregation of cAMP has been noted by several groups (Di Benedetto et al., 2008; Kotaleski and Blackwell, 2010; Steinberg and Brunton, 2001), and the potential mechanisms that could govern this are outlined in Section 3.5. Initially, given cAMP's solubility and high diffusion coefficient, it was believed that it would diffuse freely throughout the cytosol, however, in the last 40 years, a number of groups reported some dregree of confined cAMP activity, especially in cardiac myocytes. Indeed, in an elegant study whereby two halves of a single myoctye were supplied with different drugs, it was seen that cAMP simply could not produce a uniform response throughout single, exciteable cells (Jurevicius and Fischmeister, 1996). Since then, FRET has been used to visualise such compartmentalisation in a more direct manner, observing cAMP concentrations in neurons in aplysia (Bacskai et al., 1993), *xenopus* (Gorbunova and Spitzer, 2002) and lobster (Hempel et al., 1996). These studies made use of the early generations of cAMP-FRET sensor, with relatively poor signal-to-noise ratio, only capable of recording wide-ranging signal in large cellular sructures. However, this was sufficient to determine that endogenous cAMP does form local microdomains. Interestingly, direct injection of cAMP into cells expressing these sensors apparently overcomes the localising machinery, readily

diffusing throughout the cytosol, indicating a maximum concentration that can be retained at specific sites (Rich et al., 2001b). Hempel et al. (1996) noted a gradient of cAMP concentration, with cAMP synthesis at stimulated sites at the neuronal periphery followed by a diffusion towards the soma, theoretically to induce genetic transcription for the long-lasting changes required to store longterm memory. Improvements in cAMP sensors has allowed for groups to observe these cAMP gradients and rates of diffusion in mammals and at higher spatial resolutions, further confirming this direction of cAMP activity: from stimulated process to neuronal soma on a timescale of several hundred milliseconds (Nikolaev et al., 2004).

This background supports the findings of this project, whereby cAMP synthesis appears upregulated at synaptic sites undergoing enlargement/strengthening. A key difference in this study and those previously mentioned, is the absense of a direct stimulus to provoke adenylyl cyclase activity. This would imply that unlike previous work showing how an artificially induced cAMP transient would propagate throughout the axon or dendrite, endogenous, sporadic strengthening of boutons also invokes a natural production of cAMP at the synapse. With a longer imaging window with perhaps even more sensitive sensors, it may even be possible to visualise the unstimulated establishment of a cAMP gradient from synapse to soma *in vitro*; or perhaps more interestingly, with an enivornmentally-stimulated animal *in vivo*.

10.6 cAMP IN DISEASE

As detailed in section 3.3, a number of neuropsychiatric disorders and diseases present impairments at the synaptic level. As cAMP is recruited in such a wide range of cellular signalling processes, its involvement in such disorders and its subsequent targeting is of logical interest to the field.

Phosphodiesterases are a family of enzymes that degrade the phosphodiester bond in cAMP, depleting it from the cell and consequently mediating cAMP-dependent signalling pathways. Phosphodiesterase inhibitors (including caffeine) have been desirable pharmaceutical agents for several disorders that can be attributed to cyclic nucleotide

dysfunction, including asthma, inflammatory disorders and congestive heart failure (Boswell-Smith et al., 2006; Hanifin et al., 1996; Weiss and Hait, 1977). Of particular interest is their use in the potential treatment of neurological disorders. As it is now well established that cAMP plays such a vital role in the formation of long term memories, several studies have investigated the use of these phosphodiesterase inhibitors as treatments potential for Alzheimer's Disease (Garcia-Osta et al., 2012), as well as improving cognitive function in general (Richter et al., 2013). These pharmaceutical pathways revolve around the CREB pathway of gene expression, activated via cAMP, and encoding for the proteins required for memory formation. Other neurological disorders including Huntington's (Fusco and Giampa, 2015) and depression (Ding et al., 2014; Liebenberg et al., 2010; Renau, 2004) have also been extensively studied, with approved and prescribed inhibitors now commonplace for the treatment of depression.

This research into cAMP pathways, especially in relation to memory impairment and dementia is important for our understanding of how such diseases can be treated. By fully understanding where and how cAMP exerts its effects on a synaptic level, new targets and modulators can be synthesised, with minimal side effects elsewhere in the body.

11 CONCLUSIONS AND FUTURE WORK

11.1 SUMMARY OF FINDINGS

The use of FRET combined with FLIM in a multiphoton system provides an exceptionally powerful tool for investigation of sub-cellular networks and pathways. This project has aimed to combine this with the study of neuroanatomy and the role of cAMP in synaptic plasticity, an important cellular mechanism underlying learning and memory in the mammalian brain.

The imaging system required to achieve this involved extensive testing and optimisation, resulting in the selection of an optimal sensor, transfected via the ideal method into a cultured medium that would allow the best compromise of imaging access and manipulation, while retaining Physiological levels of synaptic turnover and size changes.

This concluded in the use of an mTurquoise2-EPAC^{Q270E}-VenusVenus FRET sensor biolistically inserted into cortical neurons in organotypic slice cultures being imaging via 3D-printed perfusion chamber on an upright, multiphoton FLIM imaging setup.

cAMP is an ubiquitous secondary messenger within many mammalian tissues, and lies relatively early in cell signalling pathways, being directly synthesised at the cell membrane upon GPCR (G-protein coupled receptor) activation. At the point of contact between neighbouring neurons, synaptic connections are known to be formed to allow for information to travel between them, comprising the massive neural networks that allow for the storage of information and higher level processing. It has long been established that cAMP plays a conductory role in the strengthening and weakening of synapses, the basis of long term potentiation and depression respectively, as proposed in the Hebbian theory of learning and memory retention. While this role has been studied extensively in whole brain preparations and through the use of knockout and overexpression models, cAMP's level of compartmentalisation within the synapse has only been hypothesised.

Through the use of the novel imaging methods introduced in this project, micro-environments of cAMP concentration were visualised at the sites of synapses along the axons of neurons. By coupling this reading with the minute structural changes that occur in the ever-rewiring brain, a correlation was observed between higher levels of cAMP at synapses undergoing a strengthening of connection: the very basis of long-term memory formation.

This provides insight into the localised and targeted nature of cAMP, providing the possibility for diagnosis and treatment research into the underlying synaptic impairments at the root of a plethora of neuropsychiatric disorders including dementia, depression, schizophrenia and autistic spectrum disorders.

11.2 FUTURE WORK

This project involved a great deal of method development and optimisation in order to bring a powerful imaging tool into a neurobiology field. The use of EPAC sensors to study cAMP dynamics *in vitro* is just one such avenue of research that can be carried out on this system. Other FRET sensors, binding a plethora of signalling molecules and proteins could be transfected into neuronal slices for the study of all manner of processes underlying cell morphology, activity and development.

During imaging sessions, many different morphological structures were observed, including axon growth cones, terminal boutons, dendritic spines, filopodia and somatic changes over time; all of which carry vital roles in the nervous system and are still in need of further study. The ability to achieve a direct readout of sensors clustered within individual compartments that can reflect very specific concentration fluctuations on a timescale of seconds to minutes is a powerful tool in neuroscience. The neuroplasticity and disease lab have perfected the technique of cranial window implantation accompanied with either viral transduction or *in utero* electroporation of DNA. This could result in a system allowing for the precise recordings of FRET sensors via 2p-FLIM *in vivo*, a system that could provide enormous potential in

neurological discovery. The added *in vivo* dimension would also allow for behavioural studies to be combined with measurement of neuronal changes in molecular dynamics, allowing a more endogenous stimulation protocol (such as whisker stimulation) than drug-induced changes.

Furthermore, as mentioned above, some super-resolution microscopy techniques were explored as an avenue for greater yield of morphological information. While FRET-FLIM has yet to be recorded with such a system (mostly due to the challenge of live cell imaging and simultaneous, multi-channel imaging and spatial distribution for ratiometric FRET), there are numerous groups combining, or overlaying, such information with super-resolved images to provide some level of functional data with sub-micron structures (Grecco and Verveer, 2011).

The recording from multiple sensors simultaneously is also an option becoming recently more viable (Grant et al., 2008; Kumar et al., 2011). So called 'multiplexing' requires the use of fast optics and rapidly tuneable lasers, making it difficult for multiphoton systems without several infrared pulsing lasers and FLIM capture systems. If implemented, this would allow for the readout of multiple sensors for interaction studies between proteins. In this project, such a system would most likely have been combined with calcium imaging (see Appendix 13.1). This would allow for further insight into the neurons displaying the highest changes in cAMP dynamics on a level of calcium activity, a well-established driver of LTP in neuronal transmission (Blitzer et al., 1998a; Wong et al., 1999).

11.3 Closing Remarks

Over the course of this PhD project, scientific method was extensively applied to the objective optimisation of each stage of development. Repeated measures and unbiased quantification allowed for a sensitive, reproducible and efficient system to be developed for the imaging of FRET sensors in deep tissues.

As the Neuroplasticity and Disease lab now possess these established tools, future experiments can commence, thoroughly and comprehensively investigating the chemical computers behind each neuron, shedding new light on the pathways underlying learning and memory and neurological dysfunction.

12 REFERENCES

Abel, T., Nguyen, P.V., Barad, M., Deuel, T.A., Kandel, E.R., and Bourtchouladze, R. (1997). Genetic demonstration of a role for PKA in the late phase of LTP and in hippocampus-based long-term memory. Cell *88*, 615-626.

Adams, M.C., Salmon, W.C., Gupton, S.L., Cohan, C.S., Wittmann, T., Prigozhina, N., and Waterman-Storer, C.M. (2003). A high-speed multispectral spinning-disk confocal microscope system for fluorescent speckle microscopy of living cells. Methods *29*, 29-41.

Adams, S.R., Harootunian, A.T., Buechler, Y.J., Taylor, S.S., and Tsien, R.Y. (1991). Fluorescence Ratio Imaging of Cyclic-Amp in Single Cells. Nature *349*, 694-697.

Ahmari, S.E., and Smith, S.J. (2002). Knowing a nascent synapse when you see it. Neuron *34*, 333-336.

Akamatsu, W., Okano, H.J., Osumi, N., Inoue, T., Nakamura, S., Sakakibara, S., Miura, M., Matsuo, N., Darnell, R.B., and Okano, H. (1999). Mammalian ELAV-like neuronal RNA-binding proteins HuB and HuC promote neuronal development in both the central and the peripheral nervous systems. Proc Natl Acad Sci U S A *96*, 9885-9890.

Alger, B.E., and Teyler, T.J. (1976). Long-term and short-term plasticity in the CA1, CA3, and dentate regions of the rat hippocampal slice. Brain research *110*, 463-480.

Ascher, P., and Nowak, L. (1986). A patch-clamp study of excitatory amino acid activated channels. Advances in experimental medicine and biology *203*, 507-511.

Ashkenazi, A., Yuan, J.Y., and Wells, J.A. (2014). METHODS IN ENZYMOLOGY Regulated Cell Death Part A: Apoptotic Mechanisms VOLUME FIVE HUNDRED AND FORTY FOUR PREFACE. Regulated Cell Death Pt A: Apoptotic Mechanisms *544*, Xv-Xv.

Atwood, B.K., Lovinger, D.M., and Mathur, B.N. (2014). Presynaptic long-term depression mediated by Gi/o-coupled receptors. Trends Neurosci *37*, 663-673.

Bacskai, B.J., Hochner, B., Mahautsmith, M., Adams, S.R., Kaang, B.K., Kandel, E.R., and Tsien, R.Y. (1993). Spatially Resolved Dynamics of Camp and Protein Kinase-a Subunits in Aplysia Sensory Neurons. Science *260*, 222-226.

Bailey, C.H., and Kandel, E.R. (1993). Structural-Changes Accompanying Memory Storage. Annu Rev Physiol *55*, 397-426.

Bailey, C.P., Nicholls, R.E., Zhang, X.L., Zhou, Z.Y., Muller, W., Kandel, E.R., and Stanton, P.K. (2008). Galpha(i2) inhibition of adenylate cyclase regulates presynaptic activity and unmasks cGMP-dependent long-term depression at Schaffer collateral-CA1 hippocampal synapses. Learning & memory *15*, 261-270.

Baillie, G.S., Scott, J.D., and Houslay, M.D. (2005). Compartmentalisation of phosphodiesterases and protein kinase A: opposites attract. Febs Lett *579*, 3264-3270.

Banker, G.A., and Cowan, W.M. (1979). Further Observations on Hippocampal-Neurons in Dispersed Cell-Culture. J Comp Neurol *187*, 469-493.

Bastrikova, N., Gardner, G.A., Reece, J.M., Jeromin, A., and Dudek, S.M. (2008). Synapse elimination accompanies functional plasticity in hippocampal neurons. Proc Natl Acad Sci U S A *105*, 3123-3127.

Bayes, A., van de Lagemaat, L.N., Collins, M.O., Croning, M.D.R., Whittle, I.R., Choudhary, J.S., and Grant, S.G.N. (2011). Characterization of the proteome, diseases and evolution of the human postsynaptic density. Nature Neuroscience *14*, 19-21.

Becker, W., Bergmann, A., Hink, M.A., Konig, K., Benndorf, K., and Biskup, C. (2004). Fluorescence lifetime imaging by time-correlated single-photon counting. Microsc Res Techniq *63*, 58-66.

Bennett, M.K., Calakos, N., and Scheller, R.H. (1992). Syntaxin - a Synaptic Protein Implicated in Docking of Synaptic Vesicles at Presynaptic Active Zones. Science *257*, 255-259.

Bliss, T.V., and Collingridge, G.L. (1993). A synaptic model of memory: long-term potentiation in the hippocampus. Nature *361*, 31-39.

Bliss, T.V., and Gardner-Medwin, A.R. (1973). Long-lasting potentiation of synaptic transmission in the dentate area of the unanaestetized rabbit following stimulation of the perforant path. The Journal of physiology *232*, 357-374.

Bliss, T.V., and Lomo, T. (1973). Long-lasting potentiation of synaptic transmission in the dentate area of the anaesthetized rabbit following stimulation of the perforant path. The Journal of physiology *232*, 331-356.

Blitzer, R.D., Conner, J.H., Brown, G.P., Wong, T., Shenolikar, S., Iyengar, R., and Landau, E.M. (1998a). Gating of CaMKII by cAMP-regulated protein phosphatase activity during LTP. Science *280*, 1940-1943.

Blitzer, R.D., Connor, J.H., Brown, G.P., Wong, T., Shenolikar, S., Iyengar, R., and Landau, E.M. (1998b). Gating of CaMKII by cAMP-regulated protein phosphatase activity during LTP. Science *280*, 1940-1942.

Boerner, S., Schwede, F., Schlipp, A., Berisha, F., Calebiro, D., Lohse, M.J., and Nikolaev, V.O. (2011). FRET measurements of intracellular cAMP concentrations and cAMP analog permeability in intact cells. Nature Protocols *6*.

Bolshakov, V.Y., Golan, H., Kandel, E.R., and Siegelbaum, S.A. (1997). Recruitment of new sites of synaptic transmission during the cAMP-dependent late phase of LTP at CA3-CA1 synapses in the hippocampus. Neuron *19*, 635-651.

Bonci, A., and Williams, J.T. (1996). A common mechanism mediates long-term changes in synaptic transmission after chronic cocaine and morphine. Neuron *16*, 631-639.

Bonhoeffer, T., Staiger, V., and Aertsen, A. (1989). Synaptic plasticity in rat hippocampal slice cultures: local "Hebbian" conjunction of pre- and postsynaptic stimulation leads to distributed synaptic enhancement. Proc Natl Acad Sci U S A *86*, 8113-8117.

Boswell-Smith, V., Spina, D., Oxford, A.W., Comer, M.B., Seeds, E.A., and Page, C.P. (2006). The pharmacology of two novel long-acting phosphodiesterase 3/4 inhibitors, RPL554 [9,10-dimethoxy-2(2,4,6-trimethylphenylimino)-3-(N-carbamoyl-2-aminoethyl)-3,4,6,7-tetrahydro-2H-pyrimido[6,1-a]isoquinolin-4-one] and RPL565 [6,7-dihydro-2-(2,6-diisopropylphenoxy)-9,10-dimethoxy-4H-pyrimido[6,1-a]isoquinolin-4-one]. Journal of Pharmacology and Experimental Therapeutics *318*, 840-848.

Brooker, G., Harper, J.F., Terasaki, W.L., and Moylan, R.D. (1979). Radioimmunoassay of cyclic AMP and cyclic GMP. Advances in cyclic nucleotide research *10*, 1-33.

Brose, N., O'Connor, V., and Skehel, P. (2010). Synaptopathy: dysfunction of synaptic function? Biochemical Society transactions *38*, 443-444.

Brunelli, M., Castellucci, V., and Kandel, E.R. (1976). Synaptic facilitation and behavioral sensitization in Aplysia: possible role of serotonin and cyclic AMP. Science *194*, 1178-1181.

Burre, J., Sharma, M., Tsetsenis, T., Buchman, V., Etherton, M.R., and Sudhof, T.C. (2010). alpha-Synuclein Promotes SNARE-Complex Assembly in Vivo and in Vitro. Science *329*, 1663-1667.

Canty, A.J., Huang, L., Jackson, J., Maco, B., Knott, G., Little, G., and De Paola, V. (2013a). In-vivo single neuron axotomy triggers axon regeneration to restore synaptic density in specific cortical circuits.

Canty, A.J., Teles-Grilo Ruivo, L., Nesarajah, C., Jackson, J.S., Little, G., Song, S., and De Paola, V. (2013b). Synaptic elimination and protection after minimal injury depend on cell type and their pre-lesion structural dynamics in the adult cerebral cortex. Journal of Neuroscience.

Carrel, A. (1923). A Method for the Physiological Study of Tissues in Vitro. The Journal of experimental medicine *38*, 407-418.

Carroll, R.C., Lissin, D.V., von Zastrow, M., Nicoll, R.A., and Malenka, R.C. (1999). Rapid redistribution of glutamate receptors contributes to long-term depression in hippocampal cultures. Nat Neurosci *2*, 454-460.

Catterall, W.A., and Few, A.P. (2008). Calcium channel regulation and presynaptic plasticity. Neuron *59*, 882-901.

Chavis, P., Mollard, P., Bockaert, J., and Manzoni, O. (1998). Visualization of cyclic AMP-regulated presynaptic activity at cerebellar granule cells. Neuron *20*, 773-781.

Cheetham, C.E.J., Barnes, S.J., Albieri, G., Knott, G.W., and Finnerty, G.T. (2014). Pansynaptic Enlargement at Adult Cortical Connections Strengthened by Experience. Cereb Cortex *24*, 521-531.

Chen, C.F., and Regehr, W.G. (1997). The mechanism of cAMP-mediated enhancement at a cerebellar synapse. Journal of Neuroscience *17*, 8687-8694.

Chen, H., Puhl, H.L., 3rd, Koushik, S.V., Vogel, S.S., and Ikeda, S.R. (2006). Measurement of FRET efficiency and ratio of donor to acceptor concentration in living cells. Biophysical journal *91*, L39-41.

Chen, T.W., Wardill, T.J., Sun, Y., Pulver, S.R., Renninger, S.L., Baohan, A., Schreiter, E.R., Kerr, R.A., Orger, M.B., Jayaraman, V.*, et al.* (2013). Ultrasensitive fluorescent proteins for imaging neuronal activity. Nature *499*, 295-300.

Chen, Y., and Sabatini, B.L. (2012). Signaling in dendritic spines and spine microdomains. Current Opinion in Neurobiology *22*, 389-396.

Choi, J., Ko, J., Park, E., Lee, J.R., Yoon, J., Lim, S., and Kim, E. (2002). Phosphorylation of stargazin by protein kinase A regulates its interaction with PSD-95. The Journal of biological chemistry *277*, 12359-12363.

Collingridge, G.L., Kehl, S.J., and McLennan, H. (1983). Excitatory amino acids in synaptic transmission in the Schaffer collateral-commissural pathway of the rat hippocampus. The Journal of physiology *334*, 33-46.

Cooke, S.F., and Lilley, S.J. (2002). Acidity at the synapse: pH influences plasticity and memory. Trends Neurosci *25*, 446-447.

Costantini, L.M., Fossati, M., Francolini, M., and Snapp, E.L. (2012). Assessing the tendency of fluorescent proteins to oligomerize under physiologic conditions. Traffic *13*, 643-649.

Costero, I., and Pomerat, C.M. (1951). Cultivation of neurons from the adult human cerebral and cerebellar cortes. The American journal of anatomy *89*, 405-467.

Dalby, B., Cates, S., Harris, A., Ohki, E.C., Tilkins, M.L., Price, P.J., and Ciccarone, V.C. (2004). Advanced transfection with Lipofectamine 2000 reagent: primary neurons, siRNA, and high-throughput applications. Methods *33*, 95-103.

Dao, K.K., Teigen, K., Kopperud, R., Hodneland, E., Schwede, F., Christensen, A.E., Martinez, A., and Dskeland, S.O. (2006). Epac1 and cAMP-dependent protein kinase holoenzyme have similar cAMP affinity, but their cAMP domains have distinct structural features and cyclic nucleotide recognition. Journal of Biological Chemistry *281*, 21500-21511.

Davies, S.N., Lester, R.A., Reymann, K.G., and Collingridge, G.L. (1989). Temporally distinct pre- and post-synaptic mechanisms maintain long-term potentiation. Nature *338*, 500-503.

De Paola, V., Holtmaat, A., Knott, G., Song, S., Wilbrecht, L., Caroni, P., and Svoboda, K. (2006). Cell type-specific structural plasticity of axonal branches and boutons in the adult neocortex. Neuron *49*, 861-875.

de Rooij, J., Zwartkruis, F.J.T., Verheijen, M.H.G., Cool, R.H., Nijman, S.M.B., Wittinghofer, A., and Bos, J.L. (1998). Epac is a Rap1 guanine-nucleotide-exchange factor directly activated by cyclic AMP. Nature *396*.

Debanne, D., Gahwiler, B.H., and Thompson, S.M. (1998). Long-term synaptic plasticity between pairs of individual CA3 pyramidal cells in rat hippocampal slice cultures. J Physiol-London *507*, 237-247.

Debanne, D., Guerineau, N.C., Gahwiler, B.H., and Thompson, S.M. (1995). Physiology and Pharmacology of Unitary Synaptic Connections between Pairs of Cells in Areas Ca3 and Ca1 of Rat Hippocampal Slice Cultures. J Neurophysiol *73*, 1282-1294.

Degtyar, V., Hafez, I.M., Bray, C., and Zucker, R.S. (2013). Dance of the SNAREs: assembly and rearrangements detected with FRET at neuronal synapses. The Journal of neuroscience : the official journal of the Society for Neuroscience *33*, 5507-5523.

Di Benedetto, G., Zoccarato, A., Lissandron, V., Terrin, A., Li, X., Houslay, M.D., Baillie, G.S., and Zaccolo, M. (2008). Protein kinase A type I and type II define distinct intracellular signaling compartments. Circulation research *103*, 836-844.

Ding, L., Zhang, C., Masood, A., Li, J., Sun, J., Nadeem, A., Zhang, H.T., O'Donnell, J.M., and Xu, Y. (2014). Protective effects of phosphodiesterase 2 inhibitor on depression- and anxiety-like behaviors: involvement of antioxidant and anti-apoptotic mechanisms. Behavioural brain research *268*, 150-158.

DiPilato, L.M., Cheng, X., and Zhang, J. (2004). Fluorescent indicators of cAMP and Epac activation reveal differential dynamics of cAMP signaling within discrete subcellular compartments. Proc Natl Acad Sci U S A *101*, 16513-16518.

Doyere, V., and Laroche, S. (1992). Linear relationship between the maintenance of hippocampal long-term potentiation and retention of an associative memory. Hippocampus *2*, 39-48.

Duan, D., Yue, Y., and Engelhardt, J.F. (2001). Expanding AAV packaging capacity with trans-splicing or overlapping vectors: a quantitative comparison. Molecular therapy : the journal of the American Society of Gene Therapy *4*, 383-391.

Egner, A., Andresen, V., and Hell, S.W. (2002). Comparison of the axial resolution of practical Nipkow-disk confocal fluorescence microscopy with that of multifocal multiphoton microscopy: theory and experiment. J Microsc-Oxford *206*, 24-32.

Ehrengruber, M.U., Hennou, S., Bueler, H., Naim, H.Y., Deglon, N., and Lundstrom, K. (2001). Gene transfer into neurons from hippocampal slices: comparison of recombinant Semliki Forest Virus, adenovirus, adeno-associated virus, lentivirus, and measles virus. Molecular and cellular neurosciences *17*, 855-871.

Ehrengruber, M.U., Lanzrein, M., Xu, Y., Jasek, M.C., Kantor, D.B., Schuman, E.M., Lester, H.A., and Davidson, N. (1998). Recombinant adenovirus-mediated expression in nervous system of genes coding for ion channels and other molecules involved in synaptic function. Methods in enzymology *293*, 483-503.

Elias, G.M., and Nicoll, R.A. (2007). Synaptic trafficking of glutamate receptors by MAGUK scaffolding proteins. Trends Cell Biol *17*, 343-352.

Esteban, J.A., Shi, S.H., Wilson, C., Nuriya, M., Huganir, R.L., and Malinow, R. (2003). PKA phosphorylation of AMPA receptor subunits controls synaptic trafficking underlying plasticity. Nat Neurosci *6*, 136-143.

Feng, G., Mellor, R.H., Bernstein, M., Keller-Peck, C., Nguyen, Q.T., Wallace, M., Nerbonne, J.M., Lichtman, J.W., and Sanes, J.R. (2000). Imaging neuronal subsets in transgenic mice expressing multiple spectral variants of GFP. Neuron *28*, 41-51.

Fioravante, D., and Regehr, W.G. (2011). Short-term forms of presynaptic plasticity. Current Opinion in Neurobiology *21*, 269-274.

Förster, T. (1948). Intermolecular energy migration and fluorescence. Ann Physik (Leipzig) *2*, 55–75.

Foust, K.D., Nurre, E., Montgomery, C.L., Hernandez, A., Chan, C.M., and Kaspar, B.K. (2009). Intravascular AAV9 preferentially targets neonatal neurons and adult astrocytes. Nature biotechnology *27*, 59-65.

Fox, K., and Wong, R.O.L. (2005). A comparison of experience-dependent plasticity in the visual and somatosensory systems. Neuron *48*, 465-477.

Freund, R.K., and Palmer, M.R. (1996). 8-Bromo-cAMP mimics beta-adrenergic sensitization of GABA responses to ethanol in cerebellar Purkinje neurons in vivo. Alcoholism, clinical and experimental research *20*, 408-412.

Frey, U., Huang, Y.Y., and Kandel, E.R. (1993a). EFFECTS OF CAMP SIMULATE A LATE-STAGE OF LTP IN HIPPOCAMPAL CA1 NEURONS. Science *260*.

Frey, U., Huang, Y.Y., and Kandel, E.R. (1993b). Effects of cAMP simulate a late stage of LTP in hippocampal CA1 neurons. Science *260*, 1661-1664.

Friedmann, T., and Roblin, R. (1972). Gene therapy for human genetic disease? Science *175*, 949-955.

Fusco, F.R., and Giampa, C. (2015). Phosphodiesterases as Therapeutic Targets for Huntington's Disease. Curr Pharm Design *21*, 365-377.

Gao, T., Yatani, A., Dell'Acqua, M.L., Sako, H., Green, S.A., Dascal, N., Scott, J.D., and Hosey, M.M. (1997). cAMP-dependent regulation of cardiac L-type Ca2+ channels requires membrane targeting of PKA and phosphorylation of channel subunits. Neuron *19*, 185-196.

Garcia-Osta, A., Cuadrado-Tejedor, M., Garcia-Barroso, C., Oyarzabal, J., and Franco, R. (2012). Phosphodiesterases as Therapeutic Targets for Alzheimer's Disease. Acs Chem Neurosci *3*, 832-844.

Garcia-Reitbock, P., Anichtchik, O., Bellucci, A., Iovino, M., Ballini, C., Fineberg, E., Ghetti, B., Della Corte, L., Spano, P., Tofaris, G.K.*, et al.* (2010). SNARE protein redistribution and synaptic failure in a transgenic mouse model of Parkinson's disease. Brain *133*, 2032-2044.

Garner, C.C., Zhai, R.G., Gundelfinger, E.D., and Ziv, N.E. (2002). Molecular mechanisms of CNS synaptogenesis. Trends Neurosci *25*, 243-251.

Gekel, I., and Neher, E. (2008). Application of an Epac activator enhances neurotransmitter release at excitatory central synapses. Journal of Neuroscience *28*, 7991-8002.

Gilmore, E.C., and Herrup, K. (1997). Cortical development: Layers of complexity. Curr Biol *7*, R231-R234.

Goedhart, J., van Weeren, L., Hink, M.A., Vischer, N.O., Jalink, K., and Gadella, T.W., Jr. (2010). Bright cyan fluorescent protein variants identified by fluorescence lifetime screening. Nat Methods *7*, 137-139.

Goedhart, J., von Stetten, D., Noirclerc-Savoye, M., Lelimousin, M., Joosen, L., Hink, M.A., van Weeren, L., Gadella, T.W.J., and Royant, A. (2012). Structure-guided evolution of cyan fluorescent proteins towards a quantum yield of 93%. Nat Commun *3*.

Gogolla, N., Galimberti, I., DePaola, V., and Caroni, P. (2006a). Long-term live imaging of neuronal circuits in organotypic hippocampal slice cultures. Nature Protocols *1*, 1223-1226.

Gogolla, N., Galimberti, I., DePaola, V., and Caroni, P. (2006b). Preparation of organotypic hippocampal slice cultures for long-term live imaging. Nature Protocols *1*, 1165-1171.

Goldsmith, B.A., and Abrams, T.W. (1992). cAMP modulates multiple K+ currents, increasing spike duration and excitability in Aplysia sensory neurons. Proc Natl Acad Sci U S A *89*, 11481-11485.

Gorbunova, Y.V., and Spitzer, N.C. (2002). Dynamic interactions of cyclic AMP transients and spontaneous Ca2+ spikes. Nature *418*, 93-96.

Grant, D.M., Zhang, W., McGhee, E.J., Bunney, T.D., Talbot, C.B., Kumar, S., Munro, I., Dunsby, C., Neil, M.A., Katan, M.*, et al.* (2008). Multiplexed FRET to image multiple signaling events in live cells. Biophysical journal *95*, L69-71.

Grecco, H.E., and Verveer, P.J. (2011). FRET in cell biology: still shining in the age of super-resolution? Chemphyschem : a European journal of chemical physics and physical chemistry *12*, 484-490.

Greengard, P., Valtorta, F., Czernik, A.J., and Benfenati, F. (1993). Synaptic vesicle phosphoproteins and regulation of synaptic function. Science *259*, 780-785.

Greenough, W.T., and Bailey, C.H. (1988). The Anatomy of a Memory - Convergence of Results across a Diversity of Tests. Trends Neurosci *11*, 142-147.

Griesbeck, O. (2004). Fluorescent proteins as sensors for cellular functions. Current Opinion in Neurobiology *14*, 636-641.

Grillo, F.W., Song, S., Teles-Grilo Ruivo, L.M., Huang, L., Gao, G., Knott, G.W., Maco, B., Ferretti, V., Thompson, D., Little, G.E.*, et al.* (2013). Increased axonal bouton dynamics in the aging mouse cortex. Proc Natl Acad Sci U S A *110*, E1514-1523.

Grinvald, A., and Steinberg, I.Z. (1974). On the analysis of fluorescence decay kinetics by the method of least-squares. Analytical biochemistry *59*, 583-598.

Gruol, D.L., Barker, J.L., Huang, L.Y.M., Macdonald, J.F., and Smith, T.G. (1980). Hydrogen-Ions Have Multiple Effects on the Excitability of Cultured Mammalian Neurons. Brain research *183*, 247-252.

Guerrero, G., Reiff, D.F., Agarwal, G., Ball, R.W., Borst, A., Goodman, C.S., and Isacoff, E.Y. (2005). Heterogeneity in synaptic transmission along a Drosophila larval motor axon. Nat Neurosci *8*, 1188-1196.

Hanifin, J.M., Chan, S.C., Cheng, J.B., Tofte, S.J., Henderson, W.R., Kirby, D.S., and Weiner, E.S. (1996). Type 4 phosphodiesterase inhibitors have clinical and in vitro anti-inflammatory effects in atopic dermatitis. Journal of Investigative Dermatology *107*, 51-56.

Harrison, R.G. (1910). The outgrowth of the nerve fiber as a mode of protoplasmic movement. The Journal of experimental zoology *142*, 5-73.

Harvey, C.D., Yasuda, R., Zhong, H.N., and Svoboda, K. (2008). The spread of Ras activity triggered by activation of a single dendritic spine. Science *321*, 136-140.

Hebb, D.O. (1949). The organization of behavior a neuropsychological theory ([S.l.]: John Wiley).

Hempel, C.M., Vincent, P., Adams, S.R., Tsien, R.Y., and Selverston, A.I. (1996). Spatio-temporal dynamics of cyclic AMP signals in an intact neural circuitm. Nature *384*, 166-169.

Herculano-Houzel, S., Mota, B., and Lent, R. (2006). Cellular scaling rules for rodent brains. Proc Natl Acad Sci U S A *103*, 12138-12143.

Hogue, M.J. (1947). Human fetal ependymal cells in tissue cultures. The Anatomical record *99*, 642.

Hoogland, T.M., and Saggau, P. (2004). Facilitation of L-type Ca2+ channels in dendritic spines by activation of beta2 adrenergic receptors. The Journal of neuroscience : the official journal of the Society for Neuroscience *24*, 8416-8427.

Horikawa, K., Yamada, Y., Matsuda, T., Kobayashi, K., Hashimoto, M., Matsu-ura, T., Miyawaki, A., Michikawa, T., Mikoshiba, K., and Nagai, T. (2010). Spontaneous network activity visualized by ultrasensitive Ca(2+) indicators, yellow Cameleon-Nano. Nat Methods *7*, 729-732.

Huang, Y.Y., Li, X.C., and Kandel, E.R. (1994). CAMP CONTRIBUTES TO MESSY FIBER LTP BY INITIATING BOTH A COVALENTLY MEDIATED EARLY PHASE AND MACROMOLECULAR SYNTHESIS-DEPENDENT LATE-PHASE. Cell *79*.

Hutsler, J.J., and Zhang, H. (2010). Increased dendritic spine densities on cortical projection neurons in autism spectrum disorders. Brain research *1309*, 83-94.

Inan, M., Lu, H.C., Albright, M.J., She, W.C., and Crair, M.C. (2006). Barrel map development relies on protein kinase A regulatory subunit II beta-mediated cAMP signaling. The Journal of neuroscience : the official journal of the Society for Neuroscience *26*, 4338-4349.

Isaac, J.T., Nicoll, R.A., and Malenka, R.C. (1995). Evidence for silent synapses: implications for the expression of LTP. Neuron *15*, 427-434.

Ishii, M., Kunimura, J.S., Jeng, H.T., Vessoni Penna, T.C., and Cholewa, O. (2007). Evaluation of the pH- and thermal stability of the recombinant green fluorescent protein (GFP) in the presence of sodium chloride. Appl Biochem Biotech *137*, 555-571.

Ivins, J.K., Parry, M.K., and Long, D.A. (2004). A novel cAMP-dependent pathway activates neuronal integrin function in retinal neurons. Journal of Neuroscience *24*, 1212-1216.

Jain, R.A. (2000). The manufacturing techniques of various drug loaded biodegradable poly(lactide-co-glycolide) (PLGA) devices. Biomaterials *21*, 2475-2490.

Jamain, S., Quach, H., Betancur, C., Rastam, M., Colineaux, C., Gillberg, I.C., Soderstrom, H., Giros, B., Leboyer, M., Gillberg, C.*, et al.* (2003). Mutations of the X-linked genes encoding neuroligins NLGN3 and NLGN4 are associated with autism. Nat Genet *34*, 27-29.

Jares-Erijman, E.A., and Jovin, T.M. (2003). FRET imaging. Nature biotechnology *21*, 1387-1395.

Jiang, M., and Chen, G. (2006). High Ca2+-phosphate transfection efficiency in low-density neuronal cultures. Nat Protoc *1*, 695-700.

Jurevicius, J., and Fischmeister, R. (1996). CAMP compartmentation is responsible for a local activation of cardiac Ca2+ channels by beta-adrenergic agonists. Proceedings of the National Academy of Sciences of the United States of America *93*, 295-299.

Kaech, S., and Banker, G. (2006). Culturing hippocampal neurons. Nature Protocols *1*, 2406-2415.

Kandel, E.R. (2001). The molecular biology of memory storage: a dialogue between genes and synapses. Science *294*, 1030-1038.

Kandel, E.R. (2012). The molecular biology of memory: cAMP, PKA, CRE, CREB-1, CREB-2, and CPEB. Mol Brain *5*.

Kandel, E.R.e., Schwartz, J.H.e., Jessell, T.M.e., Siegelbaum, S.e., and Hudspeth, A.J.e. (2001). Principles of neural science, Fifth edition. edn.

Kaneko, A., and Sankai, Y. (2014). Long-Term Culture of Rat Hippocampal Neurons at Low Density in Serum-Free Medium: Combination of the Sandwich Culture Technique with the Three-Dimensional Nanofibrous Hydrogel PuraMatrix. Plos One *9*.

Kanungo, T., Mount, D.M., Netanyahu, N.S., Piatko, C.D., Silverman, R., and Wu, A.Y. (2002). An efficient k-means clustering algorithm: Analysis and implementation. Ieee T Pattern Anal *24*, 881-892.

Kawasaki, H., Springett, G.M., Mochizuki, N., Toki, S., Nakaya, M., Matsuda, M., Housman, D.E., and Graybiel, A.M. (1998). A family of cAMP-binding proteins that directly activate Rap1. Science *282*, 2275-2279.

Kerr, R., Lev-Ram, V., Baird, G., Vincent, P., Tsien, R.Y., and Schafer, W.R. (2000). Optical imaging of calcium transients in neurons and pharyngeal muscle of C. elegans. Neuron *26*, 583-594.

Kirov, G., Pocklington, A.J., Holmans, P., Ivanov, D., Ikeda, M., Ruderfer, D., Moran, J., Chambert, K., Toncheva, D., Georgieva, L.*, et al.* (2012). De novo CNV analysis implicates specific abnormalities of postsynaptic signalling complexes in the pathogenesis of schizophrenia. Mol Psychiatr *17*, 142-153.

Klarenbeek, J., Goedhart, J., van Batenburg, A., Groenewald, D., and Jalink, K. (2015). Fourth-generation epac-based FRET sensors for cAMP feature exceptional brightness, photostability and dynamic range: characterization of dedicated sensors for FLIM, for ratiometry and with high affinity. Plos One *10*, e0122513.

Klarenbeek, J.B., Goedhart, J., Hink, M.A., Gadella, T.W.J., and Jalink, K. (2011). A mTurquoise-Based cAMP Sensor for Both FLIM and Ratiometric Read-Out Has Improved Dynamic Range. Plos One *6*.

Klein, T.M., Wolf, E.D., Wu, R., and Sanford, J.C. (1987). High-Velocity Microprojectiles for Delivering Nucleic-Acids into Living Cells. Nature *327*, 70-73.

Knott, G.W., Holtmaat, A., Wilbrecht, L., Welker, E., and Svoboda, K. (2006). Spine growth precedes synapse formation in the adult neocortex in vivo. Nature Neuroscience *9*, 1117-1124.

Kogan, J.H., Nestler, E.J., and Aghajanian, G.K. (1992). Elevated basal firing rates and enhanced responses to 8-Br-cAMP in locus coeruleus neurons in brain slices from opiate-dependent rats. European journal of pharmacology *211*, 47-53.

Konorski, J. (1948). Conditioned reflexes and neuron organisation ([S.l.]: Cambridge U.P.).

Kotaleski, J.H., and Blackwell, K.T. (2010). Modelling the molecular mechanisms of synaptic plasticity using systems biology approaches. Nat Rev Neurosci *11*, 239-251.

Kraemer, A., Rehmann, H.R., Cool, R.H., Theiss, C., de Rooij, J., Bos, J.L., and Wittinghofer, A. (2001). Dynamic interaction of cAMP with the Rap guanine-nucleotide exchange factor Epac1. Journal of Molecular Biology *306*, 1167-1177.

Krasowska, J., Olasek, M., Bzowska, A., Clark, P.L., and Wielgus-Kutrowska, B. (2010). The comparison of aggregation and folding of enhanced green fluorescent protein (EGFP) by spectroscopic studies. Spectrosc-Int J *24*, 343-348.

Krishtal, O.A., and Pidoplichko, V.I. (1981). A Receptor for Protons in Small Neurons of Trigeminal Ganglia - Possible Role in Nociception. Neuroscience letters *24*, 243-246.

Kumar, A., and Mallick, B.N. (2016). Long-term primary culture of neurons taken from chick embryo brain: A model to study neural cell biology, synaptogenesis and its dynamic properties. J Neurosci Methods *263*, 123-133.

Kumar, S., Alibhai, D., Margineanu, A., Laine, R., Kennedy, G., McGinty, J., Warren, S., Kelly, D., Alexandrov, Y., Munro, I.*, et al.* (2011). FLIM FRET technology for drug discovery: automated multiwell-plate high-content analysis, multiplexed readouts and application in situ. Chemphyschem : a European journal of chemical physics and physical chemistry *12*, 609-626.

Lee, D., and O'Dowd, D.K. (2000). cAMP-dependent plasticity at excitatory cholinergic synapses in Drosophila neurons: Alterations in the memory mutant dunce. Journal of Neuroscience *20*.

Lee, S.J.R., Escobedo-Lozoya, Y., Szatmari, E.M., and Yasuda, R. (2009). Activation of CaMKII in single dendritic spines during long-term potentiation. Nature *458*, 299-U258.

Leenders, A.G., and Sheng, Z.H. (2005). Modulation of neurotransmitter release by the second messenger-activated protein kinases: implications for presynaptic plasticity. Pharmacology & therapeutics *105*, 69-84.

Lessmann, V., and Heumann, R. (1997). Cyclic AMP endogenously enhances synaptic strength of developing glutamatergic synapses in serum-free microcultures of rat hippocampal neurons. Brain research *763*, 111-122.

Lesuisse, C., and Martin, L.J. (2002). Long-term culture of mouse cortical neurons as a model for neuronal development, aging, and death. J Neurobiol *51*, 9-23.

Li, L., Gervasi, N., and Girault, J.A. (2015). Dendritic geometry shapes neuronal cAMP signalling to the nucleus. Nat Commun *6*, 6319.

Liebenberg, N., Harvey, B.H., Brand, L., and Brink, C.B. (2010). Antidepressant-like properties of phosphodiesterase type 5 inhibitors and cholinergic dependency in a genetic rat model of depression. Behavioural pharmacology *21*, 540-547.

Linden, D.J. (1997). Long-term potentiation of glial synaptic currents in cerebellar culture. Neuron *18*, 983-994.

Linden, D.J. (1998). Synaptically evoked glutamate transport currents may be used to detect the expression of long-term potentiation in cerebellar culture. J Neurophysiol *79*, 3151-3156.

Lonart, G., Schoch, S., Kaeser, P.S., Larkin, C.J., Sudhof, T.C., and Linden, D.J. (2003). Phosphorylation of RIM1 alpha by PKA triggers presynaptic long-term potentiation at cerebellar parallel fiber synapses. Cell *115*, 49-60.

Lowel, S., and Singer, W. (1992). Selection of intrinsic horizontal connections in the visual cortex by correlated neuronal activity. Science *255*, 209-212.

Lu, W., Man, H., Ju, W., Trimble, W.S., MacDonald, J.F., and Wang, Y.T. (2001). Activation of synaptic NMDA receptors induces membrane insertion of new AMPA receptors and LTP in cultured hippocampal neurons. Neuron *29*, 243-254.

Luscher, C., Xia, H., Beattie, E.C., Carroll, R.C., von Zastrow, M., Malenka, R.C., and Nicoll, R.A. (1999). Role of AMPA receptor cycling in synaptic transmission and plasticity. Neuron *24*, 649-658.

Lynch, M.J., Baillie, G.S., Mohamed, A., Li, X., Maisonneuve, C., Klussmann, E., van Heeke, G., and Houslay, M.D. (2005). RNA silencing identifies PDE4D5 as the functionally relevant cAMP phosphodiesterase interacting with beta arrestin to control the protein kinase

A/AKAP79-mediated switching of the beta(2)-adrenergic receptor to activation of ERK in HEK293B2 cells. Journal of Biological Chemistry *280*, 33178-33189.

Ma, L., Zablow, L., Kandel, E.R., and Siegelbaum, S.A. (1999). Cyclic AMP induces functional presynaptic boutons in hippocampal CA3-CA1 neuronal cultures. Nat Neurosci *2*, 24-30.

Ma, N., Abel, T., and Hernandez, P.J. (2009). Exchange protein activated by cAMP enhances long-term memory formation independent of protein kinase A. Learning & memory *16*, 367-370.

Mank, M., Reiff, D.F., Heim, N., Friedrich, M.W., Borst, A., and Griesbeck, O. (2006). A FRET-based calcium biosensor with fast signal kinetics and high fluorescence change. Biophysical journal *90*, 1790-1796.

Mank, M., Santos, A.F., Direnberger, S., Mrsic-Flogel, T.D., Hofer, S.B., Stein, V., Hendel, T., Reiff, D.F., Levelt, C., Borst, A.*, et al.* (2008). A genetically encoded calcium indicator for chronic in vivo two-photon imaging. Nat Methods *5*, 805-811.

Martin, A.C.L., and Cooper, D.M.F. (2006). Layers of organization of cAMP microdomains in a simple cell. Biochemical Society transactions *34*, 480-483.

Miyasaka, N., Arimatsu, Y., and Takiguchihayashi, K. (1999). Foreign gene expression in an organotypic culture of cortical anlage after in vivo electroporation. Neuroreport *10*, 2319-2323.

Miyawaki, A. (2003). Visualization of the spatial and temporal dynamics of intracellular signaling. Dev Cell *4*, 295-305.

Montminy, M. (1997). Transcriptional regulation by cyclic AMP. Annual review of biochemistry *66*, 807-822.

Montminy, M.R., and Bilezikjian, L.M. (1987). Binding of a nuclear protein to the cyclic-AMP response element of the somatostatin gene. Nature *328*, 175-178.

Montminy, M.R., Sevarino, K.A., Wagner, J.A., Mandel, G., and Goodman, R.H. (1986). Identification of a cyclic-AMP-responsive element within the rat somatostatin gene. Proc Natl Acad Sci U S A *83*, 6682-6686.

Morris, R.G.M., Davis, S., and Butcher, S.P. (1990). Hippocampal Synaptic Plasticity and Nmda Receptors - a Role in Information-Storage. Philos T Roy Soc B *329*, 187-204.

Mulkey, R.M., and Malenka, R.C. (1992). Mechanisms underlying induction of homosynaptic long-term depression in area CA1 of the hippocampus. Neuron *9*, 967-975.

Munno, D.W., Prince, D.J., and Syed, N.I. (2003). Synapse number and synaptic efficacy are regulated by presynaptic cAMP and protein kinase A. The Journal of neuroscience : the official journal of the Society for Neuroscience *23*, 4146-4155.

Murakoshi, H., Wang, H., and Yasuda, R. (2011). Local, persistent activation of Rho GTPases during plasticity of single dendritic spines. Nature *472*, 100-U132.

Murphy, R.C., and Messer, A. (2001). Gene transfer methods for CNS organotypic cultures: A comparison of three nonviral methods. Molecular Therapy *3*, 113-121.

Nagai, T., Ibata, K., Park, E.S., Kubota, M., Mikoshiba, K., and Miyawaki, A. (2002). A variant of yellow fluorescent protein with fast and efficient maturation for cell-biological applications. Nature biotechnology *20*, 87-90.

Nakai, J., Ohkura, M., and Imoto, K. (2001). A high signal-to-noise Ca(2+) probe composed of a single green fluorescent protein. Nature biotechnology *19*, 137-141.

Neumann, E., and Rosenheck, K. (1972). Permeability changes induced by electric impulses in vesicular membranes. The Journal of membrane biology *10*, 279-290.

Nikolaev, V.O., Bunemann, M., Hein, L., Hannawacker, A., and Lohse, M.J. (2004). Novel single chain cAMP sensors for receptor-induced signal propagation. Journal of Biological Chemistry *279*.

Oddo, S., Caccamo, A., Shepherd, J.D., Murphy, M.P., Golde, T.E., Kayed, R., Metherate, R., Mattson, M.P., Akbari, Y., and LaFerla, F.M. (2003). Triple-transgenic model of Alzheimer's disease with plaques and tangles: Intracellular A beta and synaptic dysfunction. Neuron *39*, 409-421.

Ooashi, N., Futatsugi, A., Yoshihara, F., Mikoshiba, K., and Kamiguchi, H. (2005). Cell adhesion molecules regulate Ca2+-mediated steering of growth cones via cyclic AMP and ryanodine receptor type 3. The Journal of cell biology *170*, 1159-1167.

Ostroveanu, A., van der Zee, E.A., Eisel, U.L., Schmidt, M., and Nijholt, I.M. (2010). Exchange protein activated by cyclic AMP 2 (Epac2) plays a specific and time-limited role in memory retrieval. Hippocampus *20*, 1018-1026.

Ouyang, M., Zhang, L., Zhu, J.J., Schwede, F., and Thomas, S.A. (2008). Epac signaling is required for hippocampus-dependent memory retrieval. Proceedings of the National Academy of Sciences of the United States of America *105*, 11993-11997.

Padilla-Parra, S., and Tramier, M. (2012). FRET microscopy in the living cell: Different approaches, strengths and weaknesses. Bioessays *34*, 369-376.

Pathak, D., Shields, L.Y., Mendelsohn, B.A., Haddad, D., Lin, W., Gerencser, A.A., Kim, H., Brand, M.D., Edwards, R.H., and Nakamura, K. (2015). The role of mitochondrially derived ATP in synaptic vesicle recycling. The Journal of biological chemistry *290*, 22325-22336.

Pedarzani, P., and Storm, J.F. (1993). PKA mediates the effects of monoamine transmitters on the K+ current underlying the slow spike frequency adaptation in hippocampal neurons. Neuron *11*, 1023-1035.

Pennuto, M., Dunlap, D., Contestabile, A., Benfenati, F., and Valtorta, F. (2002). Fluorescence resonance energy transfer detection of synaptophysin I and vesicle-associated membrane protein 2 interactions during exocytosis from single live synapses. Mol Biol Cell *13*, 2706-2717.

Pierce, J.P., and Lewin, G.R. (1994). An Ultrastructural Size Principle. Neuroscience *58*, 441-446.

Pinto, D., Pagnamenta, A.T., Klei, L., Anney, R., Merico, D., Regan, R., Conroy, J., Magalhaes, T.R., Correia, C., Abrahams, B.S.*, et al.* (2010). Functional impact of global rare copy number variation in autism spectrum disorders. Nature *466*, 368-372.

Ponsioen, B., Zhao, J., Riedl, J., Zwartkruis, F., van der Krogt, G., Zaccolo, M., Moolenaar, W.H., Bos, J.L., and Jalink, K. (2004). Detecting cAMP-induced Epac activation by

fluorescence resonance energy transfer: Epac as a novel cAMP indicator. EMBO reports *5*, 1176-1180.

Poser, S., and Storm, D.R. (2001). Role of Ca2+-stimulated adenylyl cyclases in LTP and memory formation. International journal of developmental neuroscience : the official journal of the International Society for Developmental Neuroscience *19*, 387-394.

Qiao, J., Mei, F.C., Popov, V.L., Vergara, L.A., and Cheng, X. (2002). Cell cycle-dependent subcellular localization of exchange factor directly activated by cAMP. The Journal of biological chemistry *277*, 26581-26586.

Raman, I.M., Tong, G., and Jahr, C.E. (1996). Beta-adrenergic regulation of synaptic NMDA receptors by cAMP-dependent protein kinase. Neuron *16*, 415-421.

Rathenberg, J., Nevian, T., and Witzemann, V. (2003). High-efficiency transfection of individual neurons using modified electrophysiology techniques. J Neurosci Meth *126*, 91-98.

Ratsep, M., Linnanto, J., and Freiberg, A. (2009). Mirror symmetry and vibrational structure in optical spectra of chlorophyll a. J Chem Phys *130*, 194501.

Rehmann, H., Schwede, F., Doskeland, S.O., Wittinghofer, A., and Bos, J.L. (2003). Ligand-mediated activation of the cAMP-responsive guanine nucleotide exchange factor Epac. The Journal of biological chemistry *278*, 38548-38556.

Renau, T.E. (2004). The potential of phosphodiesterase 4 inhibitors for the treatment of depression: opportunities and challenges. Current opinion in investigational drugs *5*, 34-39.

Rich, T.C., Fagan, K.A., Tse, T.E., Schaack, J., Cooper, D.M.F., and Karpen, J.W. (2001a). A uniform extracellular stimulus triggers distinct cAMP signals in different compartments of a simple cell (vol 98, pg 13049, 2001). Proceedings of the National Academy of Sciences of the United States of America *98*, 14744-14744.

Rich, T.C., Tsf, T.E., Rohan, J.G., Schaack, J., and Karpen, J.W. (2001b). In vivo assessment of local phosphodiesterase activity using tailored cyclic nucleotide-gated channels as cAMP sensors. J Gen Physiol *118*, 63-77.

Richter, W., Menniti, F.S., Zhang, H.T., and Conti, M. (2013). PDE4 as a target for cognition enhancement. Expert Opin Ther Tar *17*, 1011-1027.

Rizzo, M.A., Springer, G.H., Granada, B., and Piston, D.W. (2004). An improved cyan fluorescent protein variant useful for FRET. Nature biotechnology *22*, 445-449.

Roscioni, S.S., Elzinga, C.R., and Schmidt, M. (2008). Epac: effectors and biological functions. Naunyn-Schmiedeberg's archives of pharmacology *377*, 345-357.

Rossato, J.I., Bevilaqua, L.R., Izquierdo, I., Medina, J.H., and Cammarota, M. (2009). Dopamine controls persistence of long-term memory storage. Science *325*, 1017-1020.

Sabatini, B.L., Oertner, T.G., and Svoboda, K. (2002). The life cycle of Ca(2+) ions in dendritic spines. Neuron *33*, 439-452.

Salin, P.A., Malenka, R.C., and Nicoll, R.A. (1996). Cyclic AMP mediates a presynaptic form of LTP at cerebellar parallel fiber synapses. Neuron *16*, 797-803.

Schacher, S., Castellucci, V.F., and Kandel, E.R. (1988). CAMP EVOKES LONG-TERM FACILITATION IN APLYSIA SENSORY NEURONS THAT REQUIRES NEW PROTEIN-SYNTHESIS. Science *240*.

Schikorski, T., and Stevens, C.F. (1997). Quantitative ultrastructural analysis of hippocampal excitatory synapses. The Journal of neuroscience : the official journal of the Society for Neuroscience *17*, 5858-5867.

Scott, A.J., and Knott, M. (1974). Cluster-Analysis Method for Grouping Means in Analysis of Variance. Biometrics *30*, 507-512.

Scott, J.M., Li, S., Harper, S.Q., Welikson, R., Bourque, D., DelloRusso, C., Hauschka, S.D., and Chamberlain, J.S. (2002). Viral vectors for gene transfer of micro-, mini-, or full-length dystrophin. Neuromuscular disorders : NMD *12 Suppl 1*, S23-29.

Seamon, K.B., and Daly, J.W. (1981). Forskolin: a unique diterpene activator of cyclic AMP-generating systems. Journal of cyclic nucleotide research *7*, 201-224.

Seino, S., and Shibasaki, T. (2005). PKA-dependent and PKA-independent pathways for cAMP-regulated exocytosis. Physiol Rev *85*, 1303-1342.

Selemon, L.D., and Goldman-Rakic, P.S. (1999). The reduced neuropil hypothesis: A circuit based model of schizophrenia. Biol Psychiat *45*, 17-25.

Selkoe, D.J. (2002). Alzheimer's disease is a synaptic failure. Science *298*, 789-791.

Shakiryanova, D., and Levitan, E.S. (2008). Prolonged presynaptic posttetanic cyclic GMP signaling in Drosophila motoneurons. Proc Natl Acad Sci U S A *105*, 13610-13613.

Sheng, M., and Kim, E. (2000). The Shank family of scaffold proteins. J Cell Sci *113 (Pt 11)*, 1851-1856.

Shimomura, O., Johnson, F.H., and Saiga, Y. (1962). Extraction, purification and properties of aequorin, a bioluminescent protein from the luminous hydromedusan, Aequorea. Journal of cellular and comparative physiology *59*, 223-239.

Sirevaag, A.M., and Greenough, W.T. (1987). Differential rearing effects on rat visual cortex synapses. III. Neuronal and glial nuclei, boutons, dendrites, and capillaries. Brain research *424*, 320-332.

Sollner, T., Whiteheart, S.W., Brunner, M., Erdjument-Bromage, H., Geromanos, S., Tempst, P., and Rothman, J.E. (1993). SNAP receptors implicated in vesicle targeting and fusion. Nature *362*, 318-324.

Song, S., Grillo, F.W., Xi, J., Ferretti, V., Gao, G., and De Paola, V. (2016). EPBscore: a Novel Method for Computer-Assisted Analysis of Axonal Structure and Dynamics. Neuroinformatics *14*, 121-127.

Steinberg, S.F., and Brunton, L.L. (2001). Compartmentation of G protein-coupled signaling pathways in cardiac myocytes. Annu Rev Pharmacol Toxicol *41*, 751-773.

Stettler, D.D., Yamahachi, H., Li, W., Denk, W., and Gilbert, C.D. (2006). Axons and synaptic boutons are highly dynamic in adult visual cortex. Neuron *49*, 877-887.

Szmacinski, H., and Lakowicz, J.R. (1993). Optical Measurements of Ph Using Fluorescence Lifetimes and Phase-Modulation Fluorometry. Anal Chem *65*, 1668-1674.

Takamori, S., Holt, M., Stenius, K., Lemke, E.A., Gronborg, M., Riedel, D., Urlaub, H., Schenck, S., Brugger, B., Ringler, P.*, et al.* (2006). Molecular anatomy of a trafficking organelle. Cell *127*, 831-846.

Takao, K., Okamoto, K., Nakagawa, T., Neve, R.L., Nagai, T., Miyawaki, A., Hashikawa, T., Kobayashi, S., and Hayashi, Y. (2005). Visualization of synaptic Ca2+ /calmodulin-dependent protein kinase II activity in living neurons. The Journal of neuroscience : the official journal of the Society for Neuroscience *25*, 3107-3112.

Terry, R.D., Masliah, E., Salmon, D.P., Butters, N., Deteresa, R., Hill, R., Hansen, L.A., and Katzman, R. (1991). Physical Basis of Cognitive Alterations in Alzheimers-Disease - Synapse Loss Is the Major Correlate of Cognitive Impairment. Ann Neurol *30*, 572-580.

Teruel, M.N., and Meyer, T. (1997). Electroporation-induced formation of individual calcium entry sites in the cell body and processes of adherent cells. Biophysical journal *73*, 1785-1796.

Teyler, T.J., Alger, B.E., Bergman, T., and Livingston, K. (1977). Comparison of Long-Term Potentiation in Invitro and Invivo Hippocampal Preparations. Behav Biol *19*, 24-34.

Tian, L., Hires, S.A., Mao, T., Huber, D., Chiappe, M.E., Chalasani, S.H., Petreanu, L., Akerboom, J., McKinney, S.A., Schreiter, E.R.*, et al.* (2009). Imaging neural activity in worms, flies and mice with improved GCaMP calcium indicators. Nat Methods *6*, 875-881.

Trudeau, L.E., Emery, D.G., and Haydon, P.G. (1996). Direct modulation of the secretory machinery underlies PKA-dependent synaptic facilitation in hippocampal neurons. Neuron *17*, 789-797.

Turner, K.M., Burgoyne, R.D., and Morgan, A. (1999). Protein phosphorylation and the regulation of synaptic membrane traffic. Trends Neurosci *22*, 459-464.

Tzounopoulos, T., Janz, R., Sudhof, T.C., Nicoll, R.A., and Malenka, R.C. (1998). A role for cAMP in long-term depression at hippocampal mossy fiber synapses. Neuron *21*, 837-845.

van der Krogt, G.N.M., Ogink, J., Ponsioen, B., and Jalink, K. (2008). A Comparison of Donor-Acceptor Pairs for Genetically Encoded FRET Sensors: Application to the Epac cAMP Sensor as an Example. Plos One *3*.

Vanderklish, P.W., Krushel, L.A., Holst, B.H., Gally, J.A., Crossin, K.L., and Edelman, G.M. (2000). Marking synaptic activity in dendritic spines with a calpain substrate exhibiting fluorescence resonance energy transfer. Proc Natl Acad Sci U S A *97*, 2253-2258.

Vlachos, A., Muller-Dahlhaus, F., Rosskopp, J., Lenz, M., Ziemann, U., and Deller, T. (2012). Repetitive magnetic stimulation induces functional and structural plasticity of excitatory postsynapses in mouse organotypic hippocampal slice cultures. The Journal of neuroscience : the official journal of the Society for Neuroscience *32*, 17514-17523.

Wang, Y., Guo, H.F., Pologruto, T.A., Hannan, F., Hakker, I., Svoboda, K., and Zhong, Y. (2004). Stereotyped odor-evoked activity in the mushroom body of Drosophila revealed by green fluorescent protein-based Ca2+ imaging. The Journal of neuroscience : the official journal of the Society for Neuroscience *24*, 6507-6514.

Weiss, B., and Hait, W.N. (1977). Selective Cyclic Nucleotide Phosphodiesterase Inhibitors as Potential Therapeutic Agents. Annual Review of Pharmacology and Toxicology *17*, 441-477.

Weisskopf, M.G., Castillo, P.E., Zalutsky, R.A., and Nicoll, R.A. (1994a). MEDIATION OF HIPPOCAMPAL MOSSY FIBER LONG-TERM POTENTIATION BY CYCLIC-AMP. Science *265*.

Weisskopf, M.G., Castillo, P.E., Zalutsky, R.A., and Nicoll, R.A. (1994b). Mediation of hippocampal mossy fiber long-term potentiation by cyclic AMP. Science *265*, 1878-1882.

Williams, J.T., Christie, M.J., and Manzoni, O. (2001). Cellular and synaptic adaptations mediating opioid dependence. Physiol Rev *81*, 299-343.

Wong, S.T., Athos, J., Figueroa, X.A., Pineda, V.V., Schaefer, M.L., Chavkin, C.C., Muglia, L.J., and Storm, D.R. (1999). Calcium-stimulated adenylyl cyclase activity is critical for hippocampus-dependent long-term memory and late phase LTP. Neuron *23*, 787-798.

Wong, W., and Scott, J.D. (2004). AKAP signalling complexes: Focal points in space and time. Nat Rev Mol Cell Bio *5*, 959-970.

Woo, N.H., Duffy, S.N., Abel, T., and Nguyen, P.V. (2003). Temporal spacing of synaptic stimulation critically modulates the dependence of LTP on cyclic AMP-dependent protein kinase. Hippocampus *13*, 293-300.

Woolfrey, K.M., Srivastava, D.P., Photowala, H., Yamashita, M., Barbolina, M.V., Cahill, M.E., Xie, Z., Jones, K.A., Quilliam, L.A., Prakriya, M.*, et al.* (2009). Epac2 induces synapse remodeling and depression and its disease-associated forms alter spines. Nature Neuroscience *12*.

Xia, Z., and Liu, Y. (2001). Reliable and global measurement of fluorescence resonance energy transfer using fluorescence microscopes. Biophysical journal *81*, 2395-2402.

Xu, T., Yu, X., Perlik, A.J., Tobin, W.F., Zweig, J.A., Tennant, K., Jones, T., and Zuo, Y. (2009). Rapid formation and selective stabilization of synapses for enduring motor memories. Nature *462*, 915-919.

Yagishita, S., Hayashi-Takagi, A., Ellis-Davies, G.C., Urakubo, H., Ishii, S., and Kasai, H. (2014). A critical time window for dopamine actions on the structural plasticity of dendritic spines. Science *345*, 1616-1620.

Yamahachi, H., Marik, S.A., McManus, J.N., Denk, W., and Gilbert, C.D. (2009). Rapid axonal sprouting and pruning accompany functional reorganization in primary visual cortex. Neuron *64*, 719-729.

Yamamoto, C., and Chujo, T. (1978). Long-term potentiation in thin hippocampal sections studied by intracellular and extracellular recordings. Experimental neurology *58*, 242-250.

Yasuda, R. (2006). Imaging spatiotemporal dynamics of neuronal signaling using fluorescence resonance energy transfer and fluorescence lifetime imaging microscopy. Current Opinion in Neurobiology *16*, 551-561.

Yin, Y.Q., Henzl, M.T., Lorber, B., Nakazawa, T., Thomas, T.T., Jiang, F., Langer, R., and Benowitz, L.I. (2006). Oncomodulin is a macrophage-derived signal for axon regeneration in retinal ganglion cells. Nature Neuroscience *9*, 843-852.

Yuste, R., and Bonhoeffer, T. (2001). Morphological changes in dendritic spines associated with long-term synaptic plasticity. Annu Rev Neurosci *24*, 1071-1089.

Zaccolo, M. (2006). Phosphodiesterases and compartmentalized cAMP signalling in the heart. Eur J Cell Biol *85*, 693-697.

Zaccolo, M., De Giorgi, F., Cho, C.Y., Feng, L.X., Knapp, T., Negulescu, P.A., Taylor, S.S., Tsien, R.Y., and Pozzan, T. (2000). A genetically encoded, fluorescent indicator for cyclic AMP in living cells. Nature Cell Biology *2*, 25-29.

Zaccolo, M., and Pozzan, T. (2002). Discrete microdomains with high concentration of cAMP in stimulated rat neonatal cardiac myocytes. Science *295*, 1711-1715.

Zhang, J., Campbell, R.E., Ting, A.Y., and Tsien, R.Y. (2002). Creating new fluorescent probes for cell biology. Nature reviews Molecular cell biology *3*, 906-918.

Zhong, Y., and Wu, C.F. (1991). ALTERED SYNAPTIC PLASTICITY IN DROSOPHILA MEMORY MUTANTS WITH A DEFECTIVE CYCLIC-AMP CASCADE. Science *251*.

Ziv, N.E., and Garner, C.C. (2001). Principles of glutamatergic synapse formation: seeing the forest for the trees. Curr Opin Neurobiol *11*, 536-543.

Zuo, Y., Yang, G., Kwon, E., and Gan, W.B. (2005). Long-term sensory deprivation prevents dendritic spine loss in primary somatosensory cortex. Nature *436*, 261-265.

13 APPENDICES

13.1 APPENDIX I: *IN VIVO* CALCIUM ACTIVITY RECORDING

As described in section 3.2, calcium concentration has been shown to play an intrinsic role in the induction of LTP and long term synaptic plasticity. Calcium concentration within neurons has been shown to fluctuate rapidly upon neural activity, tied to depolarisation of the cell during signal transmission (Harvey et al., 2008; Kerr et al., 2000; Sabatini et al., 2002).

In order to monitor calcium transients within neurons, fluorescent-based probes have been developed over the past two decades to allow for the measurement of intracellular concentration over a range of temporal and spatial resolutions, illuminating compartmentalisation and time dynamics (Tian et al., 2009; Wang et al., 2004). These have included FRET sensors (Horikawa et al., 2010; Mank et al., 2008), however until recently the temporal resolution was lacking in elucidating these rapid events.

In 2013 (Chen et al.), a family of ultra-sensitive calcium indicators being developed culminated in the advent of GCaMP6, a reporter capable of producing detectable fluorescent signal upon transient calcium influxes during individual action potentials. The GCaMP protein (Nakai et al., 2001), which has undergone substantial improvement since its creation in 2001, however the mechanism remains the same: a circularly permuted GFP bound to the calcium-binding region of a calmodulin (CaM) protein increases in fluorescence as calcium binds. This allows for live calcium imaging in cells, displaying ‘flashes’ of activity in the green spectrum.

As the Neuroplasticity and Disease group were investigating the implantation of human induced pluripotent stem cells (iPSCs) into the murine brain to investigate hallmarks of human neuronal components *in vivo*, and are utilising this GCaMP6 protein, *in vivo* 2-photon imaging was used to assess the suitability for a possible combination of cAMP FRET sensor and GCaMP calcium probe.

Mice were injected with neuronally-differentiated iPSCs transfected with the GCaMP6 plasmid and tdTomato into the somatosensory cortex. A cranial window then allowed for long-term, *in vivo* imaging with 2-photon microscopy. Using the tdTomato channel to identify cells under bright field, 5-10 minute recording windows were then set up at three frames per second on regions of interest.

Images were finally analysed with a custom MATLAB software routine to analyse fluorescent intensity over the time course. An example neuron is show in Figure 50, with the raw images above and the output from the software below. As seen, there is a clear and relatively regular oscillation in the intensity profile, likely correlating with depolarisation events in the integrated neurons.

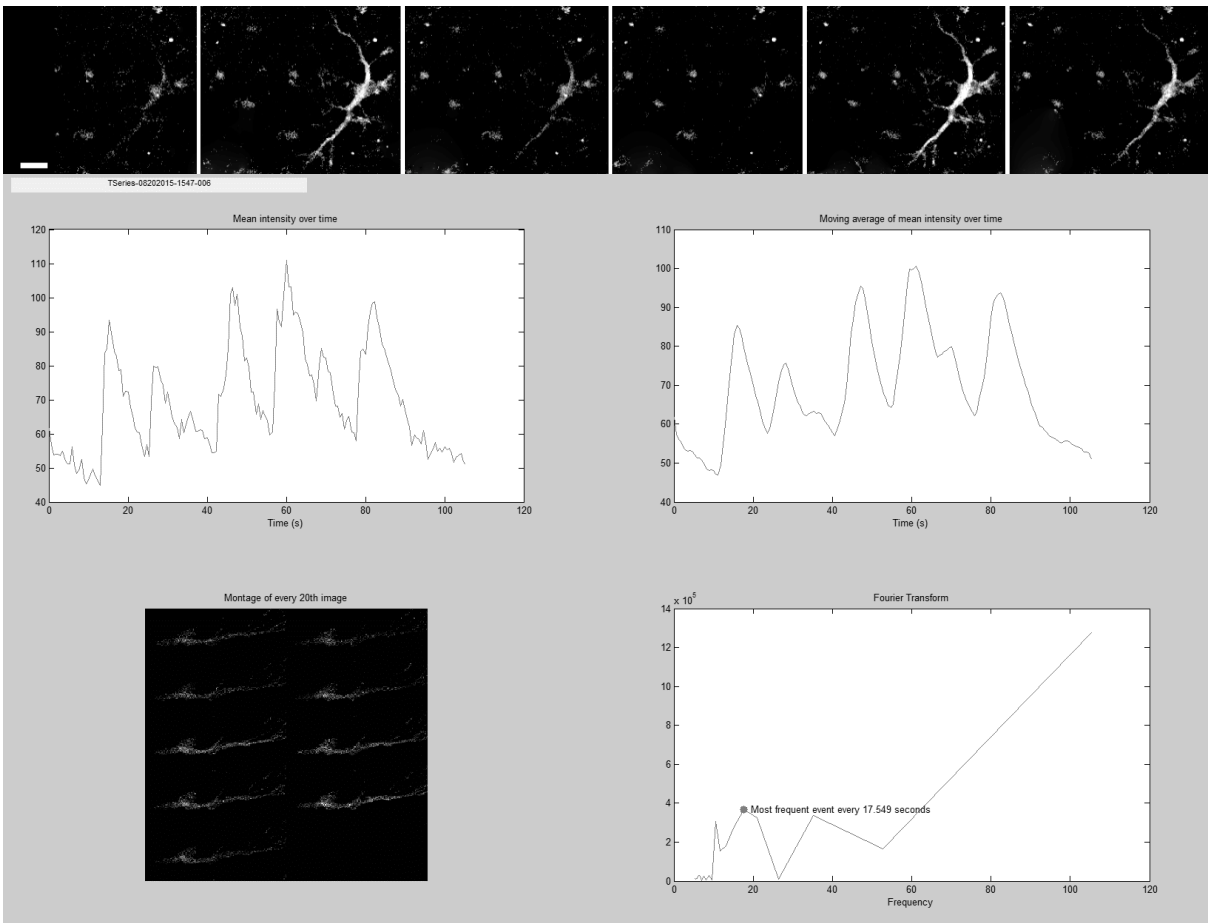


Figure 50 Calcium activity imaged and quantified from 2-Photon acquisition. Above shows a montage of a neuron activating over 30s, with one frame every 5s. The panels below show the output from the MATLAB software, mapping each peak over time. Finally, a Fourier transformation (bottom right) was used to attempt to identify regular patterns of activity.

While this system did establish a level of calcium activity of implanted human neurons *in vivo*, a technique that could provide massive gains in the study of neuropathologies; the spectra occupied by both the GCaMP and tdTomato proteins make it impossible to add FRET sensor recording in tandem.

However, this technique proves to be of particular interest in future experiments, providing a high temporal and spatial resolution for calcium transients, as well as human neuron studies.

13.2 Appendix II: Super Resolution Microscopy

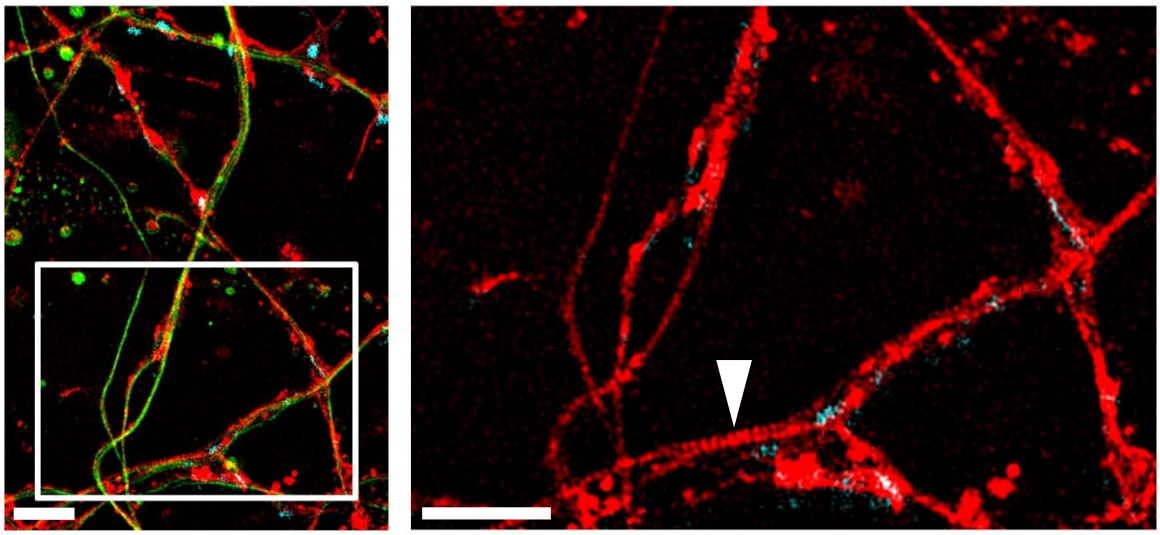


Figure 51 Super-resolution images of PNCs with a SIM system. Actin is stained red, with B3-Tubulin stained in green. The wide-field image is shown on the left, with the super-resolved image on the right. The white arrowhead shows the visible separation of actin rings, reportedly 80nm apart. Scale bar = 1µm.

Super resolution microscopy, in particular structured illumination microscopy (SIM) was explored during this project as a means of achieving higher resolution to study synaptic size changes. Despite achieving a high degree of spatial resolution, as seen in the figure above, of approximately 80nm, the system lacked in temporal resolution. It could also not appear to bring any greater information to synaptic structures, nor possessed the penetration ability for its use in tissue samples.

13.3 ADDITIONAL DRUG-INDUCED CHANGES OF CAMP ACTIVITY

In order to confirm the expected responses from cell preparations, forskolin and MDL-12,330A were added and ratiometric FRET responses were measured, as shown in Figure 52. The forskolin response was as expected, yielding a

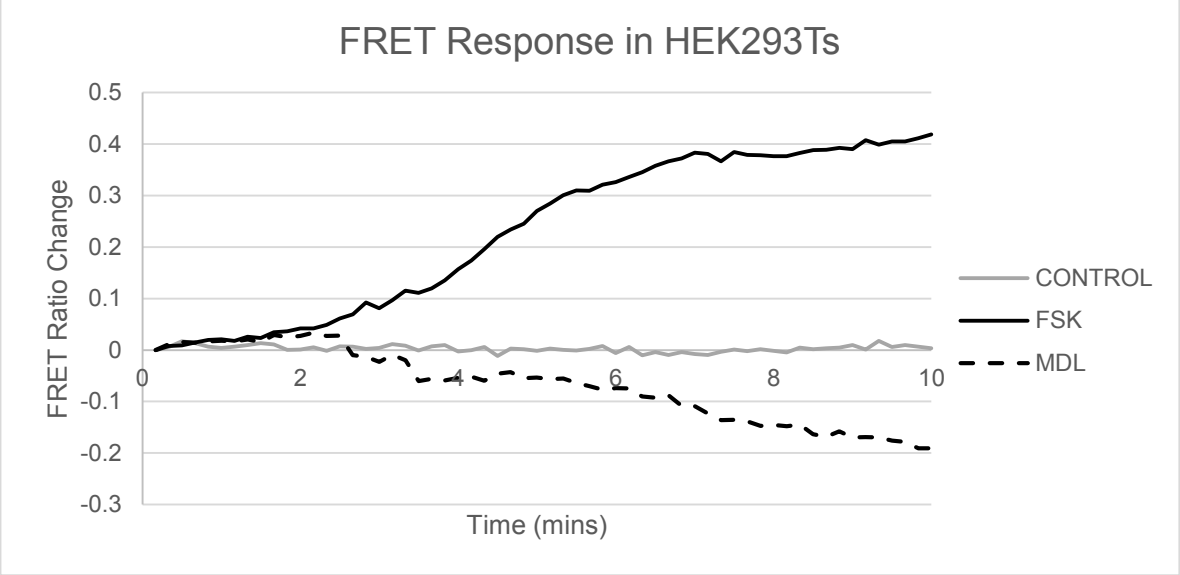


Figure 52 FRET responses for 100μM forskolin and 1mM MDL. HEK293T cells expressing the $^{mT}Epac^{VV}$ sensor were imaged with an inverted confocal microscope with a perfusion system for administering solutions. After 2 minutes, 100μM forskolin (FSK) or 1mM MDL was added. Donor and acceptor channel recordings allowed for a ratiometric FRET change to be recorded, representative of cAMP concentration.

13.4 APPENDIX IV: MATLAB CODE

13.4.1 FRET analysis of cells

```
n=406; %number of images
time_interval=5.307; %t-stack interval
drug1=11.7;
drug2=24.5; %time (in mins) when drug was added
thresh_percentage=20; %threshold to take values from, e.g. if 10, only the top 90% of pixels will be used
sg=4; % amount of smoothing in graphs (moving average value)
%Select first image in sequence
%-------------------------------------------------------------------------%
%STEP ONE: Get filename for importing a series of images & directory
%e.g. Pup1_LH2_Session_a_001_AVG.jpg to =imread("Pup1_LH3_b-',num2str(i,'%03i'),'_AVG.jpg");
%must be in the format of 000,001,002, etc.)
[name,pathstr]=uigetfile('*.jpg','Select first image in the series, e.g. exp3_t001_c001.jpg'); %user selects first file
cd(pathstr); %set path as the directory with the first image in it (optional)
filename1_idx=strfind(name,'_t0');%finds the number in the filename, position up to _t0, so e.g. exp3#
filename1=name(1:filename1_idx+1);%finds the first part of the filename, up to the number, e.g.
 str1=["",filename1,'001','_c001.jpg',""]; %creates filename for first image, '001'
 eval(['mask_image=imread(',str1,')',';',''])  %loads first images as variable 'mask_image'

 [mask,mask_coords]=imcrop(mask_image);
%mask_coords is now the coordinates for the corners of the ROI
 close all



%CHANNEL1 - CYAN
for i=1:n %change '1:n' to number of files in dir
   str1=["",filename1,num2str(i,'%03i'),'_c001.jpg',""];
%creates the full filename with 'i' being the number
   eval(['channel1=imread(',str1,')',';',''])  %loads image as channel1
    %NEW: Merge RGB:
    channel1=max(channel1, [], 3); %calculates max projection
    channel1=imcrop(channel1,mask_coords);  %applies ROI mask
    img_stack_c(:,:,i)=channel1; %records image by image to an image stack
end

%CHANNEL2 - YELLOW
for i=1:n %change '1:n' to number of files in dir
   str1=["",filename1,num2str(i,'%03i'),'_c002.jpg',""];
%creates the full filename with 'i' being the number
   eval(['channel1=imread(',str1,')',';',''])  %loads image as channel1
    %NEW: Merge RGB:
    channel1=max(channel1, [], 3); %calculates max projection
    channel1=imcrop(channel1,mask_coords);  %applies ROI mask
    img_stack_y(:,:,i)=channel1; %records image by image to an image stack
end
%STAGE 2: Means

sample_av=mean2(img_stack_c(:,:,1)); %takes average of first frame
thresh=(sample_av/100)*thresh_percentage; %generates threshold based on a given percentage of these pixels

for i=1:n
    a=img_stack_c(:,:,i);
    idx=find(a>thresh);
    a=a(idx); %removes all values below threshold
    averages_c(i)=mean2(a); %writes mean to averages_c list

 end

for i=1:n
    a=img_stack_y(:,:,i);
    idx=find(a>thresh);
    a=a(idx); %removes all values below threshold
    averages_y(i)=mean2(a); %writes mean to averages_c list
end

    %graph units
    frames=1:n;
    fpm=60/time_interval;
    mins=frames/fpm;

   mean_col_c=mean2(averages_c);
   mean_col_y=mean2(averages_y);

   if mean_col_c>mean_col_y
      averages_y=averages_y+(averages_c(30)-averages_y(30));

   else
      averages_c=averages_c+(averages_y(1)-averages_c(1));

   end
   title_string=['Mean Pixel Intensity of Each Frame in Mins - ',num2str(sg),' Point Moving Average'];
subplot(3,1,1)
plot(mins, smooth(averages_c, sg, 'moving'), 'b' );
hold on
plot(mins, smooth(averages_y, sg, 'moving'), 'r' );
title(title_string)
legend('CFP','YFP', 'Location','EastOutside')
%add drug line
line('XData', [drug1 drug1], 'YData', [min(averages_y) max(averages_y)], 'LineStyle', '-', ...
    'LineWidth', 1, 'Color','black');
hold off
%add drug line2

line('XData', [drug2 drug2], 'YData', [min(averages_y) max(averages_y)], 'LineStyle', '-', ...
    'LineWidth', 1, 'Color','black');
hold off
%STAGE THREE: RATIO
%fret_ratios=averages_y./(averages_y+averages_c);
%subplot(3,1,2)
%plot(mins,fret_ratios)
%title('FRET Ratios over Minutes, Scale 0-0.5')
     %moving average
  fret_ratios=averages_y./averages_c;
 % fret_ratios=averages_y./(averages_y+averages_c);
subplot(3,1,2)
plot(mins,smooth(fret_ratios, sg, 'moving'))
   title('FRET Ratios over Minutes, Moving Average')
%add drug line
line('XData', [drug1 drug1], 'YData', [min(fret_ratios) max(fret_ratios)], 'LineStyle', '-', ...
    'LineWidth', 1, 'Color','black');
%add drug line
line('XData', [drug2 drug2], 'YData', [min(fret_ratios) max(fret_ratios)], 'LineStyle', '-', ...
```

```
    'LineWidth', 1, 'Color','black');
%---------------------------------------
%Takes still image of cell selected
subplot(3,1,3)
title('Still image of selected cell')
imshow(img_stack_c(:,:,10)) %shows the ROI
```

13.4.2 Alignment of multiphoton tiling

```
%Program to align images using the Prarie Grid acquisition
system

%WARNING: All image from the 2P must be turned into one
8-bit multi-tiff
%using ImageJ first.
 [document,name]=uigetfile('*.xml', 'Select the metadata
xml file'); %gets the file
cd(name);
system('ren *.xml *.txt')
document=[document(1:end-3), 'txt'];
fid=fopen(document);
f=fscanf(fid,'%s');

%find x number of tiles
pos=strfind(f,"");
pos1=pos(23);
pos2=pos(24);
x_number=str2num(f(pos1+1:pos2-1));

%find y number of tiles
pos1=pos(25);
pos2=pos(26);
y_number=str2num(f(pos1+1:pos2-1));

%find overlap percentage
pos1=pos(27);
pos2=pos(28);
overlap=str2num(f(pos1+1:pos2-1));

%find z_stack size
z=size(strfind(f,'Cycle00001_'));
z_planes=z(2);
total_images=x_number*y_number;
 [name,pathstr]=uigetfile('*.tif','Select multi-tif with 8bit
images in it'); %user selects first file

cd(pathstr); %set path as the directory with the first image
in it (optional)

info = imfinfo(name);
num_images = numel(info);
for k = 1:num_images
    A = imread(name, k, 'Info', info);
   im_stack(:,:,k)=A;
end

    a=1; %z1
    b=z_planes; %zend
for i=1:total_images



    substack=im_stack(:,:,a:b);
    mip(:,:,i)=max(substack,[],3);

    a=a+z_planes;
    b=b+z_planes; %increase stack locations to next set of
z-planes
end

px_overlap=512-ceil(512/100*overlap);

grd_x_start=1;
grd_x_end=512;

grd_y_start=1;
grd_y_end=512;

o=1;
p=x_number;

for n=1:y_number

   for m=o:p
grid(grd_y_start:grd_y_end,grd_x_start:grd_x_end)=mip(:,:
,m);

grd_x_start=grd_x_start+px_overlap-1;
grd_x_end=grd_x_start+511;

   end
   grd_x_start=1;
grd_x_end=512;

  grd_y_start=grd_y_start+px_overlap-1;
grd_y_end=grd_y_start+511;

o=o+x_number;
p=p+x_number;
end

imshow(grid)
imwrite(grid,'final_stitch.tif','tif');
```

13.4.3 Alignment of multiphoton axonal tracking

```
clear all
%Program to align 2P images using their coordinates

%Images must first be made into max projections using
imageJ to output to a
%sequence of images using the numbering '000,001',etc.
This is because
%matlab cannot read the raw TIFFs from the 2P system

%Coordinates must be copied to a separate TXT file in
order of the image
%sequence, i.e. the image no. will not be read
%ALSO, coordinates must be in the format
(NUMBER,NUMBER) with no other
%brackets in the text file.

zoom_factor=150;
%ATTENTION: This is the number of microns in one
dimension of a single
%image. For z2, this is 150um, for z3 this is 100um.

%---------------------------------------------------------------------
-%
%STEP ONE: Get filename for importing a series of images
& directory
%e.g.          Pup1_LH2_Session_a_001_AVG.jpg          to
=imread("Pup1_LH3_b-',num2str(i,'%03i'),'_AVG.jpg");
%must be in the format of 000,001,002, etc.)
[name,pathstr]=uigetfile('*tif','Select first image in the
series, e.g. Pup1_LH2_a_001.jpg'); %user selects first file

cd(pathstr); %set path as the directory with the first image
in it (optional)
```

```
filename1_idx=strfind(name,'00');%finds the number in the filename
filename1=name(1:filename1_idx-1);%finds the first part of the filename, up to the number
filename2=name(filename1_idx+3:end);%finds the second part of the filename, after the number

%-------------------------------------------------------------------------
-%
%STEP TWO: Grab coordinates from within brackets of a text file
document=uigetfile('*.txt', 'Select the file with the coordinates in brackets, in order of image seq.'); %gets the file
fid=fopen(document);
f=fscanf(fid,'%s'); %turns all text into a single string
index_bracket= strfind(f,'('); %finds ( in the string
index_bracket2= strfind(f,')'); %finds ) in the string
[n,m]=size(index_bracket); % m is now how many values there are in the whole document
[n2,m2]=size(f); %m2 is now how many characters there are in the string, f

index_bracket=index_bracket'; %transpose to a list
index_bracket2=index_bracket2'; %transpose to a list

index_bracket=index_bracket+1; %move place to first number inside brackets
index_bracket2=index_bracket2-1;%move place to last number inside brackets

fx=[0 0]; %set variables
fy=[0 0]; %set variables

for i=1:m
value1=str2num(f(index_bracket(i):index_bracket2(i)));
%writes coordinates into var:Value1
co_x=value1(:,1);
co_y=value1(:,2);
fx=[fx,co_x]; %writes separate coordinates to fx or fy
fy=[fy,co_y];
end

fx=fx(3:m+2);%removes pre-allocation
fy=fy(3:m+2);%removes pre-allocation

coords_x=fx';%transpose to list and set as var: coords_x/y
coords_y=fy';

%-------------------------------------------------------------------------
-%

%STEP THREE: Convert coordinates to pixels
%i.e. coordinate width & height divided by 512
coord_convert=512/zoom_factor; %this is the number of pixels in one coordinate value, i.e. 512/one length of image in coords. N.b. 150 is only for zoom2x
coords_x=coords_x*coord_convert;
coords_y=coords_y*coord_convert;%converts values

%    b. Take minimum and maximum XY values to make complete matrix

x_min=min(coords_x);
y_min=min(coords_y);
%   c. Zero data to 0,0 and above

coords_x=coords_x-x_min;
coords_y=coords_y-y_min;
x_max=max(coords_x);
y_max=max(coords_y);
coords_x=ceil(coords_x); %rounds all numbers up to full integers
coords_y=ceil(coords_y);

%y coordinates need to be 'reversed' for axons going from top right to
%bottom left. This is MAX - the value

coords_y=max(coords_y)-coords_y; %IMPORTANT: This reverses the y-values, for some reason this seems to be needed to order the coordinates properly. Seems to be the same process for any axon...
%coords_x=max(coords_x)-coords_x;

%-------------------------------------------------------------------------
-%

%STEP FOUR: Make the total map, pre-allocated with zeros

total_map=zeros(ceil(y_max),ceil(x_max));          %makes zeroes matrix of X and Y maximum values, ceiling is because you can't have '0.5' of a pixel

total_map=uint8(total_map); %convert to uint8 format, this should be whatever form the original images are in

%-------------------------------------------------------------------------
-%

%STEP FIVE: Import images
x_number=size(coords_x);
x_number=x_number(:,1); %reads number of images

for i=1:x_number %change number to starting number of images, as selected in line 21, default =1
   str1=["",filename1,num2str(i,'%03i'),filename2,""];
%creates the full filename with 'i' being the number
   eval(['image=imread(',str1,')',';',''])


       %----------INSERTION OF NAME-STAMPING CODE----------%
   %Makes white image the same size as the oringinal
hf = figure('color','white','units','normalized','position',[.1 .1 .8 .8]);
image(ones(size(image)));
set(gca,'units','pixels','position',[5 5 size(image,2)-1 size(image,1)-1],'visible','off')


% Text at arbitrary position
text('units','pixels','position',[12
200],'rotation',90,'fontsize',15,'string',num2str(i,'%03i'))

% Capture the text image
% Note that the size will have changed by about 1 pixel
tim = getframe(gca);
close(hf)

% Extract the cdata
tim2 = tim.cdata;

% Make a mask with the negative of the text
tmask = tim2==0;

% Place white text
% Replace mask pixels with UINT8 max
tmask=tmask(:,:,1);
tim2=tmask(:,:,1);
image(tmask) = uint8(255);
```

```
        %-------------------------------------------------%


   eval(['img_',num2str(i,'%03i'),'=image;']); %loads images named '00#.jpg', where # is 1:the number of images. Saves these as 'img_00#' sequentially
end

%-------------------------------------------------------------------------
-%

%STEP SIX: Copies images to the coordinates on the total map

j=1;
for i=1:x_number
  eval(['place_img=img_',num2str(i,'%03i'),';'])

total_map(((coords_y(j))+1):((coords_y(j))+512),((coords_x(j))+1):((coords_x(j))+512))=place_img;
   j=j+1;
end

%-------------------------------------------------------------------------
-%
%Show final image and write to file
imshow(total_map)

if zoom_factor==150
    savezoom='complete_z2.tif';
elseif zoom_factor==100
    savezoom='complete_z2.tif';
else
     savezoom=['complete_', num2str(zoom_factor), 'z2.tif'];
     end
imwrite(total_map,savezoom,'TIF')
```

13.4.4 Time-Resolved Analysis for GcamP

```
%Program to analyse TIF files from t-series from GCAMP6 imaging
%Aims:
   %import files, to time stack, mask pixels based on activity/excl.
   %over-sat
   %plot intensity over time
   %FFT pattern recognition
   %quantitative - activity value for neuron
   %potential to measure red channel
   %export to video
clear all
close all

%set frames per second
%fps=input('what FPS was used?   ');
fps=3.4;
fps=fps/2;
disp('Select Images...')

%stage1 - import of TIFs

[name,pathstr]=uigetfile('*tif','Select the first TIF in the folder'); %user selects first file

cd(pathstr); %set path as the directory with the first img in it (optional)
filelist=dir('*.tif'); %lists TIF files in dir

filename1_idx=strfind(name,'Cycle');%finds the text Cycle in filename
filename1=name(1:filename1_idx+4); %loads first part up to the cycle number
filename2=name(filename1_idx+10:end); %loads second part of file name after cycle number

%-------------------------------------------------------------------------
-%
%-------------------------------------------------------------------------
-%

h = waitbar(0,'Loading Images...');
%load imgs - creates a stack
for i=1:length(filelist)
   str1=["",filename1,num2str(i,'%05i'),filename2,""];
%creates the full filename with 'i' being the number
   eval(['img(:,:,',num2str(i),')=imread(',str1,')',';',''])

   %load notes
perc = 100/length(filelist)*i;
waitbar(perc/100,h,sprintf('%d%% complete...',ceil(perc)))

end

close(h)



%threshold pixels to remove background (based on average intensity px)
stack_size=size(img);
disp('Averaging...')
%takes the average of each pixel
for j=1:stack_size(2) %y-axis
   for i=1:stack_size(1) %x-axis of each img
      img2=mean2(img(i,j,:));
      mean_img(i,j)=img2(1,:);
      end

end
disp('Thresholding...')
%replaces all pixels with a mean over with 0
img_thresholded=img;
for j=1:stack_size(2)
   for i=1:stack_size(1)
      if mean_img(i,j)<25
         img_thresholded(i,j,:)=0;
      else


      end
   end
end
disp('Select Rough Crop')
%display average image for crop and video to check activity
img_forplay = uint8(255*mat2gray(img));
implay(img_forplay,50)

figure('name','Select box around axon of interest (background will be removed)');
[mask,mask_coords]=imcrop(mean_img,[]);
%mask_coords is now the coordinates for the corners of the ROI
 close all

 disp('Masking Images...')
```

```
%crop stack to mask + average of each img
for i=1:length(filelist)

img_cropped(:,:,i)=imcrop(img_thresholded(:,:,i),mask_coo
rds);
 z=img_cropped(:,:,i); %take single image for...
 z(z==0)=[]; %remove threhsolded 0s from single image for
mean
 means(i)=mean2(z);
 z=double(z);
 variances(i)=var(z);
 %means(i)=mean2(img_thresholded(:,:,i));
end



disp('Displaying Analysis.')

x=1000/fps; %each frame in s

figresults=figure('name',name(1:end-30));

xaxis=1:x:(x*length(filelist));
xaxis=xaxis/1000;
subplot(2,2,1)
set(gcf, 'Position', get(0,'Screensize')); % Maximize figure.
plot(xaxis,means)
title('Mean intensity over time')
xlabel('Time (s)')
subplot (2,2,2)
plot(xaxis,smooth(means, 8, 'moving'), 'r' )
title('Moving average of mean intensity over time')
xlabel('Time (s)')

%textbox to display title
mTextBox = uicontrol('style','text');
figPosition = get(figresults,'Position');
y=figPosition(4)-30;
set(mTextBox,'String',name(1:end-30),'Position',[200 y 400
20])
%mTextBoxPosition = get(mTextBox,'Position');
%set(mTextBox,'Units','characters')



%img_cropped_8=uint8(img_cropped);
img_cropped8 = uint8(255*mat2gray(img_cropped));
implay(img_cropped8)

%show variances
%subplot(2,2,3)
%plot(xaxis,variances)
%title('Variance over time')
%xlabel('Time (s)')

%show mini montage
j=1;
cropsize=size(img_cropped);
imgresh=reshape(img_cropped,cropsize(1),cropsize(2),  1,
cropsize(3));
for i = 1:20:length(filelist)
    imgmont(:,:,:,j)=imgresh(:,:,:,i);
    j=j+1;
end
imgmont = uint8(255*mat2gray(imgmont));
subplot(2,2,3)
montage(imgmont)
title('Montage of every 20th image')

%FFT analysis

x=x/1000;
Y = fft(means);
Y(1) = [];

n = length(Y);
power = abs(Y(1:floor(n/2))).^2;
nyquist = 1/2;
freq = (1:n/2)/(n/2)*nyquist;
period=x./freq;
subplot(2,2,4)
plot(period(1:20),power(1:20))
xlabel('Frequency')
title('Fourier Transform')
hold on;
index = find(power == max(power));
if period(index) > (length(filelist)/fps)-5
    sorted=sort(power);
    find_index=sorted([end-1]);
    index = find(power==find_index);
end

maxfreq=period(index);
mainPeriodStr = num2str(period(index));
plot(period(index),power(index),'r.', 'MarkerSize',25);
text(period(index)+2,power(index),['Most  frequent  event
every ',mainPeriodStr,' seconds']);
hold off;

%write analysis
cd ..
if exist('Analysis') ~=7
mkdir ('Analysis')
else
end

cd Analysis

filenamexls=[filename1,'.xls'];
smoothmeans=smooth(means, 8, 'moving');
xlsdataheaders=['Time', 'Average', 'Smooth Average', 'FFT
Peak','FPS'];
for i=1:length(means)

xlsdata_numbers(:,i)=[xaxis(i),means(i),smoothmeans(i),m
axfreq,fps];

end

xlsdata_numbers= num2cell(xlsdata_numbers');
xls_export=[xlsdataheaders;xlsdata_numbers];

xlswrite(filenamexls,xls_export)
```